

10-A137 447

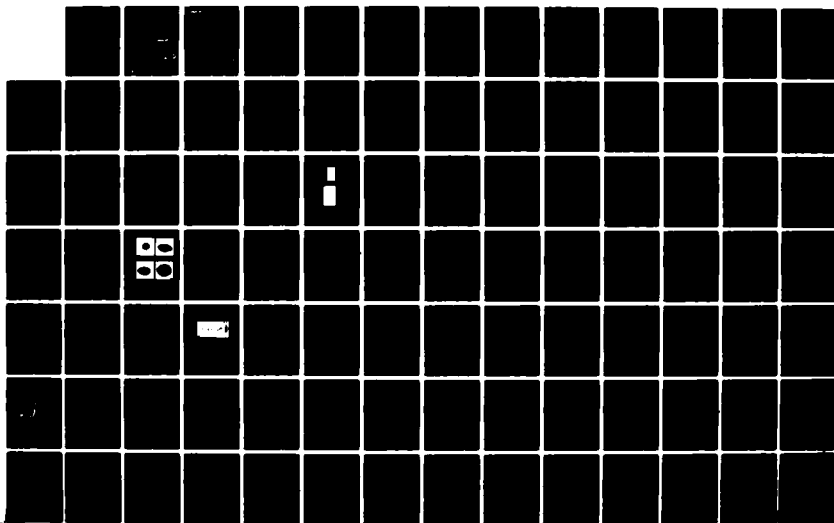
THE MODIFIED BETAIRUN ACCELERATOR EXPERIMENT(U) JAYCOR
ALEXANDRIA VA F M MAKD 06 JAN 84
JAYCOR-J206-84-001/6207 N00014-81-C-2095

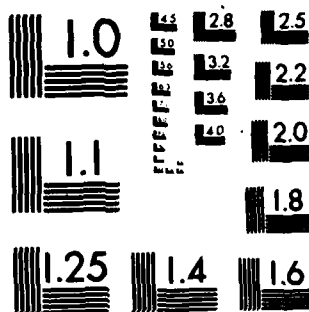
1/3

UNCLASSIFIED

F/G 20/7

NL





MICROCOPY RESOLUTION TEST CHART
NATIONAL BUREAU OF STANDARDS-1963 A

AD A 137447

THE MODIFIED BETATRON
ACCELERATOR EXPERIMENT

J206-84-001/6207

JAYCOR

DTIC
ELECTE
FEB 2 1984

FILE COPY

84 01 - 13 134

This document has been approved
for public release and sale in
distribution is unlimited.

JAYCOR

(12)

THE MODIFIED BETATRON
ACCELERATOR EXPERIMENT

J206-84-001/6207

Final Report

by

Frederick M. Mako

January 6, 1984

Prepared for:

Naval Research Laboratory
Washington, DC 20375

Under:

Contract Number N00014-81-C-2095

STIC
ELECTE
FEB 2 1984
A

This document has been approved
for public release and sale; its
distribution is unlimited.

UNCLASSIFIED

SECURITY CLASSIFICATION OF THIS PAGE (When Data Entered)

REPORT DOCUMENTATION PAGE		READ INSTRUCTIONS BEFORE COMPLETING FORM
1. REPORT NUMBER J206-84-001/6207	2. GOVT ACCESSION NO. AD-A137 447	3. RECIPIENT'S CATALOG NUMBER
4. TITLE (and Subtitle) THE MODIFIED BETATRON ACCELERATOR EXPERIMENT		5. TYPE OF REPORT & PERIOD COVERED Final Report: 01/12/81 thru 12/10/82
		6. PERFORMING ORG. REPORT NUMBER J206-84-001/6207
7. AUTHOR(s) Frederick M. Mako		8. CONTRACT OR GRANT NUMBER(s) N00014-81-C-2095
9. PERFORMING ORGANIZATION NAME AND ADDRESS JAYCOR 205 South Whiting Street Alexandria, VA 22304		10. PROGRAM ELEMENT, PROJECT, TASK AREA & WORK UNIT NUMBERS A003
11. CONTROLLING OFFICE NAME AND ADDRESS Naval Research Laboratory 4555 Overlook Avenue, SW Washington, DC 20375		12. REPORT DATE January 6, 1984
		13. NUMBER OF PAGES 203 pages
14. MONITORING AGENCY NAME & ADDRESS (if different from Controlling Office)		15. SECURITY CLASS. (of this report) UNCLASSIFIED
		15a. DECLASSIFICATION/DOWNGRADING SCHEDULE
16. DISTRIBUTION STATEMENT (of this Report) 1 copy - Code 4704 1 copy - Code 1232.MT 6 copies - Code 2627 12 copies - DTIC		
17. DISTRIBUTION STATEMENT (of the abstract entered in Block 20, if different from Report)		
18. SUPPLEMENTARY NOTES		
19. KEY WORDS (Continue on reverse side if necessary and identify by block number) Free electron lasers, induction linear accelerator, spectrometer, high power microwaves, gas breakdown, magnetic wiggler, numerical simulation, foilless diode, intense relativistic electron beams, intense ion beams, collective ion acceleration.		
20. ABSTRACT (Continue on reverse side if necessary and identify by block number)		

DD FORM 1473
1 JAN 73EDITION OF 1 NOV 65 IS OBSOLETE
S/N 0102-LP-014-6601

UNCLASSIFIED

SECURITY CLASSIFICATION OF THIS PAGE (When Data Entered)

TABLE OF CONTENTS

Introduction	1
A Free Electron Laser Driven by a Long Pulse Induction Linac;	2
Special Focus Program Advanced Accelerator Modified Betatron Design Review Coil Design;74
External Injection into a High Current Modified Betatron Accelerator;96
Electron Drift in a Linear Magnetic Wiggler with an Axial Guide Field;	110
A Broadband High Power Millimeter to Centimeter Spectrometer;	116
Electron Drift in a Linear Magnetic Wiggler with an Axial Guide Field;	139
Numerical Simulation of High Energy Light Ion Beam Flow Through a Foillless Diode; and	163
High Current, High Voltage Accelerators as Free-Electron Lasers Drivers	186

P. 69-73 Not missing
misnumbered

Acquisition Form	
100-1	<input checked="" type="checkbox"/>
TAB	<input type="checkbox"/>
ounced	<input type="checkbox"/>
ification	<input type="checkbox"/>
<i>John M. [Signature]</i>	
Distribution/	
Availability Codes	
and/or	
First	
A-1	



INTRODUCTION

The Naval Research Laboratory (NRL) is conducting a Special Focus Program in Advanced Accelerators, i.e., Modified Betatron Design. This program has been stimulated by the rapid advance in Free Electron Laser (FEL) research over the past several years. Great progress has been made in both the theoretical understanding of the mechanism and the experimental demonstration of the validity of many features predicted by theory. The FEL has attracted this interest because of its promise as a tunable, powerful, efficient source of radiation over a very large frequency range. The strong dependence of output frequency on electron energy ($\omega = \gamma^2$) makes scaling attractive. Furthermore, the availability of very high power electron beams ($>> \text{GW}$) makes possible the generation of high power radiation in regions of the spectrum when other practical high power sources do not exist.

JAYCOR has supported this program through investigations in the design and evaluation of several subsystems including the coil design, the application of the long pulse induction linac, and most important, the injection scheme for the accelerator. The results of these investigations are presented in the following publications produced during this effort.

The author wants to acknowledge the support of the NRL staff and co-contractors. Special appreciation is given to Dr. J. A. Pasour, Dr. J. Golden and Dr. C. W. Roberson of the NRL staff for their guidance and encouragement.

A Free Electron Laser Driven by a Long Pulse Induction Linac

C. W. Roberson, J. A. Pasour, F. Mako, R. Lucey and P. Sprangle

NRL Memorandum Report 5013

March 7, 1983

SECURITY CLASSIFICATION OF THIS PAGE (When Data Entered)

REPORT DOCUMENTATION PAGE		READ INSTRUCTIONS BEFORE COMPLETING FORM
1. REPORT NUMBER NRL Memorandum Report 5013	2. GOVT ACCESSION NO.	3. RECIPIENT'S CATALOG NUMBER
4. TITLE (and Subtitle) A FREE ELECTRON LASER DRIVEN BY A LONG PULSE INDUCTION LINAC		5. TYPE OF REPORT & PERIOD COVERED Interim report on a continuing NRL problem.
		6. PERFORMING ORG. REPORT NUMBER
7. AUTHOR(s) C. W. Roberson,* J. A. Pasour, F. Mako,** R. Lucey,† and P. Sprangle		8. CONTRACT OR GRANT NUMBER(s)
9. PERFORMING ORGANIZATION NAME AND ADDRESS Naval Research Laboratory Washington, DC 20375		10. PROGRAM ELEMENT PROJECT, TASK AREA & WORK UNIT NUMBERS 61153N; RR0110941; 47-1484-0-3
11. CONTROLLING OFFICE NAME AND ADDRESS Office of Naval Research Arlington, VA 22217		12. REPORT DATE March 7, 1983
		13. NUMBER OF PAGES 71
14. MONITORING AGENCY NAME & ADDRESS (if different from Controlling Office)		15. SECURITY CLASS. (of this report) UNCLASSIFIED
		15a. DECLASSIFICATION/DOWNGRADING SCHEDULE
16. DISTRIBUTION STATEMENT (of this Report) Approved for public release; distribution unlimited.		
17. DISTRIBUTION STATEMENT (of the abstract entered in Block 20, if different from Report)		
18. SUPPLEMENTARY NOTES *Present address: Office of Naval Research, Arlington, VA **Present address: JAYCOR, Alexandria, VA †Present address: Pulse Sciences Inc., San Leandro, CA (Continues)		
19. KEY WORDS (Continue on reverse side if necessary and identify by block number) Free electron lasers Induction linear accelerator		
20. ABSTRACT (Continue on reverse side if necessary and identify by block number) An overview of Free Electron Laser (FEL) research is presented, and a high-current, long pulse FEL experiment is described. The overview consists of a description of the FEL mechanism and operating regimes and a historical survey of experimental research. Preliminary results are presented from an FEL experiment using both linear and diffusive magnetic wigglers with a long pulse induction linac (≤ 800 kV, ≤ 800 A, $2 \mu\text{sec}$). Mode identification of the ~ 100 kW output radiation pulse indicates that both FEL and cyclotron emission is present.		

DD FORM 1473

EDITION OF 1 NOV 65 IS OBSOLETE
S/N 0102-010-6601

SECURITY CLASSIFICATION OF THIS PAGE (When Data Entered)

18. Supplementary Notes (Continued)

To be published in *Infrared and Millimeter Waves, Vol. 10*, ed. by K. J. Button,
Academic Press, N.Y.

CONTENTS

I. INTRODUCTION	1
II. FEL MECHANISM	2
III. FEL EXPERIMENTAL RESEARCH	5
IV. FEL OPERATING REGIMES	12
V. ACCELERATOR DEVELOPMENT	19
VI. THE FEL APPARATUS	28
VII. RADIATION MEASUREMENTS	45
VIII. CONCLUSIONS AND FUTURE DIRECTIONS	61
ACKNOWLEDGEMENTS	62
REFERENCES	63

A FREE ELECTRON LASER DRIVEN BY A LONG PULSE INDUCTION LINAC

I. Introduction

In the last five years, free electron laser (FEL) research has expanded rapidly. Great progress has been made both in the theoretical understanding of the mechanism and in the experimental demonstration of the validity of many features predicted by theory. The FEL has attracted this interest because of its promise as a tunable, powerful, and efficient source of radiation over a very large frequency range. The strong dependence of output frequency on electron energy ($\omega \propto \gamma^2$) makes scaling attractive. Furthermore, the availability of very high power electron beams ($>>1$ GW) makes possible the generation of high power radiation in regions of the spectrum where other practical high power sources do not exist.

In this paper we will present an overview of FEL research and then describe in some detail an ongoing experiment designed to produce mm-wave output from a long pulse induction linac ($\tau = 2$ μ sec). In Section II we will describe the FEL mechanism, and a brief history of FEL experimental research will be presented in Section III. Section IV will describe the various FEL operating regimes and discuss the beam requirements for operation in the Raman regime. Accelerator development and diode characteristics will be discussed in Section V and the long pulse induction linac described. Our FEL experiment will be described in Section VI along with a comparison of various wigglers. The experimental results will be presented in Section VII and future sections for the experiment and conclusions in Section VIII.

Manuscript approved December 23, 1982.

II. FEL Mechanism

To understand the FEL, let us consider a very low current electron beam so that space charge forces are not important. We assume the initial velocity of the electron beam is in the axial direction and we have a simple linear wiggler in the y direction.

Let

$$\underline{v}_b = v_b \hat{z} \quad (1)$$

and

$$\underline{B}_w = B_w \sin(k_w z) \hat{y} . \quad (2)$$

Then

$$\underline{v}_w = v_w \cos(k_w z) \hat{x} . \quad (3)$$

Here, v_b is the beam velocity, B_w the wiggler magnetic field, and v_w is the wiggle velocity that results from the Lorentz force acting on the particle as it passes through the wiggler field. We now assume the presence of a linearly polarized radiation field

$$\underline{E} + \underline{B} = E \cos(kz - \omega t) \hat{x} + B \sin(kz - \omega t) \hat{y} \quad (4)$$

This radiation field will exist as part of the noise spectrum in the case of the oscillator, or will be supplied externally in the case of an amplifier.

As a result of the wiggler and the radiation field, a pondermotive force in the z direction develops

$$\underline{F} = \frac{q}{c} (\underline{v}_w \times \underline{B} + \underline{v} \times \underline{B}_w) \hat{z} \approx \sin[(k \pm k_w) z - \omega t] \hat{z} \quad (5)$$

This force arises from the interaction between \underline{v}_w and the magnetic component of the radiation field and from the perturbed velocity \underline{v} (which results from $\underline{v}_b \times \underline{B}$) interacting with the wiggler field.

This pondermotive force drives a current, δJ_z . From the continuity equation $q \partial \delta n / \partial t = \nabla \cdot \delta \underline{J}$, we obtain a density modulation of the form

$$\delta n \approx \cos [(k \pm k_w) z - \omega t]. \quad (6)$$

This density modulation of the electron beam, driven by the pondermotive force, results in a current which can cause radiation in phase with the radiation field:

$$\delta \underline{J} = q \delta n \underline{v}_w \approx \cos (kz - \omega t) \hat{x}. \quad (7)$$

Therefore the pondermotive force causes the beam to bunch and the electrons to radiate coherently and in phase with the existing radiation. Thus the original radiation grows, which increases δn , increasing $\delta \underline{J}$ and so on until saturation occurs.

If $\delta n((k + k_w), \omega)$ is at a frequency and wave number that is also a beam mode, then we have a collective free electron laser. Then to determine the wavelength scaling, we assume the phase velocity of the pondermotive wave is near the beam velocity

$$v_{ph} = \frac{\omega}{k+k_w} = v_b. \quad (8)$$

Then using $\omega = ck$, we obtain

$$\lambda = \frac{1-\beta}{\beta} \lambda_w = \frac{\lambda_w}{2\gamma^2}. \quad (9)$$

This is the wavelength scaling law that is such an important feature of the FEL. If the beam current is high, the pondermotive force will drive a collective space charge wave. This enhances the interaction and increases the intrinsic efficiency. However the higher current introduces an additional complication, that of the beam rapidly expanding due to its own space charge. The simplest configuration to confine the beam is an axial magnetic field. This introduces the cyclotron modes on the beam, which can result in competing interactions.

III. FEL Experimental Research

As is typical in a rapidly developing, complex field such as free electron lasers, experiments have lagged behind theory to a large degree. In the last 2-3 years, however, scores of experiments have been proposed and undertaken to explore the many aspects of FEL operation predicted by theory. Although only preliminary results have been reported from most of these experiments, indications are that the FEL mechanism is a viable, tunable source of radiation from millimeter waves to the infrared. Experiments now underway are attempting to extend the range of operation into the visible and even beyond.

Free electron laser experiments have evolved along two distinct paths depending on the type of electron accelerator used. High current, relatively low particle energy electron beams typically from Marx type generators have been used for FEL experiments in the collective regime. More conventional accelerators such as RF linacs, which produce much higher energy electrons but at much lower current levels, have proved useful for FEL research in the Compton or single particle regime. Madey and coworkers¹ at Stanford have pioneered the Compton regime research using a superconducting linac together with a helical magnetic wiggler field (Elias et al., 1976; Deacon et al., 1977). They initially performed amplifier experiments at $\lambda = 10.6 \mu\text{m}$ and later demonstrated laser oscillator operation at $\lambda = 3.4 \mu\text{m}$ using a 43 MeV beam having a peak micropulse current of 2.6 A. The efficiency (laser energy/beam energy) of the oscillator was less than 10^{-4} , but it was suggested that a much higher efficiency could be achieved by providing for multiple passes of the electron beam through the FEL interaction region. However, the increasing beam energy spread with each pass becomes a limiting factor.

More recently, the Stanford group has collaborated with LURE on an experiment using the ACO storage ring in Orsay, France (Bazin et al., 1982). In this experiment a superconducting undulator ($B_{\perp} = 4$ kG, $L \sim 1$ m) was placed on a straight section of the storage ring, which was typically operated at 150 MeV with a bunch current of ~ 10 mA. An argon laser ($\lambda = 4880$ Å or 5145 Å) having a power density of ~ 1.6 kW/cm² was amplified in the interaction region. The maximum gain reported was $\sim 4 \times 10^{-4}$ per pass, hence oscillator experiments would be extremely difficult with the original apparatus. Consequently, the group is attempting to increase the gain by substituting an optical klystron for the undulator.

Somewhat similar experiments are underway at Frascati using the Adone storage ring (Barbini and Vignola, 1982) and at Brookhaven using the VUV storage ring (Luccio, 1982). Another storage ring FEL experiment has been proposed for BESSY in Berlin (Gaupp, 1982).

Another set of similar experiments employing rf linacs in conjunction with CO₂ lasers and planar, permanent magnet wigglers have recently been undertaken. These experiments were initiated at Los Alamos, TRW, and Math Sciences Northwest. The permanent magnet wigglers used in these experiments are convenient for studying variable wiggler efficiency enhancement schemes by changing either the wiggler period or amplitude with axial distance. In initial experiments, the groups have concentrated on measuring the energy loss of the electrons passing through the interaction region, because the gains or efficiencies are so low that it is very difficult to accurately measure the amplified output signal in the presence of the large input laser signal (20 - 1000 MW).

Based on measurements of electron energy loss, the TRW group has calculated an efficiency of 0.07% and a gain of 2.7% using a wiggler with an amplitude taper of 2.25% (Boehmer et. al., 1982). This efficiency is an order of magnitude higher than the theoretical value with no taper. By using a more powerful laser than the TRW group (1 GW vs 2 MW) the Los Alamos group can achieve high efficiency (~ 2%) but lower gain (Warren et. al., 1982). (Note that the input laser power is not included in the efficiency calculation). The Los Alamos experiment is now being converted to an oscillator mode.

Additional low-current-regime experiments are being performed using microtron accelerators at Bell Labs (Shaw and Patel, 1982) and at Frascati (Bizzarri et al., 1982). These accelerators operate at up to ~20 MeV with peak current of ~ 5 A, and the Frascati microtron is being upgraded to > 30 MeV. Bell Labs is using a 10 m long helical wiggler with a 20 cm period to generate 100 - 400 μ m radiation by tuning the beam energy from 10-20 MeV. Frascati uses a 2.25 m long permanent magnet wiggler with a period of 5 cm for output at ~ 15-20 μ m.

A different, but quite interesting approach is being pursued at the University of California - Santa Barbara (Elias and Ramian, 1982). The UCSB group is using a recirculating electrostatic accelerator to achieve high average power, good beam quality, and high overall FEL efficiency. If all the beam could be recovered, the device could essentially operate dc. The group hopes to use the 2A, 3 MeV electron beam to generate FIR to submillimeter radiation in a single stage FEL, and then to perform a two stage experiment to generate visible to IR output.

High current, relatively low particle energy FEL experiments have achieved impressively high gains and radiation power levels at much lower frequencies than the high particle energy experiments. However, these experiments are characterized by a different set of problems. High current beams are typically produced by Marx-type generators and in general have higher energy spreads than low current beams. Self field effects become important in the propagation of these beams, and the axial magnetic field required to confine the beam can result in large amounts of cyclotron type emission.

The first operation of a device employing what we now call the FEL mechanism was reported over 20 years ago by Phillips (1960). He called the device a Ubitron and built several microwave tube-type versions which behaved impressively in S-band ($\sim 2-3$ GHz). The wiggler typically consisted of alternately wound co-axial coils and the interaction length was ~ 50 cm. Peak microwave output power in excess of 1 MW was achieved using a beam of ~ 150 kV and ≤ 100 A, corresponding to an efficiency of $\sim 10\%$. Scaling this device into the mm wavelength range was restricted at the time because of the limited voltage of available electron guns. However, the introduction of high current, higher voltage Marx type generators made possible a renewed effort in the generation of high power mm waves using this mechanism.

High current (> 1 kA) FEL experiments were originally referred to as stimulated scattering, and their origins can be traced to early experiments at Cornell University and the Naval Research Lab in which large radiated powers were observed when an intense beam was modulated by a slow wave structure or a rippled magnetic field (Nation, 1970; Friedman and Herndon, 1972). These and

similar experiments were interpreted using one of two different theories, the cyclotron maser instability (Sprangle and Manheimer, 1975) and stimulated Raman scattering (Sprangle et. al, 1975), which predicted large growth rates and high efficiencies. The cyclotron maser instability is a purely relativistic effect associated with relativistically gyrating electrons. This mechanism has been successfully used in the development of gyrotrons, relatively compact tube-type devices which operate at the fundamental or harmonics of the cyclotron frequency (See, e.g., Granatstein, ed., 1981). Stimulated scattering experiments, on the other hand, have continued to employ Marx generators at higher voltage and current levels in order to take advantage of the γ^2 frequency scaling and the growth rate scaling with current. After the Stanford group popularized the term "free electron laser" and the equivalence of the FEL and stimulated scattering mechanisms was shown (Kroll and McMullin, 1978; Sprangle et. al., 1979), the high current experiments also began to be referred to as FEL's.

The first high current, relativistic beam experiment to be interpreted as stimulated scattering was performed at the Naval Research Laboratory (Granatstein et al., 1974). In experiments designed to produce microwaves at $\lambda = 2$ cm via the cyclotron maser interaction, strong submillimeter radiation was also observed. A quantitatively consistent explanation was that some of the 2 cm radiation reflected off the output window and subsequently interacted with a sufficiently cold part of the 1.5 MeV beam to produce the high frequency scattered radiation. In a subsequent experiment designed to optimize this effect, 400 μ m radiation was generated at a power of ~ 1 MW (Granatstein et al., 1977).

The next important step in the development of high current FEL's came in an experiment at Columbia University in which the high power electromagnetic pump was replaced by a periodic magnetic wiggler, or quasi-wave (Mross et al., 1976; Efthimion and Schlesinger, 1977). A 750 keV, 5 kA beam was used to generate ~ 10 -100 kW of mm or cm radiation. Subsequent experiments at Columbia increased the millimeter wave power level to more than 1 MW (Marshall et al., 1977a). This group also performed mode structure, spectral, and growth rate measurements which indicated that the mechanism responsible for the observed output was weak pump Raman scattering (Marshall et al., 1977b; Gilgenbach et al., 1979).

These early experiments at NRL and Columbia led to a collaborative effort on NRL's VEBA generator in which a quasioptical cavity was used to provide feedback (McDermott et al., 1978). Approximately 1 MW of 400 μ m radiation was coupled out of the cavity, and the output wavelength agreed with theoretical predictions for the $\gamma = 3.4$ beam. An important result of this experiment was the demonstration of line narrowing when feedback was introduced. The line width decreased from $\Delta\lambda/\lambda > 10\%$ to $\Delta\lambda/\lambda \approx 2\%$.

The efficiency ($< 0.03\%$) of these high current experiments was strongly limited by the poor beam quality. Also, researchers at MIT have shown that the output from such experiments can easily be dominated by cyclotron emission (Shefer and Bekefi, 1982). Consequently, the NRL VEBA group (Parker et al., 1982) designed an improved diode in which 90% of the diode current was removed from the beam with a collimator. The collimated 1.5 kA, 1.4 MeV beam had an instantaneous axial velocity spread of $\sim 0.1\%$. The beam was passed through a helical wiggler and generated ~ 35 MW of radiation at

$\lambda = 4$ mm. This power was $\sim 2.5\%$ of the propagated beam power. A strong frequency dependence of the output on the axial guide field was observed, with the highest output occurring at a field slightly above the cyclotron resonance.

Another recent collective regime experiment at Columbia University has been reported in which the electrons were given an initial transverse velocity before their injection into the wiggler (Grossman et. al., 1983). Output was observed at a frequency equal to the sum of the doppler shifted cyclotron and usual FEL frequencies; i.e., $\omega_o = 2\gamma_z^2 (\Omega_o/\gamma + k_w v_z)$. In this experiment, < 1 MW of power at $\lambda = 1.5$ mm was generated. This mechanism was independently proposed by the MIT group, which called it a Lowbitron (McMullin and Bekefi, 1981), and experiments to study the effect are also underway there.

Finally, an important trend that is occurring in FEL research is an attempt to bridge the gap between the two current regimes. High current experiments are being scaled to higher voltages in an attempt to produce higher output frequencies and/or higher powers. In an experiment being undertaken on the ETA induction linac ($V \sim 4.5$ MV) at Livermore, a high current beam (~ 1 kA) is being used in an attempt to efficiently generate very high FEL output powers at $f \sim 100$ GHz (Prosnitz and Sessler, 1982). At the Naval Research Laboratory, a program is underway to develop compact high current, and high voltage accelerators, which could be used as FEL drivers (Roberson et al., 1982). The long pulse duration experiment reported here is part of that program and is scalable to high energies.

IV. FEL Operating Regimes

There are three regimes of free electron laser operation. The operating regimes can be characterized, in part, by the velocity distribution relative to the phase velocity of the pondermotive wave. A phase space plot is shown in Figure 1.

In the Raman regime the beam appears cold to the pondermotive wave. There are no particles in resonance with the wave. The amplitude of the wave is too small to trap any beam particles at $z=0$. As the wave grows in space, the amplitude becomes large enough to trap the beam particles, thus terminating the linear growth phase.

In the kinetic Compton regime, the beam appears warm to the pondermotive wave. There are particles in resonance with the pondermotive wave. The linear growth is proportional to the slope of the distribution function. This is a Landau type growth mechanism. Kinetic theory is required to describe the FEL process in this regime. The pondermotive wave is resonant with a range of particles, as indicated by the dashed lines in the figure. The growth mechanism of the FEL in this regime has a quantum mechanical analogy with Compton scattering. It is not a single particle effect, since it requires a kinetic description, and so it is referred to as kinetic Compton. The phase space plot shows the growth of the wave in space. Initially the wave amplitude is small compared to the width of the resonance. The pondermotive wave will grow until the amplitude becomes large enough to trap the resonant particles, thus terminating the linear growth phase.

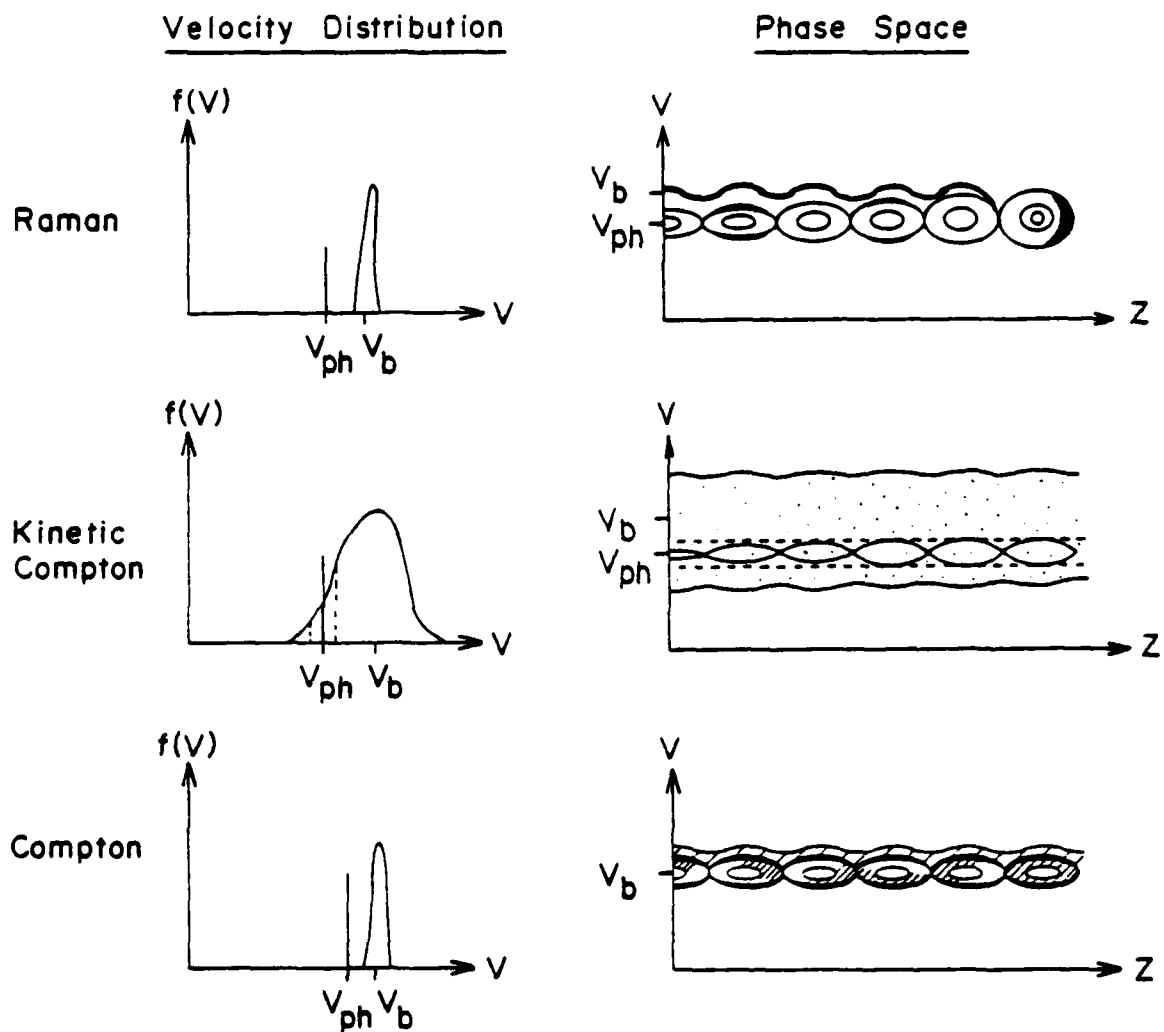


Figure 1. Velocity distributions and phase space plots of the three FEL operating regimes.

In the Compton regime, the beam energy is high and the current low. Single particle effects dominate over collective effects. The phase velocity of the pondermotive wave is less than the beam velocity. There are two modes in which a single particle Compton FEL may be operated. If the amplitude of the pondermotive wave is too small initially to trap the beam particles, as in the Stanford experiment, the gain is due to the perturbation of beam particles by the pondermotive wave. The interchange between wave and particle energy is oscillatory at the same period as the pondermotive wave. These particles are represented by a shaded region above the pondermotive wave ellipses in Fig. 1.

If the wave amplitude is sufficiently large, as in the Los Alamos experiment (Warren et. al., 1982), some or all of the beam particles may be trapped in the potential well of the pondermotive wave. The gain of the FEL in this region is due to the loss of particle energy as the particles rotate in the potential troughs of the pondermotive wave. This occurs at the trapped particle bounce frequency. The maximum gain is obtained when the beam particles are at the bottom of the ellipse in phase space.

The efficiency of the free electron laser can be increased in all of these schemes by decreasing the phase velocity of the pondermotive wave after it has trapped the beam particles. The decrease in particle energy appears as an increase in wave energy.

To operate a high current beam in the Raman regime requires

$$\frac{\Delta\gamma}{\gamma} < \frac{\omega_b}{\gamma^{3/2} c k_w} \quad (10)$$

where ω_b is the beam plasma frequency (Sprangle et al., 1979). Combining this with $\lambda = \lambda_w / 2\gamma^2$ gives

$$\lambda > \frac{c\pi}{\omega_b \gamma^{1/2}} \cdot \frac{\Delta\gamma}{\gamma} \quad (11)$$

This condition can be shown to be equivalent to requiring $\lambda' > \lambda'_D$, where λ' and λ'_D are the wavelength and Debye length in the beam frame (Hasegawa, 1978). The energy spread $\Delta\gamma/\gamma$ which results from the normalized emittance ϵ_n of a beam with radius r_b is (Neil, 1977)

$$\frac{\Delta\gamma}{\gamma} = \frac{1}{2} \frac{\epsilon_n^2}{r_b^2} \quad (12)$$

The Lawson-Penner relation which relates the emittance to the beam current is

$$\epsilon_n^2 = S^2 I(\text{kA}) (\text{cm} - \text{rad}) \quad (13)$$

where S is a scale factor that is typically 0.1 - 0.3 for existing accelerators.

Combining these equations we find for a Raman interaction, that

$$\lambda(\text{cm}) > 5.7 \frac{S^2}{\gamma^{1/2}} J^{1/2} (\text{kA/cm}^2) \quad (14)$$

At a current density of 1 kA/cm² and $S = 0.3$ the wavelength must be greater than 0.3 cm to operate in the Raman regime when $\gamma = 3$. To operate a 1 micron FEL in the Raman regime for such a beam would require $\gamma = 2600$, or

1.3 GeV, and a wiggler with a wavelength of 135 meters. Consequently, the Raman FEL is not viable in the IR region unless S can be greatly reduced.

It is clear from Eq. 14 that there are three parameters one can improve upon to extend the Raman region. The kinetic energy of the beam can be increased, the current density decreased or the scale factor in the emittance relation decreased. However, there is a limit to the extent one can increase the energy, decrease the current density and maintain a collective interaction. When the number of particle in the debye sphere is small, the system will not support collective oscillations.

The wavelength condition of Eq. 14 is most sensitive to S, so it is important to analyze the degree to which S can be reduced. The Lawson-Penner relation is not derived from first principles but is a phenomenological relation which has been shown to hold in many accelerators. The success of the Lawson-Penner relation is related to the fact that the reliable current density from oxide thermionic cathodes is generally $< 10 \text{ A/cm}^2$. With higher current density cathodes, the scale factor, S, can be reduced considerably. In a recent experiment using cold graphite cathodes, an S parameter of 0.12 was obtained with a 14 kA beam by aperturing the beam to about 30 percent of the diode current (Sloan et al., 1982). An S parameter of .13 at 4 kA was obtained by aperturing to about 25% of the current from a spiral knife-edge cold cathode in a 20 MeV induction linac (Kulke et al., 1981). Finally, a much reduced value of $S = 0.04$ at 1.5 kA was calculated for a recent experiment in which only $\sim 5\text{-}10\%$ of the current from a graphite cold cathode was extracted from the diode (Parker et al., 1982).

The S parameter is best understood in terms of the brightness, another invariant that is related to the emittance:

$$B_n = \frac{I}{\pi^2 \epsilon_n^2} = \frac{1}{\pi^2 S^2} = \frac{J}{2\pi \Delta Y / \gamma} \quad (15)$$

Thus, the brightness is a measure of our ability to make a high current density, cold beam. To the extent that the emittance is an invariant, the brightness is determined at the diode; hence if we compress the beam at a later stage we increase $\Delta Y / \gamma$. Therefore, for high power operation it is desirable to have a high current density cathode. From the above three experiments we can conclude that the brightness of cold cathodes with appropriate aperturing is a factor of six to sixty higher than that of hot cathodes. This will extend the Raman wavelength region by a corresponding amount. However, the price one pays for cold cathode operation is diode closure. This can limit the pulse length to a few hundred nanoseconds. In addition, the efficiency of the system is reduced by a factor of 5 to 10 when a large fraction of the beam is terminated by aperturing.

The emittance is often the dominant contributor to energy spread. However, the self potential and the wiggler gradient can also contribute to the beam energy spread, which in general is given by

$$\frac{\Delta Y}{\gamma} = \frac{1}{2} \frac{\epsilon_n^2}{r_b^2} + \frac{1}{\gamma_0} \left(\frac{r_{b,w}}{2c} \right)^2 + \left(\frac{r_{b,w}}{2c} \right)^2, \quad (16)$$

where the second term is the contribution from the self potential and the third is from the wiggler gradient. From this we can find an optimum radius of

$$r_b^4 = \frac{2c^2 \epsilon_n^2}{\omega_b^2 / \gamma_0 + \Omega_w} \quad (17)$$

For high current beams propagated in a strong axial magnetic field, the equilibrium radius (Neil, 1977) should be compatible with the optimum radius.

The variation in γ as determined by the emittance, wiggler gradients and self field of the beam results in a velocity spread of the beam that is independent of time. If the diode voltage is time dependent (as for example due to diode closure), this will shift the output wavelength. If the gain is sufficiently high in an oscillator the time variation will cause a broad band output. The time variation in an amplifier experiment can cause a loss of resonance with the input signal. The range of unstable wave numbers is (Sprangle et. al., 1979)

$$\Delta k = 8 k_i^2 / k \quad (18)$$

where k_i is the spatial growth rate. This can be related to the variation in γ through $\lambda = \lambda_w / 2\gamma^2$. Then $\frac{\Delta \gamma}{\gamma} \Big|_t < 4 k_i^2 / k^2$ is required. Substituting

the maximum growth rate value for k_i^2 we get

$$\left. \frac{\Delta\gamma}{\gamma} \right|_t < 2\gamma^{1/2} \frac{\Omega_w^2 \omega_b^2}{(2\pi c)^3} \lambda^3 \quad (19)$$

Therefore, the requirements on the time variation of the beam energy to keep the growth of the output wavelength in the unstable region is proportional to λ^3 . For a 1 kA/cm², 1 MeV beam in a 1 kG wiggler field an output wavelength of 0.7 mm requires a $\Delta\gamma/\gamma$ time variation of less than 1%.

V. Accelerator Development

During the past fifty years accelerators have developed primarily along two directions: (1) low current, high voltage and (2) high current, low voltage devices. Consequently FEL research has followed similar lines. The history of traditional accelerators is quite well known. The average current in these accelerators is generally less than an ampere with micro bunch currents reaching tens of amperes. The energies achieved in electron linacs exceeds 10^{10} eV and the beam energy in a proton synchrotron is approaching 10^{12} eV. High current accelerators have been developed primarily as Marx generators driving a pulse forming line, which is connected to a diode. The energy of these devices is typically around 1 MeV, although 10 MeV devices have been built. The pulse current from a pulse-power line diode has reached 10 MA. These devices do not scale well in energy because the total energy is achieved in a single gap, hence the stress on the insulator becomes excessive at high voltages. A free electron laser requires high voltage for

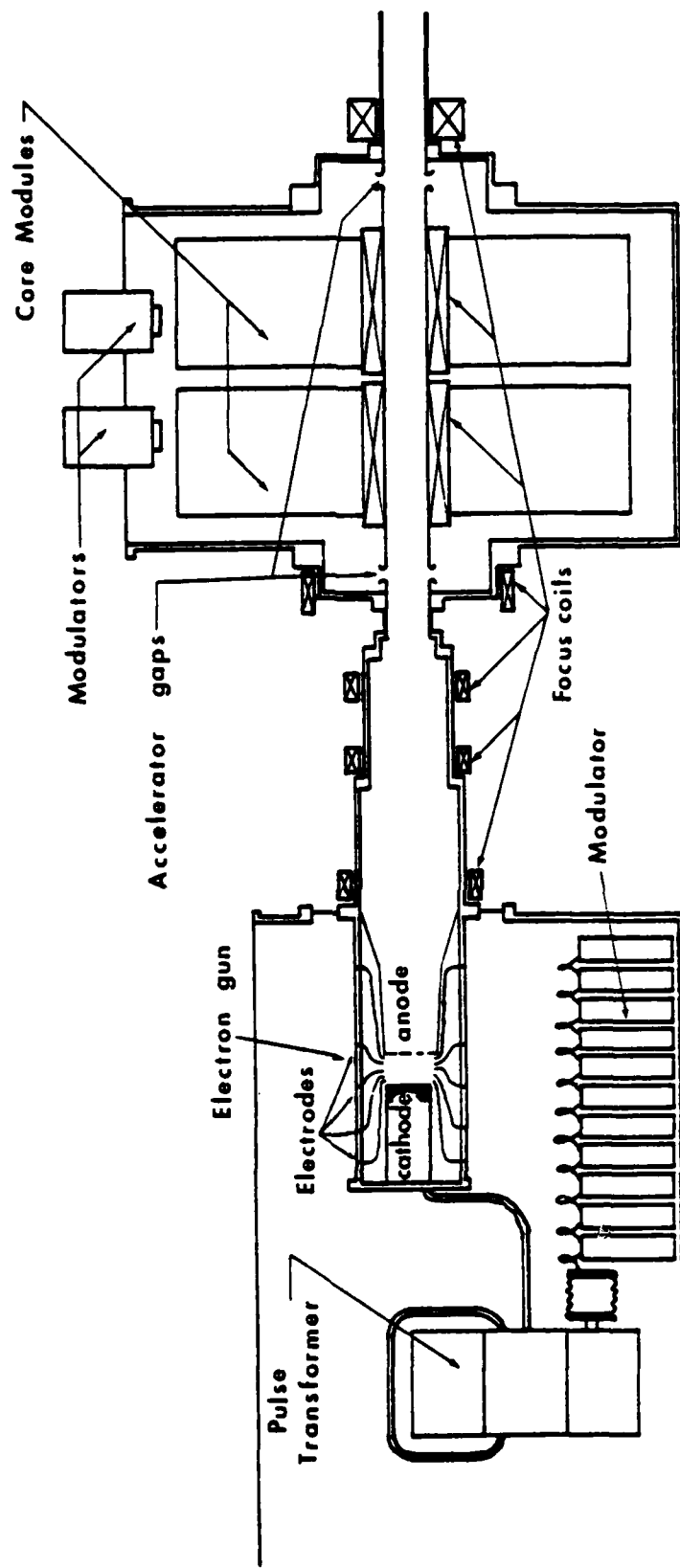
short wavelength operation and high current for efficiency and high gain. Only the induction linac has been a serious candidate as a FEL driver in this parameter range. Experiments at Lawrence Livermore Laboratory on the Experimental Test Accelerator (ETA) have achieved currents approaching 10 kA and beam energies of 5 MeV. A scaled up version of this accelerator is designed for 50 MeV, 10 kA, 30 ns operation. The current from this device is probably excessive for efficient FEL operation and the pulse length too short.

A long pulse induction linac ($\tau = 2 \mu\text{sec}$) was built at the National Bureau of Standards (Leiss, et al., 1980) and is currently in operation at the Naval Research Laboratory. Figure 2 is a schematic of the Long Pulse Induction Linac. The accelerator consists of two major components; (1) an injector and (2) an induction accelerator module.

The electron gun in the injector has a 16.5 cm diameter tungsten dispenser thermionic cathode. Electrons are accelerated in the gun through a series of 12 annular electrodes, spaced by ceramic insulator rings. The last electrode supports a 95% transmission tungsten mesh at ground potential. The gun has also been operated with a graphite brush cold cathode (Ramirez and Cook, 1980; Prohaska and Fisher, 1982).

The electron gun is immersed in an oil filled tank. The gun voltage is fed from a pulse line driving a 12:1 step up transformer. The injector typically produces a 0.8 kA beam pulse of 400 keV. The electron beam is transported to the induction accelerator module by a series of focusing coils.

INDUCTION LINAC



$V = 0.8 \text{ MV}$
 $I = 0.8 \text{ kA}$
 $\tau \sim 2.0 \mu\text{s}$
 $N \sim 10^{16} \text{ particles}$
 $\frac{\Delta V}{V} \sim 3\%$

Figure 2. Schematic of Long Pulse Induction Linear Accelerator.

The induction accelerator module consists of two core sets. One of the core sets give a 4 to 1 step up voltage and the other a 5 to 1. The cores are wound with 0.001 inch mild steel foil, separated by 0.00025 inch mylar sheets. Each accelerating gap produces about 200 kV of acceleration.

Typically, the output energy of the electron beam generated by the linac is 0.8 MeV, the current approximately 0.8 kA and the pulse length 2 μ sec. However, for the data reported in this work one of the accelerating gaps was not operating, so the beam voltage was 0.55 MeV. Also, a graphite brush cold cathode was used and the 0.8 kA diode current was reduced to 0.2 kA due to losses in beam transport. The temporal variation in the voltage with the hot cathode is less than 3 percent over 1.6 μ sec. This is the longest pulse induction linac in existence, with a pulse duration more than an order of magnitude longer than other induction linacs. The pulse length becomes an important consideration for free electron laser experiments where one wishes to study the nonlinear dynamics of the beam or efficiency enhancement schemes. Applications that require a significant amount of energy in the radiation field also require long pulses to avoid the problems encountered with excessive electric field strengths at short pulses.

Figure 3a shows the voltage and current traces of the injector for the long pulse induction linac. The voltage remains constant to within a few percent over the 2 microsecond pulse length. In contrast Figure 3b shows the voltage and current from the graphite cathode diode of the Febetron, a relatively long pulse Marx type generator. The oscillations on the voltage and current are due to the finite element pulse line of the Febetron Marx. The diode voltage decreases 25 percent in 250 nsec as a result of diode

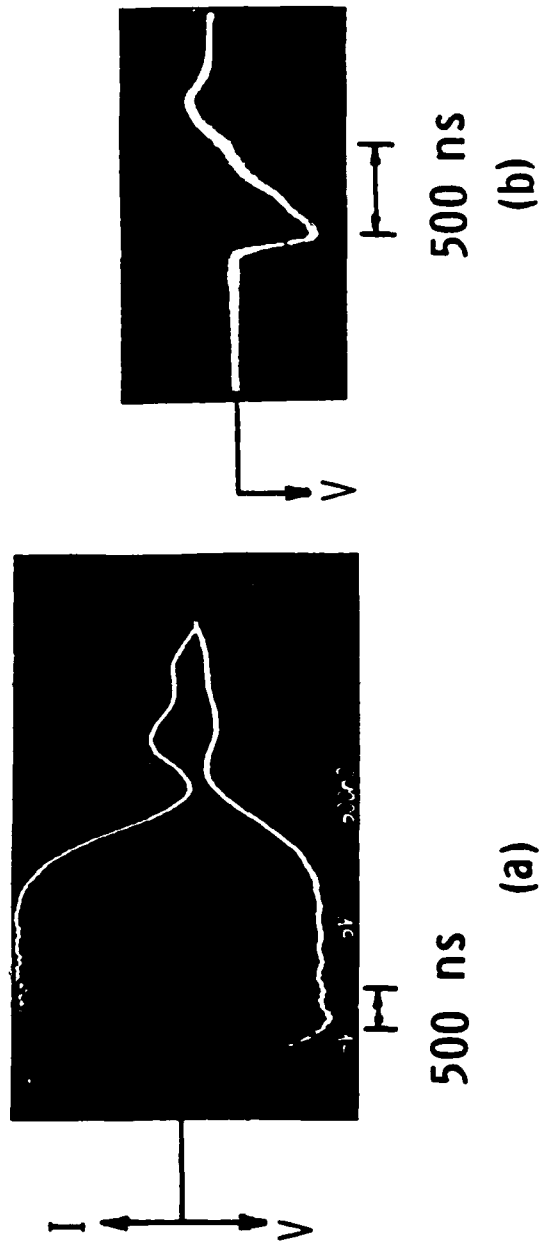


Figure 3. Comparison of diode waveforms with hot (a) and cold (b) cathodes.

closure. This closure-induced voltage collapse is typical of cold, plasma cathodes, and in light of the condition of Eq. 19, is a key problem for long pulse FEL operation. Efforts to prevent diode closure, such as magnetic insulation, generally result in higher beam emittance.

The relationship between the cathode plasma velocity and the diode parameters can be determined by considering the simple circuit shown in Fig. 4. There is a voltage source V_c , an internal line impedance Z_L , and a time dependent diode impedance $Z_D(t)$. The current is

$$I = V_c / (Z_L + Z_D). \quad (20)$$

The diode voltage is

$$V_D = I Z_D = V_c Z_D / (Z_L + Z_D) \quad (21)$$

and the diode impedance is

$$Z_D = \frac{a d^2(t)}{v_D^{1/2}}, \quad (22)$$

where a is a constant and d the anode cathode spacing. We will assume

$$d = d_0 - \alpha t \quad (23)$$

where α is the plasma closure velocity. The closure velocity for high current cold cathodes is typically ~ 2.5 cm/ μ s. Now if we differentiate Eq. (21)

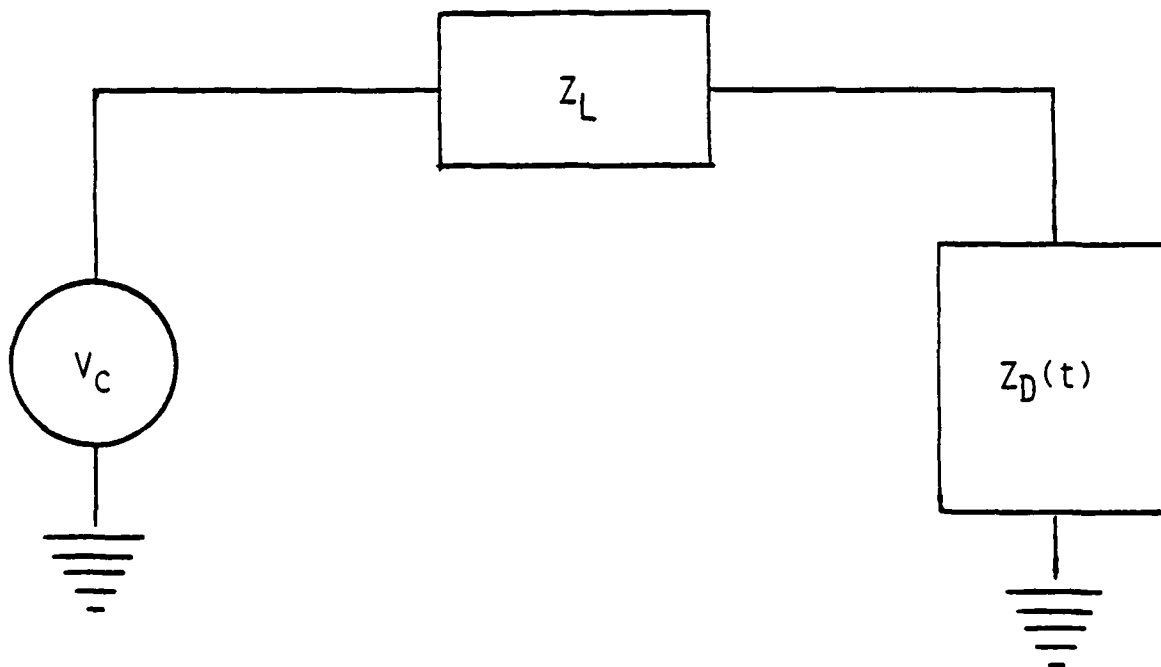


Figure 4. Idealized circuit diagram of an electron beam generator. Source voltage V_c appears across line impedance Z_L in series with diode impedance Z_D .

with respect to time and assume the diode impedance is matched to the line at $t = 0$, then $V_C = 2 V_D$ and

$$\frac{\Delta V_D}{V_D} = \frac{1}{2} \frac{\Delta Z_D}{Z_D} \quad (24)$$

$$\Delta Z_D = \frac{2ad\Delta d}{V_D^{1/2}} - \frac{1}{2} \frac{ad^2 \Delta V_D}{V_D^{3/2}} \quad (25)$$

Then

$$\frac{\Delta V_D}{V_D} = \frac{4}{5} \frac{\Delta d}{d} \quad (26)$$

and

$$V_D(t) = V_D(0) \left(\frac{d}{d_0} \right)^{4/5} = V_D(0) (1 - \alpha t/d_0)^{4/5} \quad (27)$$

Hence for a diode that is initially matched we can obtain a simple expression for the time dependence as a function of diode spacing.

Figure 5 is a plot of the diode voltage as a function of time for $Z_L = Z_D$, $Z_L = 10 Z_D$ and $Z_L = 0.1 Z_D$ when $t = 0$. When the line impedance is ten times the diode impedance, the device tries to behave as a constant current source and the voltage decays faster than in the matched load case. When the line impedance is small compared to the diode impedance, the device tries to act as a constant voltage source at the expense of an increased current. However,

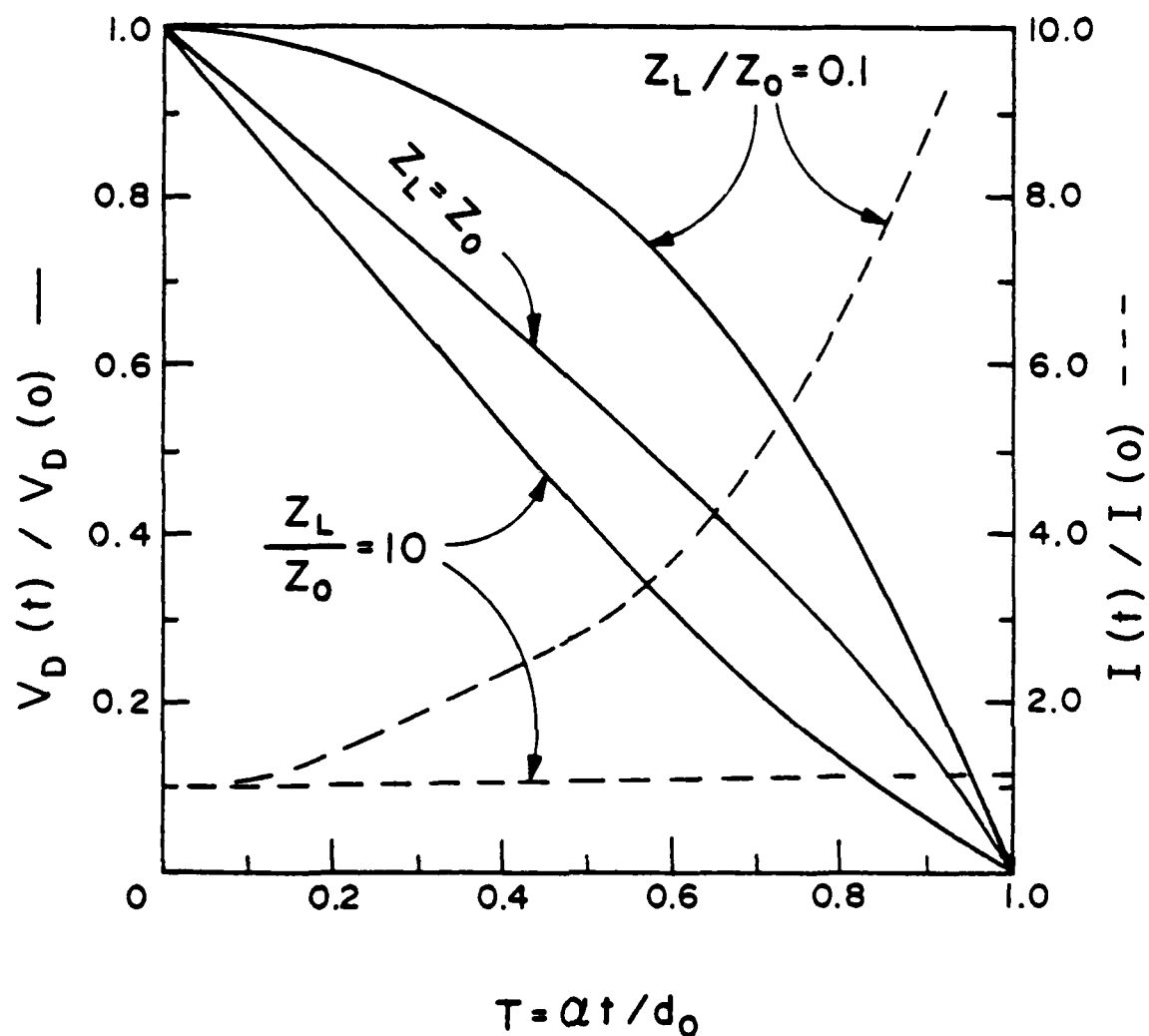


Figure 5. Calculated diode voltage and current for three different diode impedances. The line impedance is Z_L and Z_0 is the diode impedance at $t = 0$.

for high current beams, the increasing self potential of the beam with current will cause the beam's kinetic energy to decrease faster than the diode voltage.

Although diode closure in high current cold, cathode machines is a limiting factor for long pulse operation, there are many operational advantages to cold cathodes. Thus, we have temporarily replaced the hot cathode in the induction linac with a graphite brush cold cathode of the same area. The average electric field at the cathode surface is about 30 kV/cm. The cathode rapidly turns on, and the closure problem does not seem to be as severe as in the Febetron. Perhaps the large area, low current density reduces the closure velocity. The emittance is worse than with the hot cathode, and more of the beam is lost in transport. However, the emittance of the beam transported to the wiggler appears to be about the same as with the hot cathode.

VI. The FEL Apparatus

Figure 6 is a sketch of the free electron laser experiment. There is a uniform axial field of 120 cm length which is varied from 1 to 5 kG, with a typical operating field of 2 kG. The beam from the induction linac is focused into the solenoid. The experiment has not yet been run with the mirrors in place as shown, but operated in a superradiant mode.

Two wiggler configurations have been investigated: (1) a pulsed linear wiggler and (2) a radially symmetric diffusive wiggler. The amplitude of the linear wiggler field can be varied from 0.1 kG to 1 kG. The wiggler

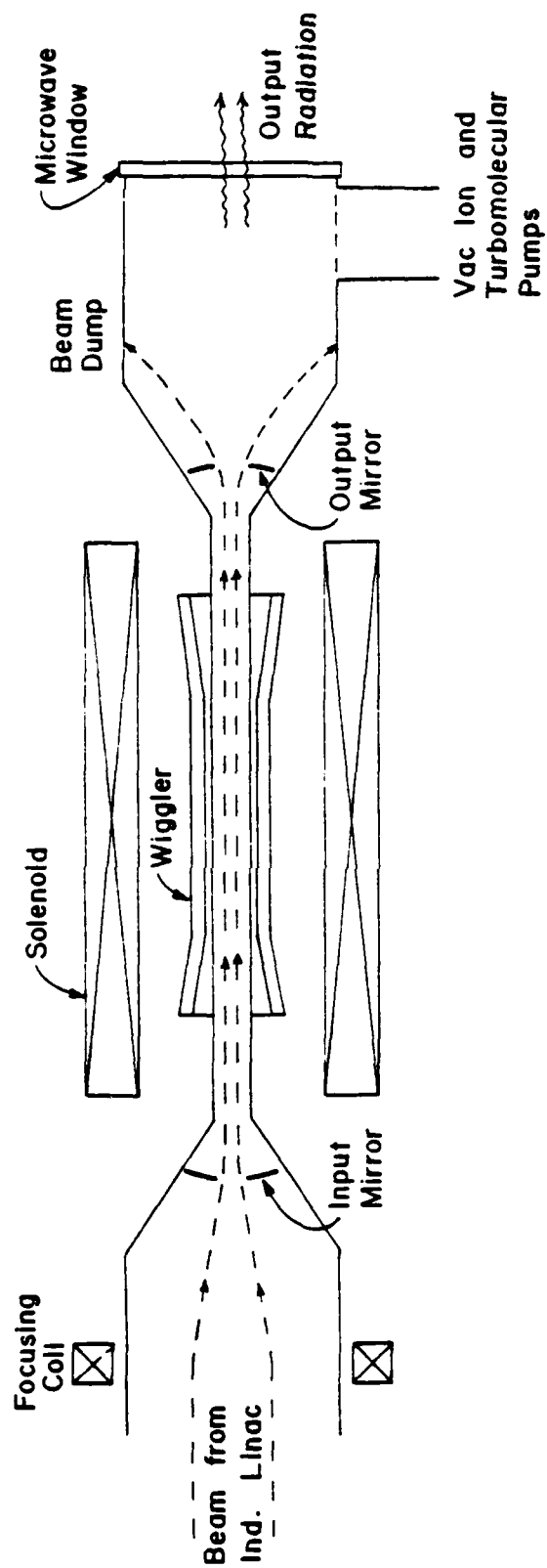


Figure 6. Schematic of FEL interaction region.

wavelength in 3.0 cm, and the overall length of the wiggler is 120 cm. The wiggler amplitude rises adiabatically in 30 cm, has a uniform straight section of 60 cm and decays adiabatically in the last 30 cm.

Two diffusive wigglers have been used: a 6 cm period aluminum wiggler and a 4.5 cm copper wiggler. The perturbed axial component of the on-axis field is 4 percent of the axial field for the 6 cm wiggler and 6 percent for the 4.5 cm wiggler.

The output radiation is extracted through a large area window, and the power and spectrum are determined by gas breakdown thresholds or with high pass filters and calibrated detectors.

A. Linear Wigglers

There are several advantages to linear wigglers, including ease of assembly, changing the periodicity to operate at different wavelengths, and tapering the period and/or field amplitude for efficiency enhancement (Sprangle et al., 1979). As a result of our experiments and analysis, we find that a linear wiggler in an axial guide field produces an elliptical polarization. The ratio of the major to minor axis of the ellipse is $k_w v_z / \Omega_0$, where k_w is the wiggler wave number, v_z the axial beam velocity, and Ω_0 the cyclotron frequency in the axial guide field. As a result of the asymmetry of the wiggler, there are no focusing forces in one of the directions perpendicular to the beam propagation and an electron drift results. Although this drift can be very small in some parameter regimes, it is always present in linear wigglers immersed in an axial guide field unless additional focusing

forces are provided. This problem was avoided in a high current device using a linear wiggler by eliminating the solenoidal field (Phillips, 1960). Focusing was provided by increasing the wiggler field at the edges.

To understand how the elliptical polarization and perpendicular drift arise, we will solve the equations of motion in the combined wiggler and axial fields. The linear wiggler field components are

$$B_{wx} = 0$$

$$B_{wy} = b(z) B_w \cosh k_w y \cos k_w z \quad (28)$$

$$B_{wz} = - b(z) B_w \sinh k_w y \sin k_w z$$

where B_w is the peak wiggler field on axis and $b(z)$ is an adiabatic taper in the wiggler amplitude at the entrance and exit of the wiggler. The amplitude increases to its full value in ten periods in our experiment.

We define $\Omega_0 = qB_0/\gamma m$ and $\Omega_w = qB_w/\gamma m$. To simplify the analysis we will make the following assumptions

$$\frac{B_w}{B_0}, \frac{v_x}{v_z}, \frac{v_y}{v_z}, k_w y \ll 1 \quad (29)$$

and $v_z = v_b = \text{constant}$. The single particle equation of motion then gives

$$\dot{v}_x = (\Omega_0 v_y - \Omega_w \cosh k_w y \cos k_w z v_z)$$

$$\dot{v}_y = -v_x \Omega_0 \quad (30)$$

$$\dot{v}_z = v_x \Omega_w \cosh k_w y \cos k_w z$$

where we have neglected the correction to B_z from the wiggler since $B_w/B_0 \ll 1$ and $v_y \ll v_z$.

We take the derivative of each of the components with respect to time and use the assumptions of Eq. 29 to get

$$\ddot{v}_x + \Omega_0^2 v_x = \Omega_w k_w \cosh k_w y \sin k_w z v_z^2. \quad (31)$$

Similarly

$$\ddot{v}_y + \Omega_0^2 v_y = \Omega_0 \Omega_w \cosh k_w y \cos k_w z v_z \quad (32)$$

We have the following solutions

$$v_x = \frac{\Omega_w k \cosh k_w y \sin k_w z v_z^2}{\Omega_0^2 - k_w^2 v_z^2}$$

$$v_y = \frac{\Omega_0 \Omega_w \cosh k_w y \cos k_w z v_z}{\Omega_0^2 - k_w^2 v_z^2}$$

$$x = \frac{\Omega_w v_z \cosh k_w y \cos k_w z}{\Omega_0^2 - k_w^2 v_z^2}$$

(33)

$$y = \frac{\Omega_o \Omega_w \cosh k_w y \sin k_w z}{k_w (\Omega_o^2 - k_w^2 v_z^2)}$$

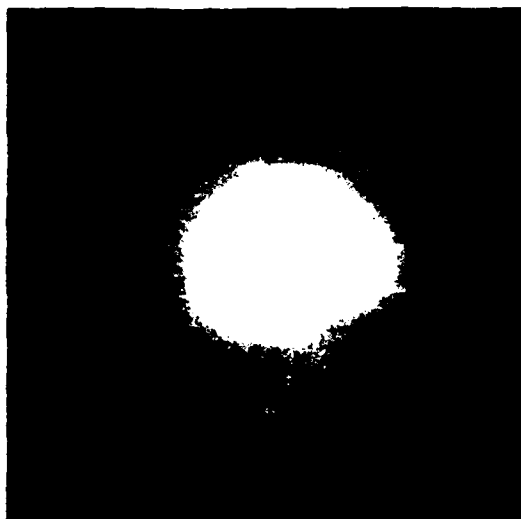
The displacement in the x direction is proportional to the wiggler field and axial velocity. The displacement in the y direction occurs only if there is a nonzero solenoidal magnetic field. It is proportional to both the solenoidal and wiggler field. This displacement is a result of the Lorentz force arising from the x-component of v_w and B_o .

The ratio of the maximum excursion in the x-direction to that in the y-direction is seen from Eq. 33 to be

$$\Delta x / \Delta y = k_w v_z / \Omega_o. \quad (34)$$

Thus, this ratio is a measure of how close Ω_o is to the cyclotron resonance which occurs at $\Omega_o = k_w v_z$. Since $k_w v_z$ is approximately constant in the experiment, the ratio of the maximum displacements $\Delta x / \Delta y$ should vary as $1/\Omega_o$.

Figure 7 is a series of exposures made from x-rays produced when the beam strikes a target placed beyond the wiggler. These photos give us the shape of the beam versus solenoidal field. In Fig. 7(a), the wiggler field is zero and the beam is approximately circular. In Fig. 7(b), with a 500 Gauss wiggler field the beam becomes elongated in the x-direction. The linear wiggler field is in the y direction, consistent with the above analysis. As the solenoidal field is increased with the wiggler field constant, the shape goes from



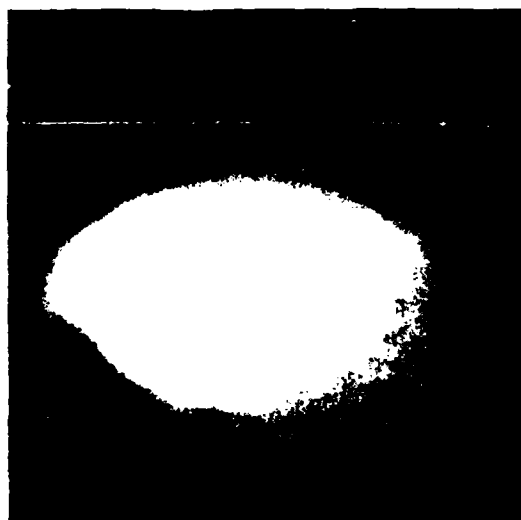
$B_0 = 1.74 \quad B_W = 0$

(a)



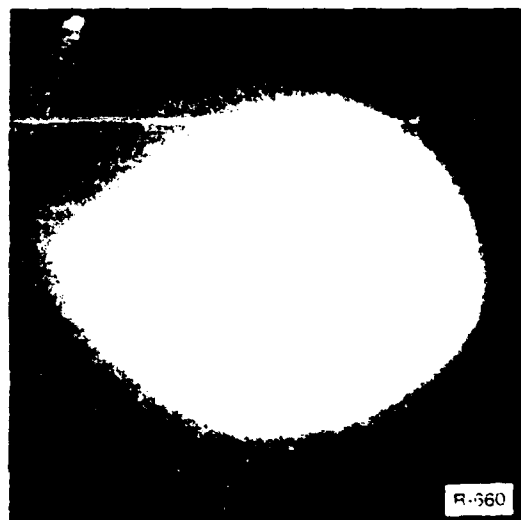
$B_0 = 1.74 \quad B_W = 0.5$

(b)



$B_0 = 2.6 \quad B_W = 0.5$

(c)



$B_0 = 3.48 \quad B_W = 0.5$

(d)

Figure 7. Time integrated x-ray exposure of beam striking a target placed beyond linear wiggler (wiggler field is vertical) for various values of solenoidal field.

elliptical to circular, as shown in Figs. 7(b) - 7(d). Hence, we would expect a nearly linearly polarized output for (b) and a nearly circular polarization for (d).

Figure 8 is a plot of the ratio $\Delta x/\Delta y$ as a function of the solenoidal field. The results are plotted three ways. The solid line is the theory, the small dots were computed numerically and the circled x points are experimental. At small values of magnetic field the approximations break down and there is a large variation in the results.

We have demonstrated that the polarization of a linear wiggler in a solenoidal magnetic field may be varied by changing the magnitude of the solenoidal field. In addition, we see from Eqs. 34 that a change in the amplitude of the wiggler field alone does not change the polarization. We have confirmed this by propagating a beam the entire length of the wiggler in a solenoidal magnetic field of 2 kG. The wiggler field is varied up to 1 kG without changing the shape or intensity of the beam.

As a result of the asymmetry of the wiggler, there are no focusing forces in the x-direction. This results in a net drift of off axis particles (Pasour et al., 1982). This drift is shown clearly in Fig. 9, which consists of electron trajectories in the x-y plane. The trajectories are calculated by numerically solving the equations of motion, including self-fields. Initially the electrons $\vec{E} \times \vec{B}$ drift azimuthally as they are injected into the adiabatically increasing wiggler field. However, when they reach the constant amplitude portion of the wiggler, the electrons drift rapidly in a direction perpendicular to both the axial and wiggler fields.

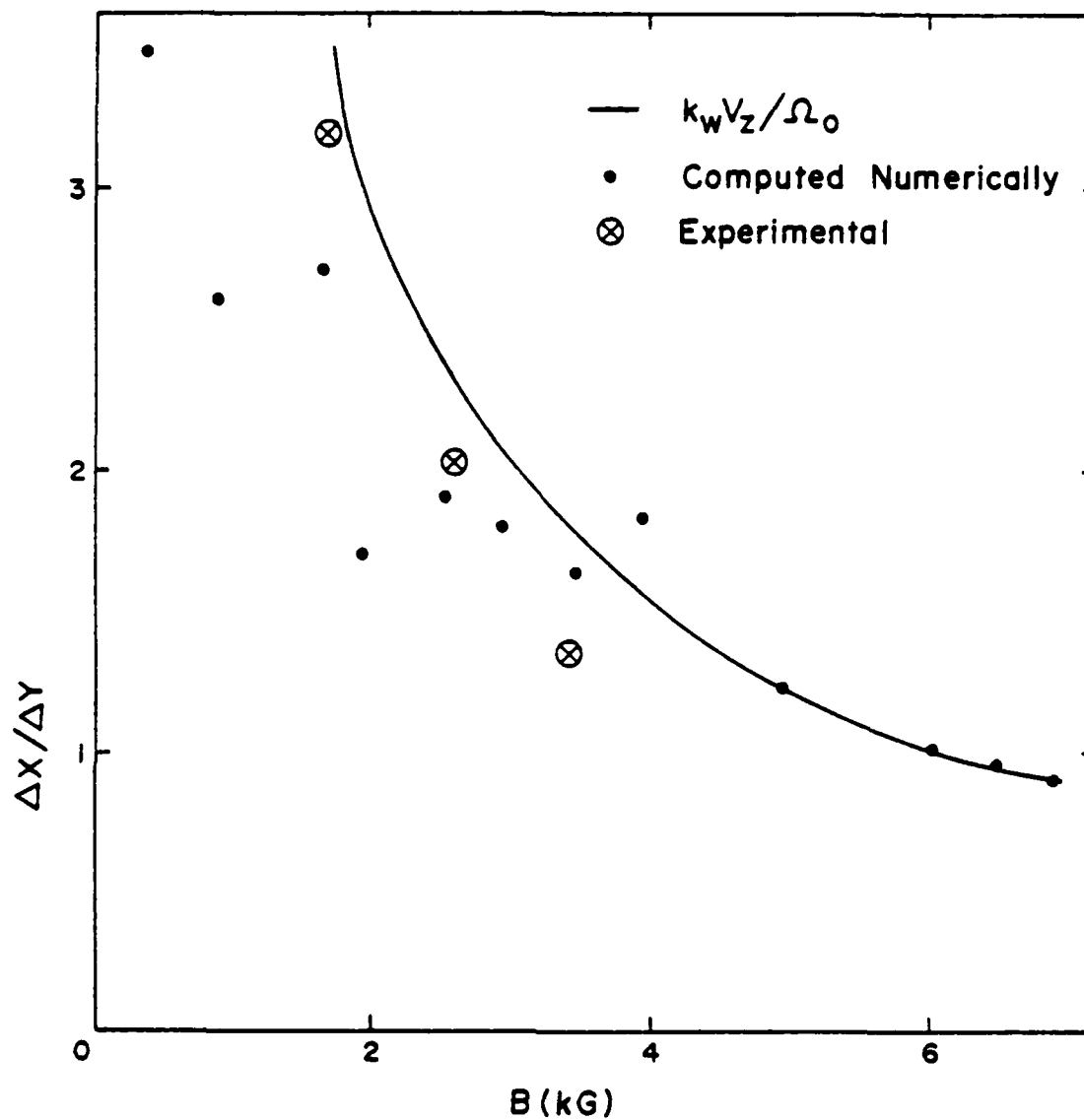


Figure 8. Plot of beam elongation ($\Delta x / \Delta y$) vs. axial magnetic field in a linear wiggler (B_w in y-direction). Solid line is theoretical curve (Eq. 34), dots are values obtained by numerical integration of orbit equations, and crosses are experimental results.

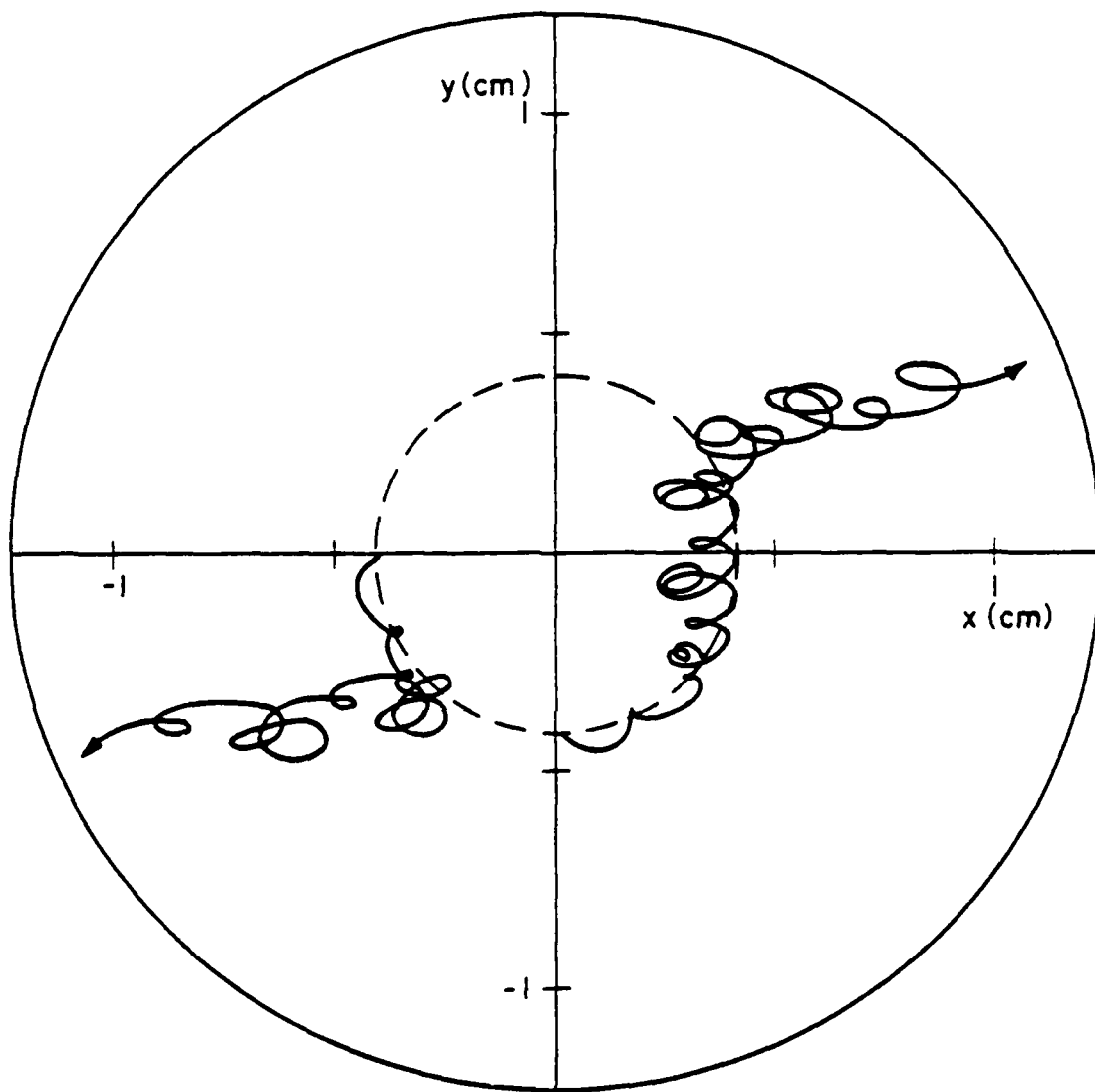


Figure 9. Electron trajectories in a linear wiggler and an axial magnetic field. In this case, $B_w = 1$ kG, $B_o = 250$ A, $\lambda_w = 3$ cm, and $\gamma = 2.2$.

An approximate, empirical expression for the drift has been found which is in good agreement with results from computer calculations of the electron orbits when $\Omega_w < \Omega_o < kv_z$. In terms of the wiggler gradient, the expression is

$$\vec{v}_d = \frac{1}{2} \frac{v_{\perp}^2}{\Omega_o} \cdot \frac{\nabla(\vec{B}_w)^2}{2(\vec{B}_w)^2} \times \frac{\vec{B}_o}{B_o}, \quad (35)$$

where $v_{\perp}^2 = v_x^2 + v_y^2$. This expression has the same form as the usual grad B drift and can be thought of as arising from the crossed wiggler gradient and axial field. It can also be written as

$$v_d = \frac{1}{2} v_z \frac{k_w v_z}{\Omega_o} \cdot \frac{(\Omega_w k_w v_z)^2 \cosh k_w y \sinh k_w y}{(\Omega_o^2 - k_w^2 v_z^2)^2} \quad (36)$$

This expression is reasonably valid for $k_w y \leq 0.8$, $B_{wy} \gg B_{wz}$, and

$v_{\perp} \ll v_z$. Note that the drift is very small near the axis but increases exponentially with $k_w y$.

Table 1 compares drift velocities for various cases as calculated by the computer trajectory code to those calculated from the Eq. 36. In general the agreement is very good. One consequence of the large drift near resonance is that it limits the degree of gain enhancement achievable through the magneto-resonance effect.

TABLE I

Comparison of drift velocities computed from the code with those from Eq. 9 for various cases.

B_o (kG)	B_w (kG)	γ	$\frac{\Omega_o}{kv_z}$	X (cm)	$\frac{v_d}{c}$ (code)	$\frac{v_d}{c}$ (Eq. 9)
2	1	2.2	0.29	0.4	0.047	0.050
4	1	2.2	0.57	0.4	0.042	0.046
2	0.5	2.2	0.29	0.4	0.011	0.013
2	1	2.2	0.29	0.2	0.019	0.022
2	1	3.0	0.21	0.4	0.029	0.034
4	1	3.0	0.42	0.4	0.019	0.022
4	0.5	3.0	0.42	0.4	0.0051	0.0056
4	1	10.0	0.11	0.4	0.0043	0.0049
10	5	10.0	0.28	0.4	0.057	0.056

B. Helical Wiggler

Because the linear wiggler drift is so sensitive to slight off-centering or large diameter of the beam, a helical wiggler would seem to be somewhat better suited to the experiment, at least initially when beam focusing is not optimized. If the trajectory calculation is repeated with the same parameters as those in Fig. 9 but with a helical wiggler substituted for the linear one, it is found that the electron drifts azimuthally and is well confined, as shown in Fig. 10 (Pasour et al., 1982). This behavior results from the radially increasing wiggler field, which for $k_w r \lesssim 0.8$ can be written as (Blewett and Chasman, 1977)

$$B_r = B_w \left(1 + \frac{3}{8} k_w^2 r^2\right) \sin(\theta - k_w z)$$

$$B_\theta = B_w \left(1 + \frac{1}{8} k_w^2 r^2\right) \cos(\theta - k_w z) \quad (37).$$

$$B_z = -krB_w \left(L + \frac{1}{8} k_w^2 r^2\right) \cos(\theta - k_w z).$$

Although a helical wiggler is in general more difficult to construct than a linear one and is not nearly as amenable to tapering, the orbital stability that it provides is a major advantage when an axial guide field is used. Also, it is possible to taper the amplitude of the wiggler field in the helical wiggler by carefully varying the winding radius as a function of z .

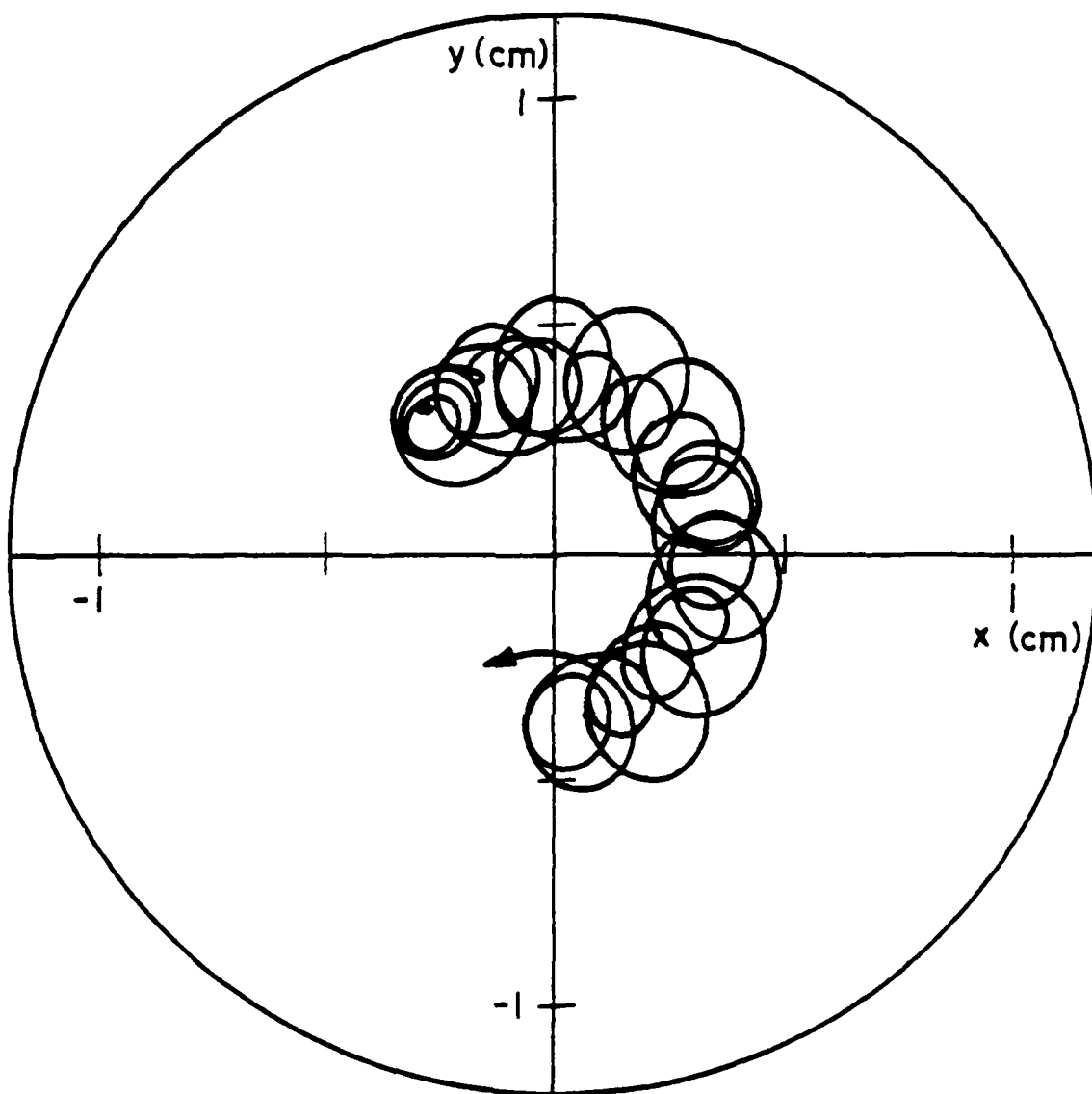


Figure 10. Electron trajectories in a helical wiggler and an axial magnetic field. Parameters are identical to those in Figure 9.

C. Diffusive Wiggler

An axially symmetric wiggler can be constructed by placing conducting rings in a pulsed solenoidal magnetic field (Jacobs et al., 1980). As the solenoidal field diffuses in, it induces eddy currents in the conducting rings which generate an opposing field. This results in a magnetic field with a periodic radial component. This process is illustrated in the computer plots of Fig. 11.

The magnetic field at a distance r from the the axis is approximately

$$\vec{B} = \hat{z} [B_0 + B_1 I_0(k_w r) \sin(k_w z)] - r B_1 I_1(k_w r) \cos(k_w z) , \quad (39)$$

where I_0 and I_1 are modified Bessel functions and B_1 is the amplitude of the axial field modulation on axis.

Figure 12 is a computer plot of the axial component of the magnetic field of the diffusive wiggler used in the system. When the wiggler is not present, the solenoidal field is 2 kG. Hence, the wiggler not only modulates the solenoidal field, it reduces the average value. To make a smooth transition into the wiggler field, the conducting rings extend all the way to the end of the solenoid where the field drops to one half the peak value.

Since the diffusive wiggler is axially symmetric, it does not produce the kind of radial particle drift which is characteristic of linear wigglers in an

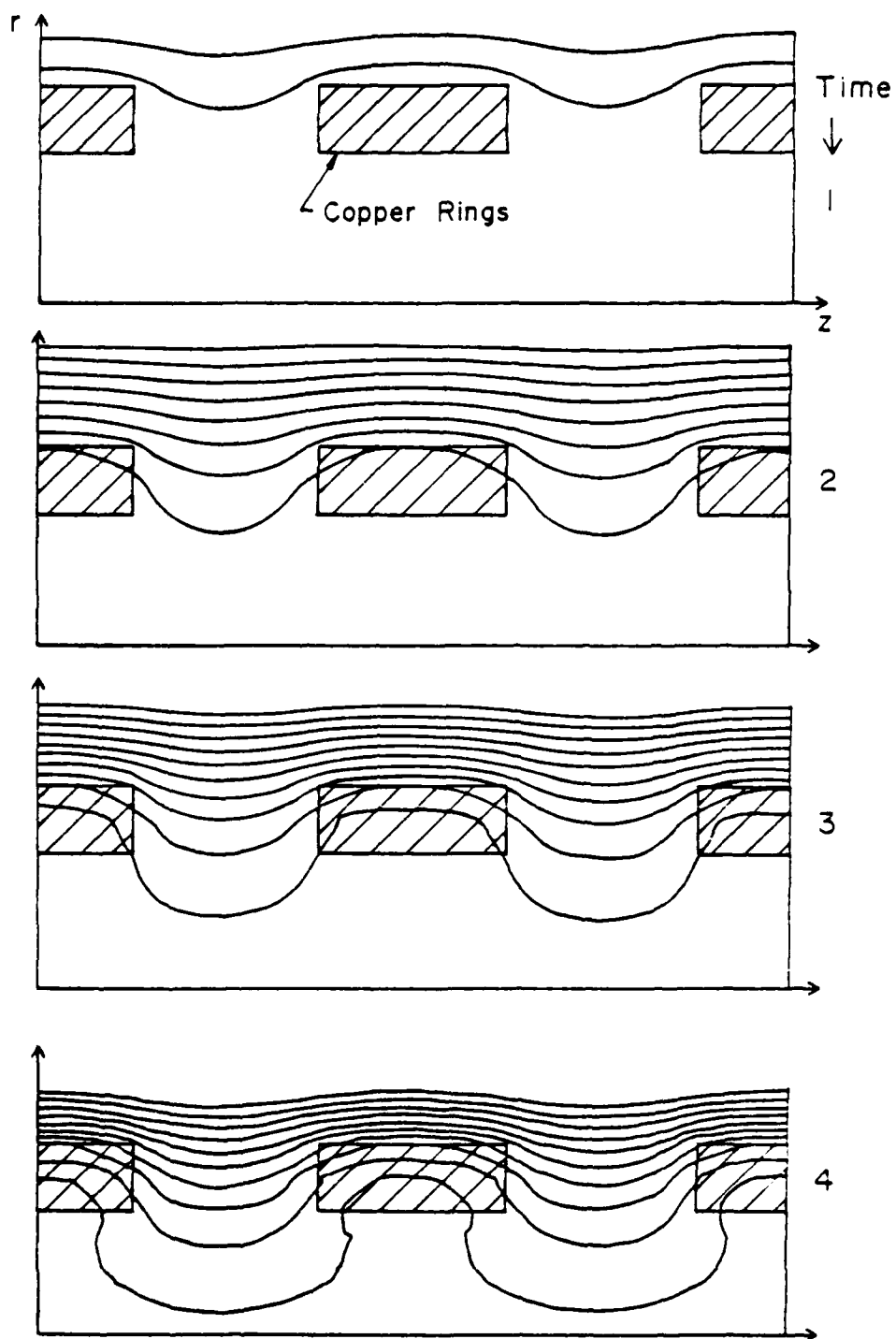


Figure 11. Diffusion of magnetic field through copper rings used in diffusive wiggler. Plots show field lines at progressively later times.

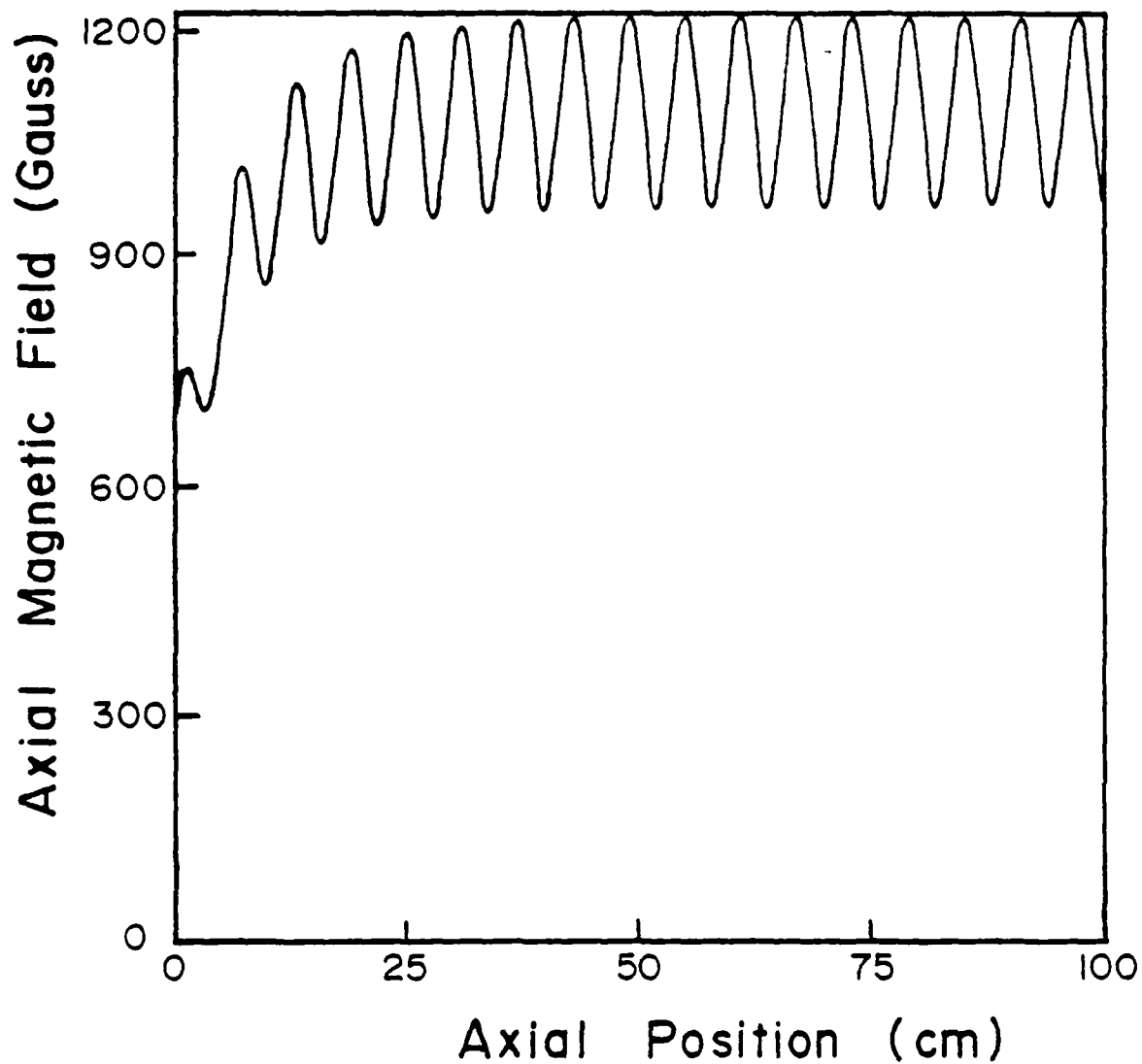


Figure 12. Plot of $B_z(r=0)$ vs. z in the diffusive wiggler. Face of solenoid is at $z = 0$.

axial field. However, the perpendicular component of the wiggler vanishes along the axis of the diffusive wiggler, so that only electrons that are significantly off axis can participate in the type of FEL interaction described previously. It has been pointed out, however, that an interaction that relies on the transverse energy in the beam can be exploited to obtain radiation from such a wiggler. This device has been called the Lowbitron (McMullin and Bekefi, 1981). The radiation frequency is approximately

$$\omega \approx (1 + \beta_z^2) \gamma_z^2 (\nu_z k_w + \Omega_0 / \gamma). \quad (39)$$

This radiation is a result of electrons interacting with the axial component of the wiggler field. The Lowbitron interaction requires $k_w c \beta_z \gamma / \Omega_0 \lesssim 1$. The electron gyroradius must be sufficiently small that the transverse field modulation felt by the electron can be neglected compared with the longitudinal modulation.

VII. Radiation Measurements

We have carried out a series of measurements on the radiation using a diffusive wiggler. Radiation measurements have primarily consisted of a) spectral analysis using cylindrical cut-off filters and/or a gas breakdown spectrometer and b) approximate power measurements using either pressure thresholds for gas breakdown or calibrated crystal detectors and attenuators. Careful consideration has been given to the identification of the interaction modes, both cyclotron and FEL, and scaling measurements have been performed to verify these modes.

A. Gas Breakdown Spectrometer

The radiated power can be estimated from the pressure at which gas breakdown occurs. An empirical formula for the rms breakdown electric field E_b is

$$E_b = AP[1 + (a/P\lambda)^2]^{1/2}, \quad (40)$$

where $A = 3000 \text{ Vm}^{-1}\text{Torr}^{-1}$ and $a = 0.9 \text{ Torr-m}$ for air or nitrogen, P is the gas pressure in Torr, and λ is the wavelength in meters. Equation (40) has been checked against McDonald's gas breakdown data (McDonald, 1966) and agrees in the worst case to within 30%. This formula is valid on the high pressure side of the breakdown curve and for $\lambda < 30 \text{ cm}$, pulse lengths $> 1 \text{ us}$, low repetition rate ($< 100 \text{ pps}$), and electron diffusion lengths small compared to the chamber dimensions.

If the radiation is reflected from a boundary, a standing wave is set up with an amplitude given by

$$E^2 = E_i^2 (1 + \Gamma^2 - 2\Gamma \cos [2 \vec{k} \cdot \vec{x}]) \quad (41)$$

where E_i is the magnitude of the incident wave, Γ the reflection coefficient, and k the wavenumber. The distance d between the peaks in the standing wave is determined by setting $2 \vec{k} \cdot \vec{x} = 2\pi$, so that

$$d = \frac{\lambda}{2 \cos \theta} \quad (42)$$

where λ is the wavelength of the radiation and θ the angle of incidence with respect to the surface normal. By adjusting the gas pressure so that the standing wave field amplitude is slightly higher than the breakdown field, localized gas breakdown will occur at the standing wave peaks. Then λ can be determined by measuring the distance between adjacent breakdown spots, and the power can be estimated from the pressure required to initiate observable breakdown.

Figure 13 shows a schematic of the spectrometer. Radiation is collected in the horn on the left. It then travels through a high pass filter and expands through the horn on the right to a collimating or weakly focusing lens. The microwaves are reflected from a metallic boundary located inside the gas filled chamber.

Figure 14 is a time integrated photograph of the resulting interference pattern. Microwave radiation has entered from the left of the photograph where the lens is located (but cannot be seen) and is reflected off a copper plate located at the right of the photograph (outlined by a light ring). All the white spots are due to light produced when the gas breaks down. Type 57 (ASA 3000) Polaroid film was used with a Graphflex camera (f/4.5) to obtain these results. The gas density was selected so that enough light was available for photographing the spots, but was kept low enough to prevent microwave reflections from the plasma. Thus for the measured pressure (25 Torr) and wavelength (4.5 cm), the electric field is determined from Eq. 40 to be about 1 kV/cm. From the spot diameter of 2.5 cm, the power is estimated for a plane wave to be 8 kW.

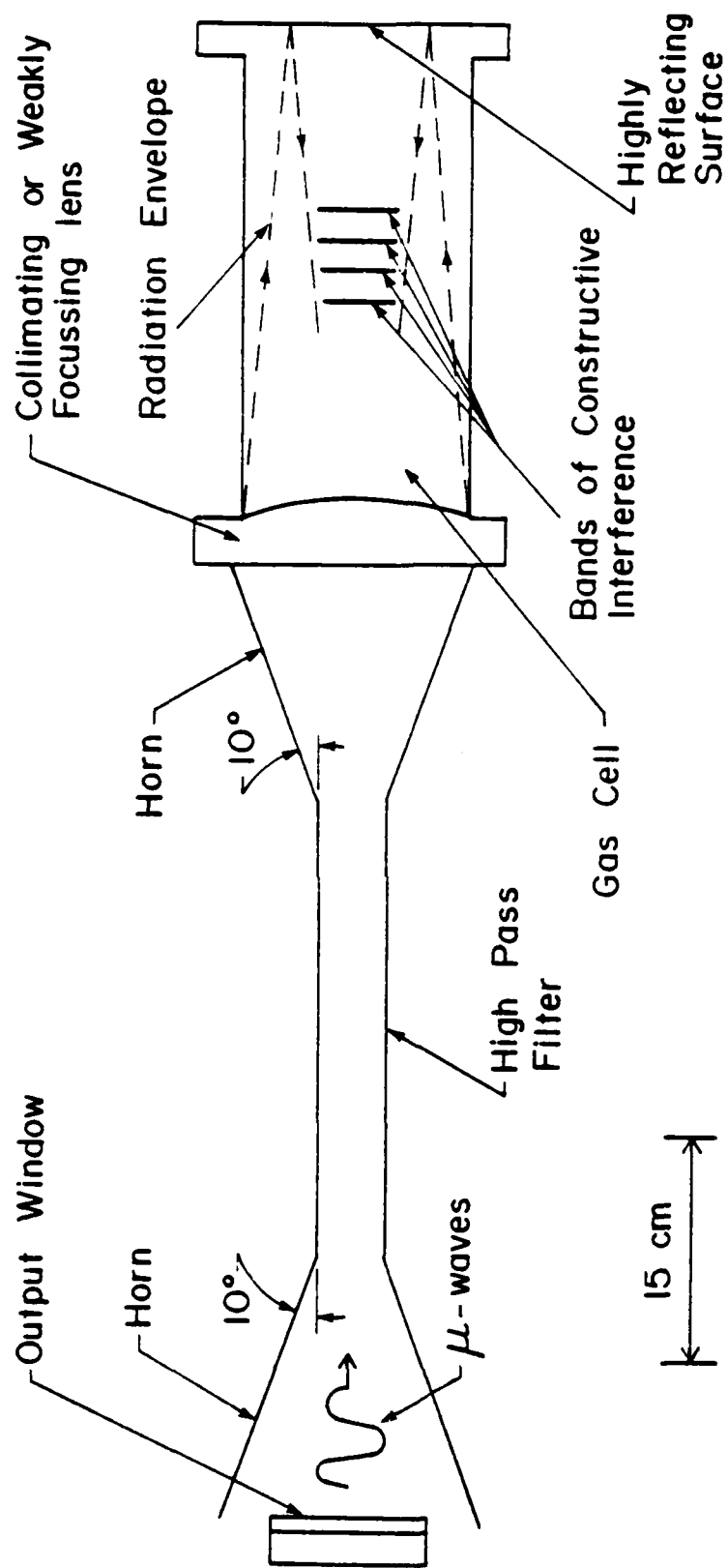


Figure 13. Schematic of gas breakdown spectrometer.

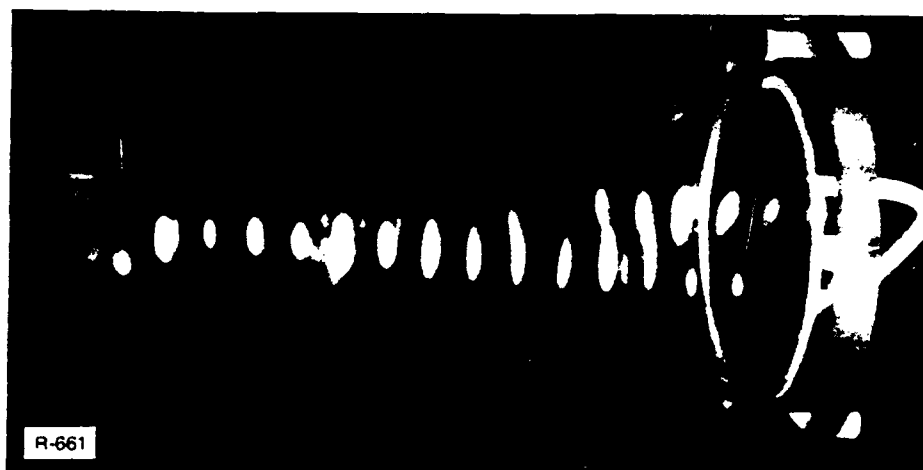


Figure 14. Open-shutter photograph of gas breakdown in 25 Torr nitrogen.
From the 2.25 cm spot spacing, the radiation wavelength is 4.5 cm.

This technique underestimates the power because there is considerable energy outside the radius of the observed spot. For example, in the case above the spot diameter is nearly a factor of 2 smaller than the wavelength, so clearly the radiation envelope is larger than the measured spot size.

We have identified this radiation as a TE_{01} mode that is excited at the 2nd harmonic of the electron cyclotron beam interaction. With similar measurements we have observed more than 100 kW of power at a wavelength of 7.5 cm. This mode was identified as a TE_{11} mode excited at the fundamental cyclotron beam interaction. The electron beam current in these experiments was 130 A, the voltage 550 keV for 2 μ sec, and the wiggler period was 6 cm. The gas breakdown spectrometer has been described in more detail elsewhere (Mako et al., 1982).

3. Mode Analysis and Experimental Results

The strongest interactions are expected when the phase velocities of the beam modes and waveguide modes are equal. The dispersion relation for the waveguide mode is

$$\omega^2 = \omega_{co}^2 + k^2 c^2 \quad (43)$$

where ω_{co} is the cutoff frequency. The dispersion relation for the free electron laser is

$$\omega = (k + k_w) v_z - \omega_p / \gamma^{3/2} \quad (44)$$

The last term is small at the current densities of this experiment and is neglected. The cyclotron mode dispersion relation is given by

$$\omega = k v_z + n \Omega_o / \gamma, \quad (45)$$

where $\Omega_o = eB_o/m$ and γ have been explicitly written to make the energy scaling clear.

Then the intersections of the FEL and cyclotron modes with a waveguide mode are found from Eqs. 43-45 to be

$$\omega_{FEL} = k_w v_z \gamma^2 \left[1 \pm \beta_z \sqrt{1 - \left(\frac{\omega_{co}}{k_w \gamma v_z} \right)^2} \right] \quad (46)$$

$$\omega_{cyc} = \frac{n \Omega_o \gamma^2}{\gamma} \left[1 \pm \beta_z \sqrt{1 - \left(\frac{\omega_{co} \gamma}{n \Omega_o \gamma_z} \right)^2} \right] \quad (47)$$

where $\omega_{co} = 2\pi c/aX_{nm}$, a is the waveguide radius and $X_{nm} = 3.41$ for TE_{11} , 2.61 for TM_{01} , 2.06 for TE_{21} , 1.14 for TM_{11} and 1.14 for TM_{02} modes.

A sketch of three dispersion relations is shown in Fig. 15. The cyclotron mode will be above the FEL mode if $n \Omega_o / \gamma > k_w v_z$. There are typically both high frequency and low frequency intersections of the FEL and cyclotron modes with the waveguide mode. However, the high frequency FEL intersection is the one which results in the usual FEL interaction. Also, the gyrotron typically operates at the low frequency cyclotron intersection, but a cyclotron

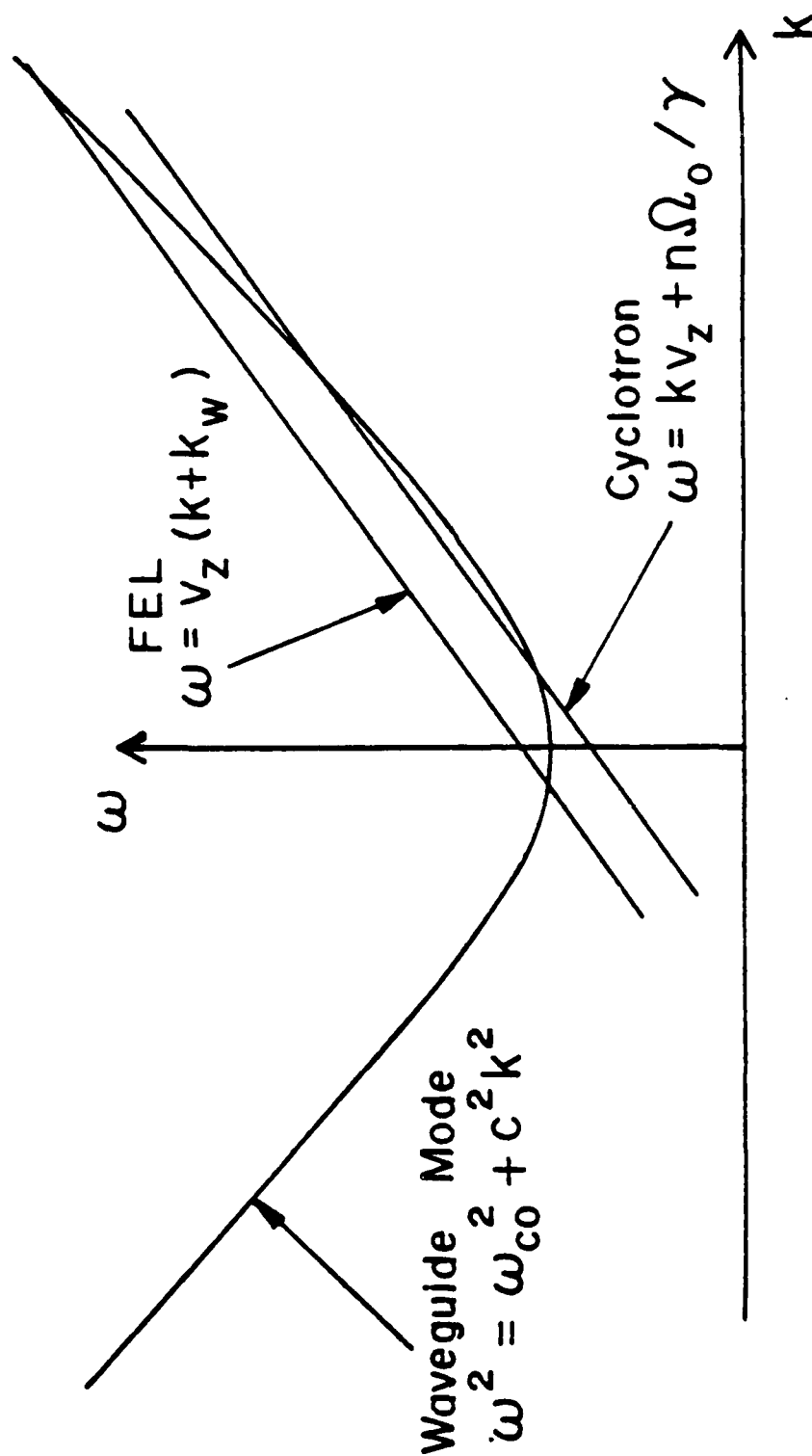


Figure 15. Dispersion curves showing a waveguide mode and the cyclotron and FEL beam lines. Radiation growth is expected at the intersection points, which are given by Eqs. 46 and 47.

interaction is also possible at the high frequency intersection. Figure 16 is a plot of the waveguide beam mode interactions that are possible for the parameters of the experiment. Both the first and second harmonics of the electron cyclotron interaction are shown, assuming $\gamma_z = 1.6$. The justification for this assumption will be given below. The arrows in the figure indicate the frequencies at which the strongest interactions were observed experimentally.

To positively identify the FEL mode at $f = 16$ GHz, we have varied the magnetic field and wiggler wavelength. It turns out that the cyclotron mode is very insensitive to B_0 in our parameter range. Because the magnetic moment is approximately conserved, the leading term for the cyclotron wave $\omega_0 \gamma_z^2$ is nearly a constant for small changes in the magnetic field. Thus, the frequencies of the electron cyclotron modes increase only slightly with increasing magnetic field. However, the FEL frequency increases with a decreasing magnetic field because γ_z^2 varies as the inverse of B_0 .

Figure 17 contains the results of the mode identification experiments. The measurements were made using high pass cutoff filters, so each bar is an indication of the resolution. This technique integrates the total power above the cut off frequency of the particular filter. Thus, the power in a particular band is just the power measured with that filter minus the power measured with the next smaller diameter filter.

The arrow is the calculated FEL frequency with $\gamma_z = 1.6$. At $\lambda_w = 7$ cm and $B_0 = 2.45$ kG the calculated frequency is 11.6 GHz and this is where we see a factor of two increase in the signal amplitude. When the magnetic field

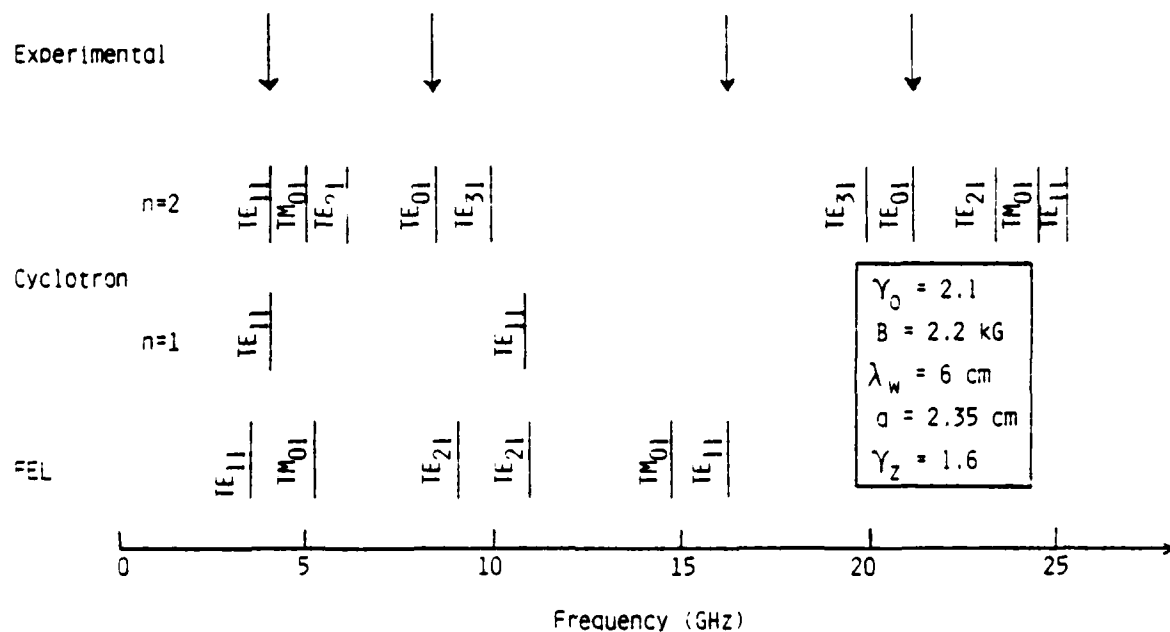


Figure 16. Beam-waveguide mode interactions which are possible with the experimental parameters. The arrows denote the measured output frequencies.

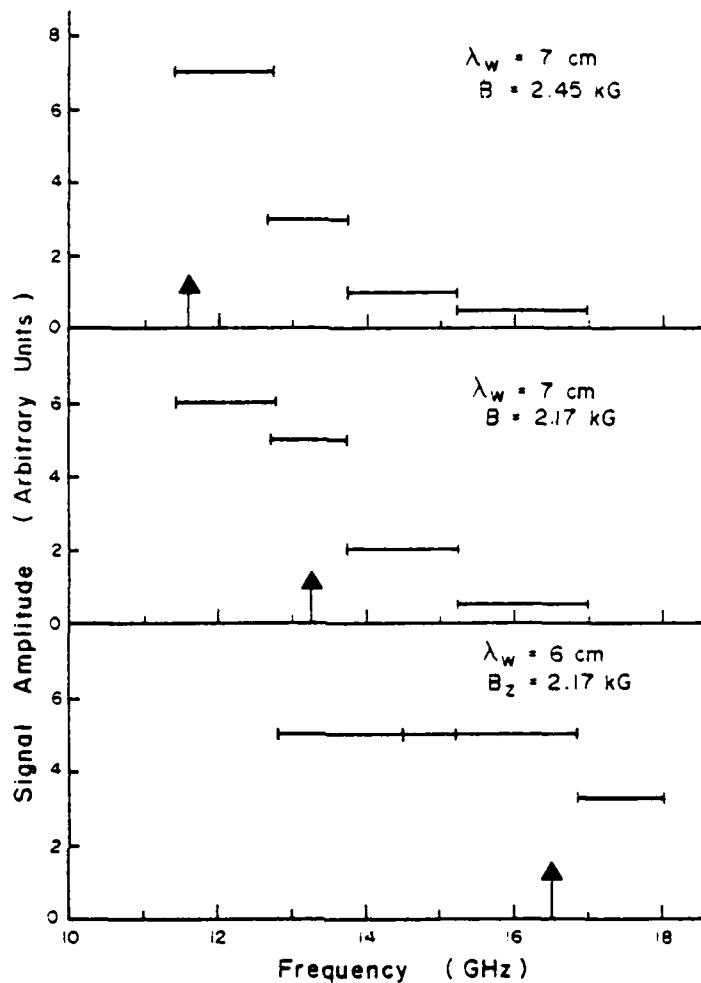


Figure 17. Frequency scaling of one particular mode with magnetic field and wiggler period, as determined by using a series of high-pass cut-off filters. Except as limited by the detector bandwidth, the signal amplitude shown in each frequency interval is proportional to the integrated power at all frequencies above the cut-off of the corresponding filter. Thus, power in a particular interval is indicated by a decrease in signal amplitude at the next higher interval. The arrows locate the theoretical frequency of the TE_{11} FEL mode, which agrees well with the observed spectra.

is reduced to 2.17 kG, the FEL frequency should increase to 13.2 GHz, and we observe a factor of two increase in that cutoff filter. At $\lambda_w = 6$ cm and $B_0 = 2.17$ kG, the FEL interaction should occur at 16.5 GHz and we observe a factor of 10 increase in that cutoff filter. We have also observed that the electron cyclotron mode at 21 GHz increases with magnetic field. We have looked for radiation from the Lowbitron interaction at $\omega = 2\gamma_z^2 (\Omega_0/\gamma + k_w v_z)$. This interaction requires perpendicular velocity and interacts with variations in the z component of the wiggler field. We did not see Lowbitron radiation that was comparable in amplitude with the FEL and 2nd harmonic cyclotron radiation.

In summary, we have observed free electron laser radiation from the long pulse induction linac. The FEL was operated in the superradiant mode. The power radiated in the FEL mode was approximately 10 kW with the beam interacting with the TE_{11} waveguide mode. Second harmonic electron cyclotron radiation of comparable amplitude was observed in the TE_{01} mode. Most of the power resulted from the low frequency cyclotron interaction. More than 100 kW of radiated power at the fundamental electron cyclotron mode was observed in the TE_{11} mode. In all cases the duration of the radiation was 2 μ sec. The thermal spread of the beam in the region requires FEL operation in the kinetic Compton regime.

The radiation spectrum is very sensitive to the average value of γ_z , which was determined by fitting the observed spectrum with interaction frequencies calculated using an assumed value of $\langle \gamma_z \rangle$. Then small variations in the magnetic and wiggler period were made to determine if the mode was an FEL or cyclotron mode. In this manner we were able to determine that $\langle \gamma_z \rangle$ had to be $1.6 \pm .2$.

Another way of estimating γ_z is by measuring the beam radius in the uniform field of the solenoid. Since the cathode in this experiment is in a magnetic field free region, the canonical angular momentum P_θ is zero. Then

$$\gamma m r v_\theta = e r A_\theta, \quad (48)$$

where A_θ is the magnetic vector potential which for a uniform magnetic field is $A_\theta = r B_z/2$. Then

$$\beta_\theta = \frac{1}{2} \frac{e B_z r}{\gamma m c}. \quad (49)$$

Experimentally, the rms beam radius was measured from time averaged x-ray scintillation pictures to be 1.3 cm when $B_z = 2.17$ kG and $\gamma = 2.1$. Thus conservation of P_θ alone gives $\beta_\perp = 0.4$ at this rms beam radius. Then

$$\gamma_z = \gamma / (1 + \beta_\perp^2 \gamma^2)^{1/2} = 1.6 \quad (50)$$

In addition, computer simulations of the induction linac free electron laser configuration have been carried out (Thompson et. al., 1982). The mean value of γ_z from the simulations was 1.61. Most of the energy spread comes at the transition between the induction linac transport system and the solenoidal field. Figure 18 is a plot of the induction linac FEL magnetic field profile. The diode is in a field free region at $z = 0$ and the last focusing coil of the linac is at 350 cm. The edge of the solenoid is at approximately 375 cm. The 2 kG magnetic field is required for a beam equilibrium radius that is consistent with a practical wiggler diameter.

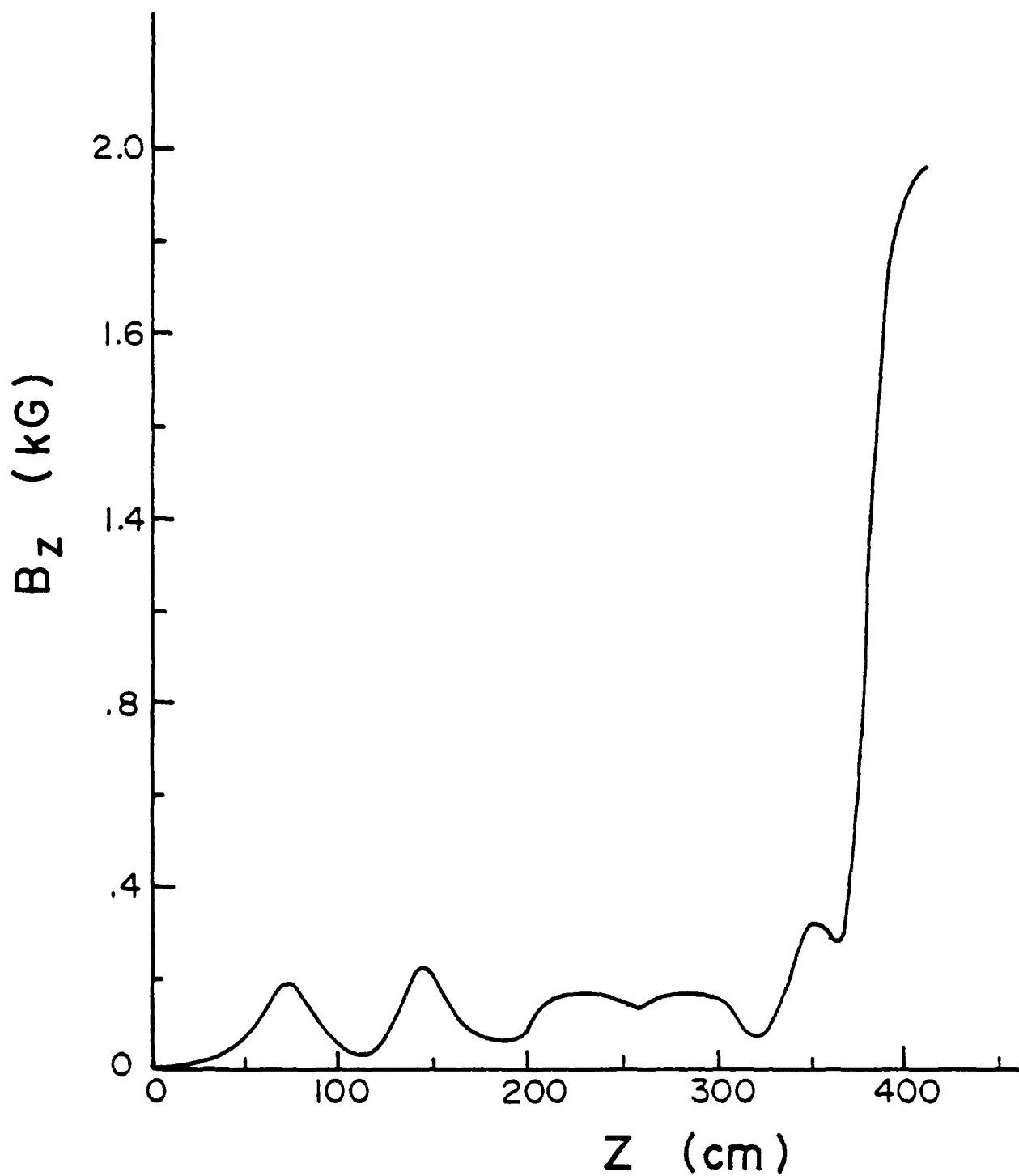


Figure 18. Axial magnetic field profile in the Long Pulse Induction Linac.

Cathode is located at $z=0$ and the FEL solenoid begins at $z = 380$ cm.

Figure 19 is a plot of results from a static computer simulation of the beam transport from the cathode into the solenoid. The last accelerating gap of the induction module is not energized, so $\gamma = 2.1$ as the beam enters the last focusing coil. When the beam has reached the uniform field region $\langle \gamma_z \rangle$ is 1.6.

This problem of beam transport and matching represents one of the major design concerns for high current free electron lasers. The equilibrium of high current beams is sensitive to self electric and magnetic fields of the beam. Abrupt changes in the wall diameter or magnetic field profile induces betatron, or zero frequency cyclotron oscillations at $\omega = 0 = k\beta c - \Omega_0/\gamma$, so the period is $\lambda = 2\pi\beta c/\Omega_0$.

A spread in β across the beam radius will cause these oscillations to phase mix after a few periods. The perturbation then appears as an effective temperature.

In the present simulation the initial normalized emittance was $\epsilon_n = 180 \pi$ mmrad-cm, whereas the effective final emittance was $\epsilon_n = \gamma r \beta_{1 \text{ rms}} = 940 \pi$ mmrad-cm. Almost all of this increase in emittance came in the transition to the solenoid. This is why the final emittance for the hot and cold cathode is about the same. These problems can and have been avoided in Marx-pulse line beam generators by immersing the diode in a very strong magnetic field. This minimizes the radial excursion and effective emittance growth. This approach becomes difficult when long pulse times are required and one must use large area hot cathodes to get kiloampere electron beams. One can conclude from this that the design of the beam transport system for an induction linac FEL is at least as important as the diode design.

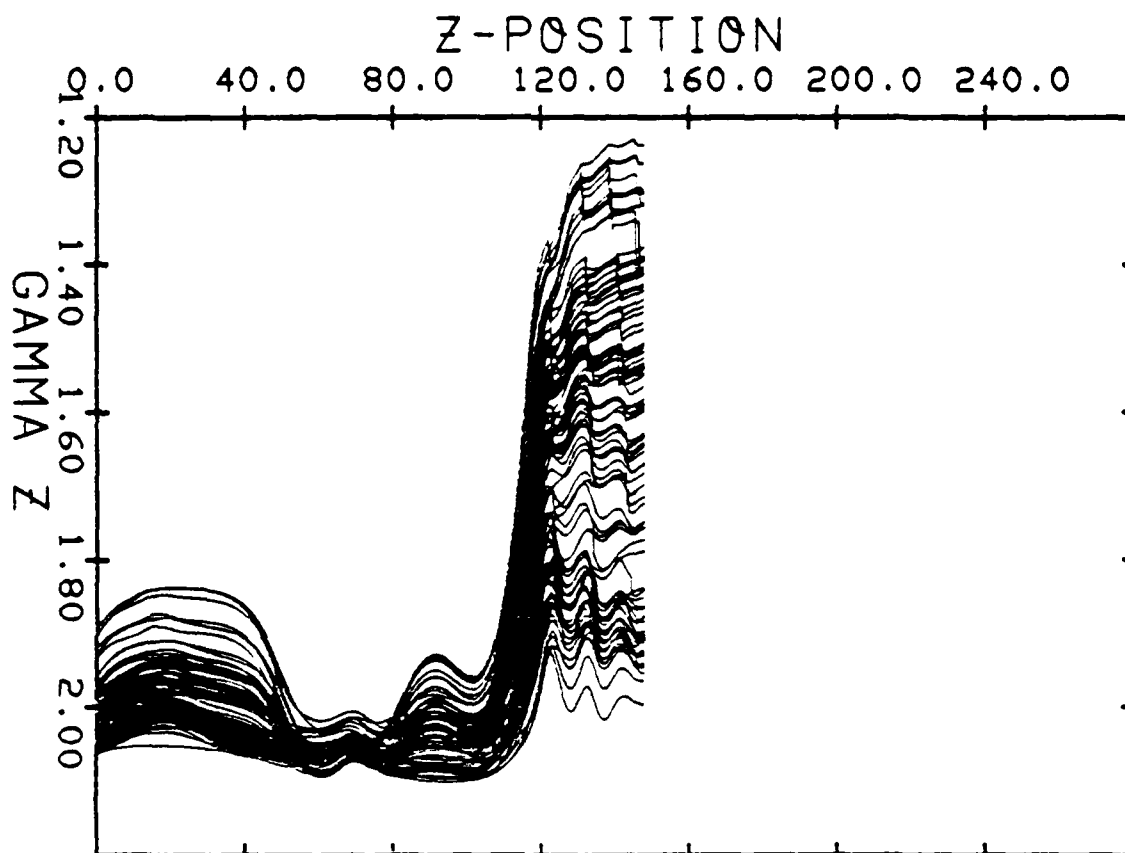


Figure 19. Variation of γ_z with z for electrons in a computer simulation of the experiment. The large spread in γ_z occurs as the beam enters the solenoidal field.

VIII. Conclusions and Future Directions

Improvements in the beam transport are clearly needed to operate in the Raman regime. One of the advantages of operating in the cold beam limit is that the efficiency of the FEL is higher and can be enhanced by tapering the wiggler period. Once the beam is trapped in the pondermotive wave, the phase velocity of the wave can be reduced gradually to extract energy from the beam. Figure 20 is a plot of efficiency vs distance for an untapered and tapered wiggler. These results are from a computer simulation of the present experiment. Whereas the intrinsic efficiency is about 5 percent, the tapered wiggler efficiency is in excess of 20 percent.

To go to shorter wavelengths the FEL can be operated as a two stage device. The output from stage one at $\lambda_1 = \lambda_w / 2\gamma^2$ can be used as the output for the second stage to give

$$\lambda_2 = \frac{\lambda_1}{4\gamma^2} = \frac{\lambda_w}{8\gamma^4} . \quad (51)$$

To obtain a high voltage high current accelerator and achieve a high gain, high power short wavelength FEL, the long pulse induction module can be converted into a racetrack accelerator (Roberson, 1981; Mondelli and Roberson, 1982). This takes advantage of the long pulse to give a voltage

$$V = V_g T / \tau \quad (52)$$

where V_g is the voltage gain of the module, T the time the module is on, and τ the time it takes the beam to go around the racetrack. In the present case a 30 nsec path length would result in a 26 MeV beam with the 2 μ s, 0.4 MV module.

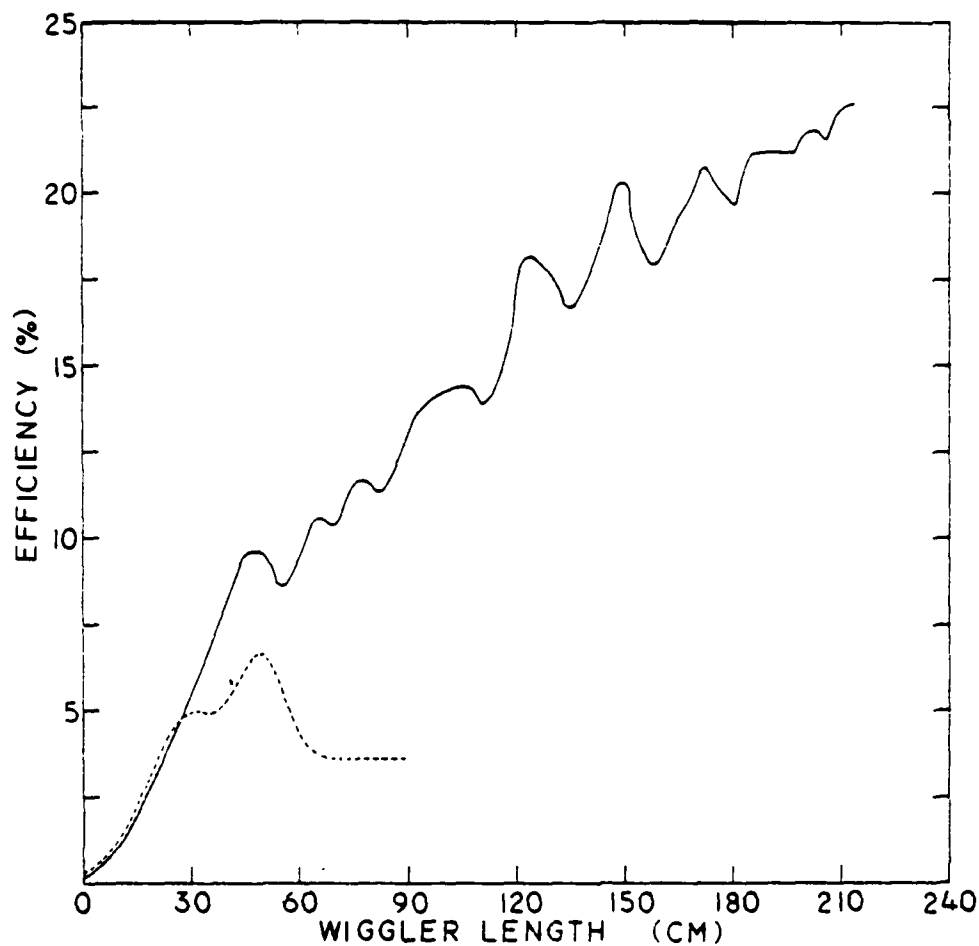


Figure 20. Theoretical FEL efficiency vs. interaction length with an without a tapered wiggler. The parameters used for the calculation are those of the experiment.

Acknowledgements

We would like to thank A. Mondelli and S. Slinker for their contributions on the diffusive wiggler and beam transport; H. Freund for discussion on the linear wiggler; C.M. Tang for simulations of the linear wiggler; J.R. Thompson and B. Moore for computer simulations of the beam transport and Mark Wilson for his help in setting up the induction linac at NRL.

References

- Barbini, R. and Vignola, G. (1982). In "Physics of Quantum Electronics" (S. Jacobs, H. Pilloff, M. Scully, G. Moore, M. Sargent III, and R. Spitzer, eds.), Vol. 8, pp. 235-262. Addison-Wesley, Reading, MA.
- Bazin, C., Billardon, M., Deacon, D.A.G., Ellaume, P., Farge, Y., Madey, J.M.J., Ortega, J.M., Petroff, Y., Robinson, K.E., and Velghe, M. (1982). In "Physics of Quantum Electronics" (S. Jacobs, H. Pilloff, M. Scully, G. Moore, M. Sargent III, and R. Spitzer, eds.), Vol. 8, pp. 89-118. Addison-Wesley, Reading, MA.
- Bizzarri, U., Ciocci, F., Dattoli, G., DeAngelis, A., Fiorentino, E., Gallerano, G.P., Marino, A., Renieri, A., and Vignati, A., (1982). In "Physics of Quantum Electronics" (S. Jacobs, H. Pilloff, M. Scully, G. Moore, M. Sargent III, and R. Spitzer, eds.), Vol. 9, pp. 677-696. Addison-Wesley, Reading, MA.
- Blewett, J.P. and Chasman, R. (1977), "Journ. of Appl. Phys." 48, 2692.
- Boehmer, H., Caponi, M.Z., Edighoffer, J., Fornaca, S., Munch, J., Neil, G.R., Saur, B., and Shih, C. (1982). Phys. Rev. Lett. 48, 141.
- Deacon, D.A.G., Elias, L.R., Madey, J.M.J., Ramian, G.J., Schwettman, H.A., and Smith, T.I. (1977). Phys. Rev. Lett. 38, 892.
- Efthimion, P.C. and Schlesinger, S.P. (1977). Phys. Rev. A. 16, 633.

Elias, L.R., Fairbanks, W.M., Madey, J.M.J., Schwettman, H.A., and Smith, T.I. (1976). Phys. Rev. Lett. 36, 717.

Elias, L.R. and Ramian, G. (1982). In "Physics of Quantum Electronics", (S. Jacobs, H. Pilloff, M. Scully, G. Moore, M. Sargent III, and R. Spitzer, eds.), Vol. 9, pp. 577-602. Addison-Wesley, Reading, MA.

Friedman, M. and Herndon, M. (1972). Phys. Rev. Lett. 28, 210.

Gaupp, A. (1982). In "Physics of Quantum Electronics", (S. Jacobs, H. Pilloff, M. Scully, G. Moore, M. Sargent III, and R. Spitzer, eds.), Vol. 9, pp. 263-274. Addison-Wesley, Reading, MA.

Gilgenbach, R.M., Marshall, T.C., and Schlesinger, S.P. (1979) Phys. Fluids 22 971-977.

Granatstein, V.L., Herndon, M., Parker, R.K., and Schlesinger, S.P. (1974). IEEE Trans. Microwave Theory Tech. 22, 1000.

Granatstein, V.L., Schlesinger, S.P., Herndon, M., Parker, R.K., and Pasour, J.A. (1977). Appl. Phys. Lett. 30, 384.

Granatstein, V.L., ed. (1981). "Special Issue on Gyrotrons." Int. J. Electronics 51, 275-606.

Grossman, A., Marshall, T.C., and Schlesinger, S.P. (1983) Phys. Fluids 26,

Hasegawa, A. (1978) Bell Syst. Tech. J. 57, 3069.

Jacobs, K.D., Shefer, R.E., and Bekefi, G. (1980). Appl. Phys. Lett. 37, 583.

Kroll, N.A. and McMullin, W.A. (1978). Phys. Rev. A 17, 300-308.

Kulke, B., Ravenscroft, D.S., and Vogtlin, G.E. (1982), IEEE Trans. Nucl. Sci. NS-28, 2882.

Leiss, J.E., Norris, N.J. and Wilson, M.A., (1980), Particle Accelerators 10, 223.

Luccio, A. (1982). In "Physics of Quantum Electronics" (S. Jacobs, H. Pilloff, M. Scully, G. Moore, M. Sargent III, and R. Spitzer, eds.), Vol. 8, pp. 153-190. Addison-Wesley, Reading, MA.

Mako, F., Pasour, J.A., Roberson, C.W., and Lucey, R. (1982). NRL Memo Report #4945.

Marshall, T.C., Talmadge, S., and Efthimion, P. (1977a). Appl. Phys. Lett. 31, 302.

Marshall, T.C., Sandel, F.L., and Gilgenbach, R.M., (1977b). Proc. Sec. Int. Topical Conf. on High Power Electron and Ion Beam Res. Technol., pp. 697-702.

McDermott, D.B., Marshall, T.C., Schlesinger, S.P., Parker, R.K., and Granatstein, V.L. (1978). Phys. Rev. Lett. 41, 1368-1371.

McDonald, A.D., (1966) "Microwave Breakdown in Gases", John Wiley & Sons.

Mondelli, A. and Roberson, C.W. "Energy Scaling Laws for the Racetrack Induction Accelerator", NRL Memo Report

Mross, M.R., Marshall, T.C., Efthimion, P., and Schlesinger, S.P. (1976).

Digest Sec. Int. Conf. Winter School on Submillimeter Waves and Appl. (IEEE Cat. No. 76 CH 1152-8 MTT), pp. 128-129.

Nation, J.A. (1970). Appl. Phys. Lett. 17, 491.

Neil, V.K. (1979). Jason Technical Report JSR-79-10, SRI International, Arlington, VA.

Parker, R.K., Jackson, R.H., Gold, S.H., Freund, H.P., Granatstein, V.L., Efthimion, P.C., Herndon, M. and Kinkead, A.K. (1982) Phys. Rev. Lett. 48, 238.

Pasour, J.A., Roberson, C.W., and Mako, F. (1982) J. Appl. Phys. 53,

Phillips, R.M. (1960). IRE Trans. on Electron Dev. 7, 231.

Prohaska, R., and Fisher, A. (1982). Rev. Sci. Instrum. 53, 1092.

Prosnitz, D. and Sessler, A.M. (1982). In "Physics of Quantum Electronics" (S. Jacobs, H. Pilloff, M. Scully, G. Moore, M. Sargent III, and R. Spitzer, eds.), Vol. 9, pp. 651-670, Addison-Wesley, Reading, MA.

Ramirez, J.J. and Cook, D.L. (1980). J. Appl. Phys. 51, 4602.

Roberson, C.W. (1981), IEEE Trans. Nucl. Sci. NS-28, 3433.

Roberson, C.W., Pasour, J.A., Kapetanacos, C.A., Sprangle, P., Golden, J., Mako, F., and Lucey, R. (1982). In "Physics of Quantum Electronics" (S. Jacobs, H. Pilloff, M. Scully, G. Moore, M. Sargent III, and R. Spitzer, eds.), Vol. 9, pp. 727-740. Addison-Wesley, Reading, MA.

Shaw, E.D. and Patel, C.K.N. (1982). In "Physics of Quantum Electronics" (S. Jacobs, H. Pilloff, M. Scully, G. Moore, M. Sargent III, and R. Spitzer, eds.), Vol. 9, pp. 671-676. Addison-Wesley, Reading, MA.

Shefer, R.E. and Bekefi, G. (1982). In "Physics of Quantum Electronics" (S. Jacobs, H. Pilloff, M. Scully, G. Moore, M. Sargent III, and R. Spitzer, eds.), Vol. 9., pp. 703-726. Addison-Wesley, Reading, MA.

Sloan, M.L. and Davis, H.A. "Design and Testing of Low Temperature Intense Electron Beam Diodes" Accepted for publication in Physics of Fluids.

Sprangle, P., Smith, R.A., and Granatstein, V.L., (1979). In "Infrared and Millimeter Waves" (K.J. Button, ed.) Vol. 1, pp. 279-327. Academic Press, New York.

Sprangle, P. and Manheimer, W.M. (1975). Phys. of Fluids 18, 224.

Sprangle, P., Granatstein, V.L., and Baker, L. (1975). Phys. Rev. A 12, 1697.

Thompson, J.R. Moore, B.N., Sloan, M.L. and Uglum, J.R. (1982). Bull. Am. Phys. Soc. 27, 1011.

Warren, R.W., Brau, C.A., Newnam, B.E., Stein, W.E., Winston, J.G., and Young, L.M. (1982). In "Physics of Quantum Electrons" (S. Jacobs, H. Pilloff, M. Scully, G. Moore, M. Sargent III, and R. Spitzer, eds.), Vol. 8, pp. 397-414. Addison-Wesley, Reading, MA.

Page 69-73 Not Missing
Document Misnumbered

Special Focus Program Advanced Accelerator
Modified Betatron Design Review
Coil Design

Presented by: F. Mako
Contributors: J. Golden, J. Pasour and K. Smith

December 7, 1982

SPECIAL FOCUS PROGRAM
ADVANCED ACCELERATOR

MODIFIED BETATRON DESIGN
REVIEW

COIL DESIGN

DECEMBER 7, 1982

PRESENTED BY:

F. MAKO

CONTRIBUTORS:

J. GOLDEN

J. PASOUR

K. SMITH

OUTLINE

- VF AND TF COIL DESIGN OBJECTIVES
- COIL CROSS-SECTION AND MATERIAL SELECTION
- BUS EDDY CURRENT ERRORS, CROSS-SECTION AND MATERIAL SELECTION
- COIL AND BUS CONFIGURATION
- NON COAXIAL BUS ERRORS
- ELECTRICAL SPECIFICATIONS
- SUMMARY AND CONCLUSIONS

VF AND TF COIL DESIGN OBJECTIVES

- 1) MAINTAIN FIELD UNIFORMITY AND LOW FIELD ERRORS $\left(\frac{\Delta B}{B} \lesssim .5\%\right)$
- 2) MINIMIZE ENERGY LOSSES $(\lesssim 10\%)$
- 3) MINIMIZE DEFLECTIONS $(\lesssim 1\text{mm})$
- 4) ESTABLISH A RELIABLE AND ACCESSIBLE SYSTEM

LIST OF SYMBOLS

r_v : RADIUS OF VERTICAL BUS CONDUCTOR

l_v : LENGTH OF VERTICAL BUS CONDUCTOR

z : AXIAL POSITION OF THE BOTTOM OF THE BUS

B_{BUS} : IS THE VF (AVERAGE) IN THE REGION WHERE THE BUS
IS GOING TO BE LOCATED

b : SIDE LENGTH OF SQUARE CROSS SECTION COIL

σ : ELECTRICAL CONDUCTIVITY

τ : TIME TO REACH PEAK CURRENT

S : TOTAL CONDUCTOR LENGTH

L : COIL OR CONDUCTOR INDUCTANCE

E_{LOSS}/E_{COIL} : FRACTIONAL ENERGY LOSS (MAGNETIC AND
RESISTIVE UNLESS SPECIFIED OTHERWISE)

F : FORCE PER UNIT LENGTH

LIST OF SYMBOLS, CON'T.

d : LENGTH OF COIL BETWEEN FIXED POINTS (SPAN)

α : DEFLECTION DISTANCE

Y : YOUNG'S MODULUS OF ELASTICITY

τ_{DF} : DIFFUSION TIME THROUGH A THIN WALL CYLINDER

t : WALL THICKNESS OF COAXIAL BUS,

μ_0 : PERMEABILITY OF FREE SPACE

R_T : TOTAL AC COIL, BUS AND JOINT RESISTANCE

L_T : TOTAL COIL AND BUS INDUCTANCE

L_{BUS} : BUS INDUCTANCE

L_{COIL} : COIL INDUCTANCE

E_{COIL} : MAGNETIC FIELD ENERGY FROM COILS ONLY

C : CAPACITANCE

VF COIL-SELECTION

CONSIDER A SQUARE CROSS SECTION COIL WITH SIDE OF LENGTH, b ,

- CLEARANCE REQUIRES: $b \lesssim 7 \text{ cm}$,
- LOW ENERGY LOSS REQUIRES THE CONDUCTIVITY, $\sigma \gtrsim \frac{\tau_s}{Lb^2} \left(\frac{E_{\text{COIL}}}{E_{\text{LOSS}}} \right)$,
- SMALL DEFLECTION (α) REQUIRES THE MODULUS, $Y \gtrsim \frac{F}{32\alpha} \left(\frac{d}{b} \right)^4$,

FOR $\tau = 3.2 \text{ ms}$, $S = 170 \text{ m}$, $L = 590 \text{ } \mu\text{H}$, $E_{\text{LOSS}}/E_{\text{COIL}} = .1$

(RESISTIVE ONLY), $d = 70 \text{ cm}$, $\alpha = .1 \text{ cm}$, $F = 10^7 \text{ dynes/cm}$

(HOOP STRESS) AND $b = 5 \text{ cm}$ THEN

$$\underline{\sigma \gtrsim 4 \times 10^6 (\Omega\text{-m})^{-1}}, \quad \underline{Y \gtrsim 10^{11} \text{ dynes/cm}^2}$$

\Rightarrow ALUMINUM OR COPPER CAN SATISFY THESE REQUIREMENTS.

ALUMINUM IS SELECTED WHEN COST AND WEIGHT ARE CONSIDERED.

TF COIL - SELECTION

CONSIDER A SQUARE CROSS SECTION COIL WITH SIDES OF
LENGTH, b ,

- CLEARANCE REQUIRES: $b \leq 20$ CM,
- LOW ENERGY LOSS REQUIRES THE CONDUCTIVITY,

$$\sigma \geq \frac{\tau s}{L b^2} \left(\frac{E_{\text{COIL}}}{E_{\text{LOSS}}} \right),$$

- SMALL DEFLECTION (α) REQUIRES THE MODULUS: $\gamma \geq \frac{F}{32\alpha} \left(\frac{d}{b} \right)^4,$

FOR $\tau = 3.6$ MS, $s = 120$ M, $L = 85 \mu\text{H}$, $E_{\text{LOSS}}/E_{\text{COIL}} = .1$

(RESISTIVE), $d = 150$ CM, $\alpha = .1$ CM, $F = 10^8$ DYNES/CM (HOOP STRESS)

AND $b = 10$ CM THEN

$$\sigma \geq 5 \times 10^6 (\Omega\text{-M})^{-1}, \quad \gamma \geq 1.6 \times 10^{12} \text{ DYNES/CM}^2$$

⇒ ALUMINUM OR COPPER CAN SATISFY THE CONDUCTIVITY REQUIREMENT BUT,

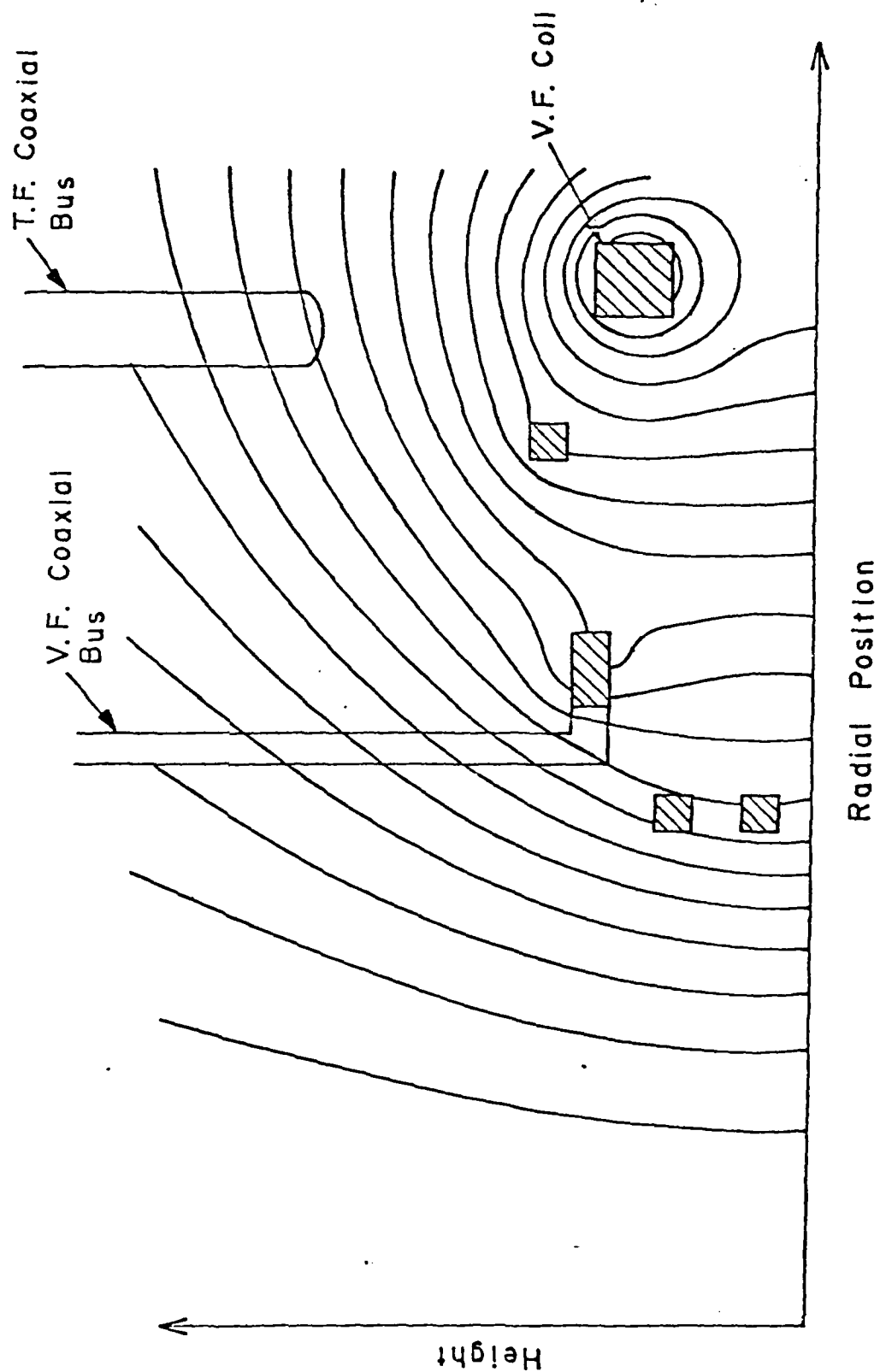
THE MODULUS REQUIRES STAINLESS STEEL OR EQUIV.

⇒ THE SPAN (d) IS REDUCED BY THE DECK SUPPORT THUS COPPER OR

ALUMINUM CAN BE USED. ALUMINUM IS SELECTED AFTER WEIGHT

AND COST ARE CONSIDERED

Bus Location In Vertical Field



FIELD ERRORS FROM BUS EDDY CURRENTS INDUCED BY VF

FOR NO DIFFUSION THROUGH A VERTICAL BUS, THE VF ERROR ~~IS~~

IS GIVEN UNDER THE BUS ON THE MIDPLANE BY

$$\Delta B_z = B_{bus} \frac{r_v^2}{4} \left[\frac{1}{z^2} - \frac{1}{(\ell_v + z)^2} \right]$$

FOR $r_v = 5\text{cm}$, $\ell_v = 100\text{cm}$ AND LOCATED AT $r = 90\text{cm}$,

$z = 33\text{cm}$ THEN $B_{bus} = 1.7 B_z$ AND AT $r = 90\text{cm}$, $z = 0$

$$\Delta B_z / B_z \approx 1\% \quad (\text{WORST CASE, INNER VF BUS})$$

\Rightarrow THE INNER VF BUS MUST BE MADE MAGNETICALLY TRANSPARENT

AND/OR HAVE A SMALL MAGNETIC MOMENT.

\Rightarrow THE TF BUS CAN BE LOCATED IN A REGION OF LOW VF.

\Rightarrow BUS CONDUCTORS ABOVE AND BELOW THE DECK GIVE SMALL

($< .1\%$) VF ERRORS.

VF AND TF BUS SELECTION

CONSIDER COAXIAL BUS WITH OUTER RADIUS A

VF Bus

- COIL COMPATIBLE AND CLEARANCE REQUIRE: $A \lesssim 5 \text{ CM}$
- MAGNETIC DIFFUSION REQUIRES: $\sigma \leq \frac{2\tau_{DF}}{AtH_0}$

TF Bus

- COIL COMPATIBLE AND CLEARANCE REQUIRES: $A \lesssim 10 \text{ CM}$
- LOW LOSS REQUIRES: $\sigma \geq \frac{\tau_s}{L2\pi At} \left(\frac{E_{COIL}}{E_{LOSS}} \right)$

VF, $\tau_{DF} = .5 \text{ MS}$, $A = 2.5 \text{ CM}$, $t = 1 \text{ CM}$

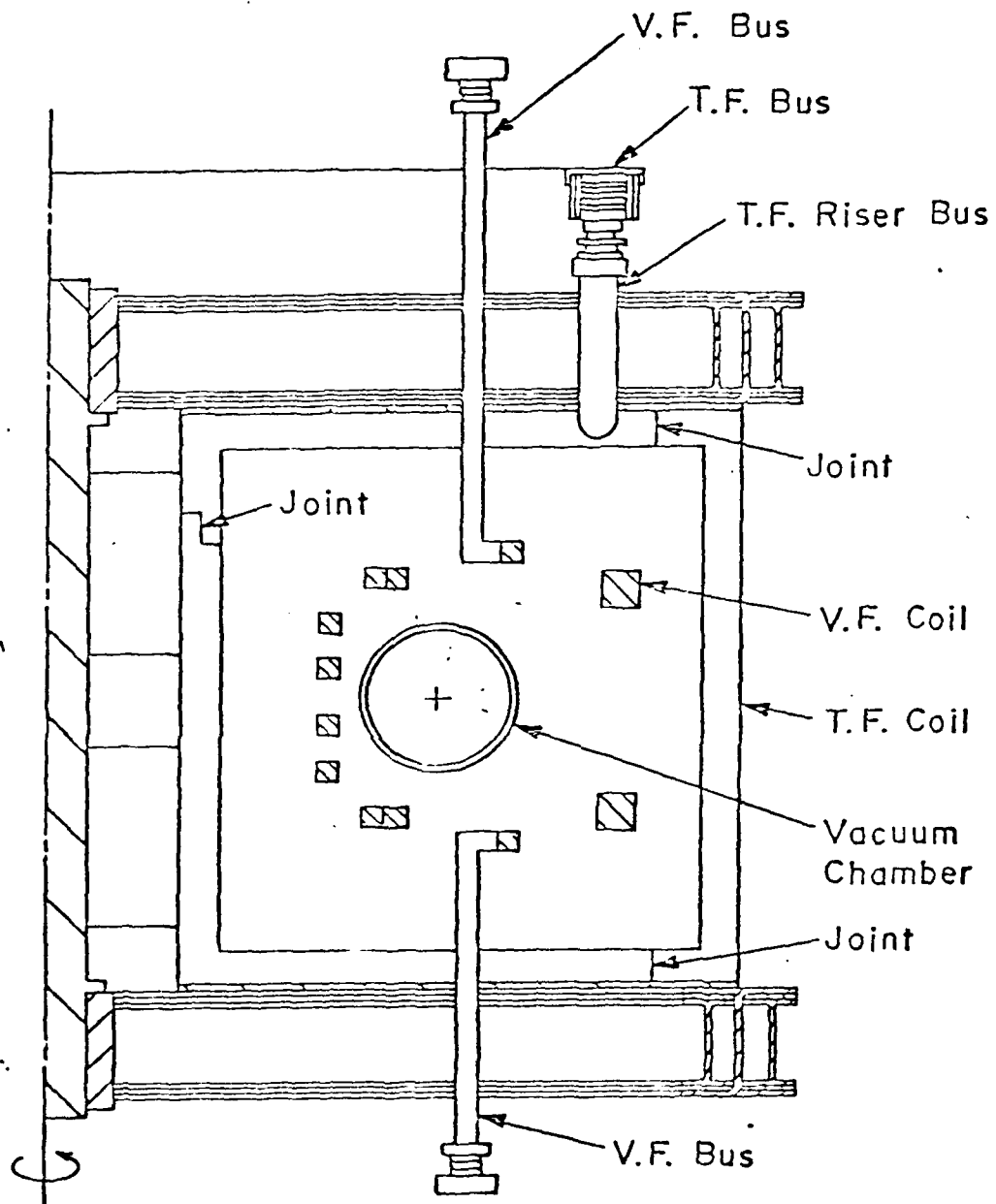
$$\underline{\sigma \leq 3 \times 10^6 (\Omega\text{-M})^{-1}}$$

STAINLESS STEEL OR EQUIV. IS REQUIRED.

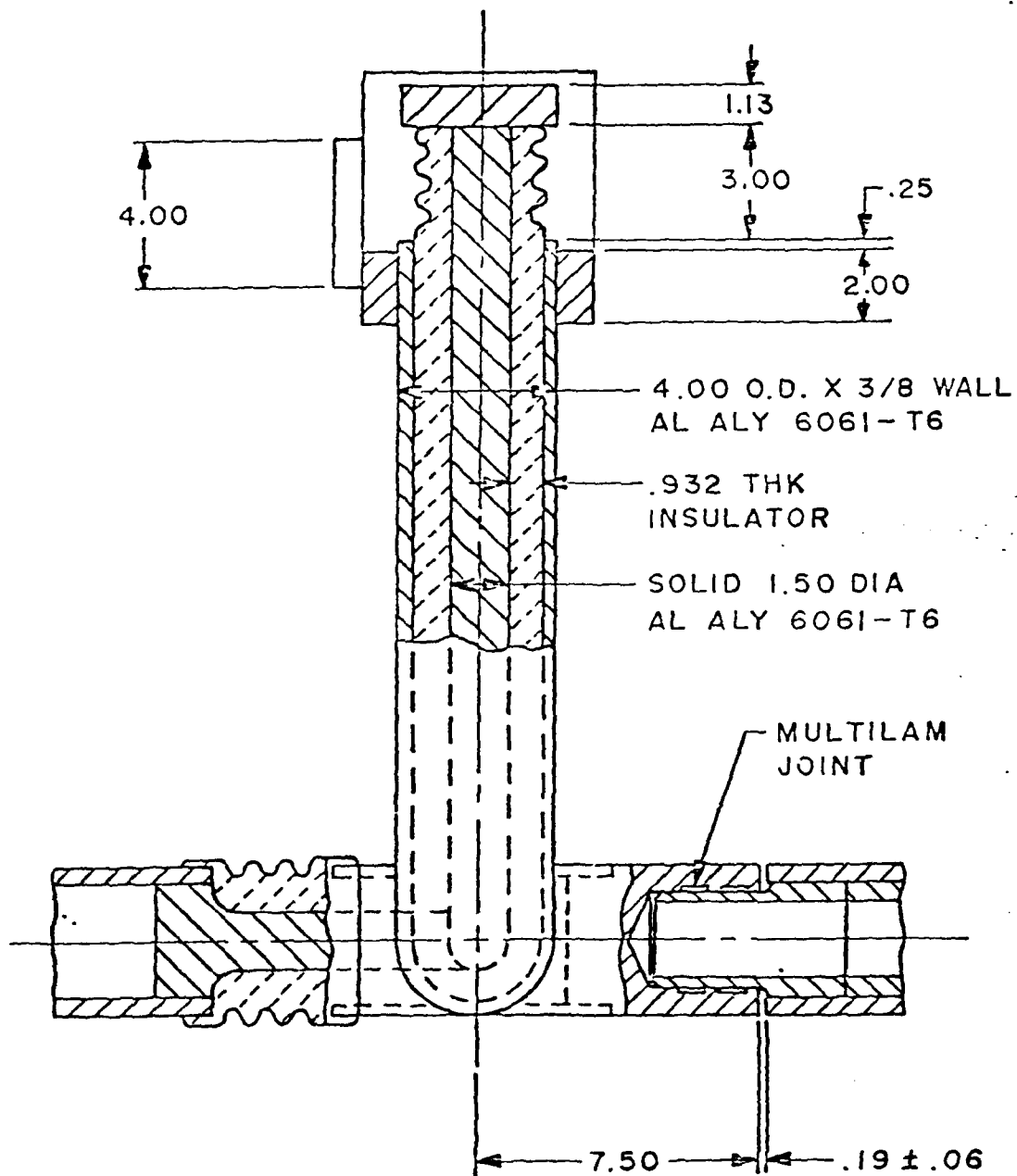
TF, $\tau = 3.6 \text{ MS}$, $s = 24 \text{ M}$, $L = 3 \mu\text{H}$, $\Delta = 1 \text{ CM}$, $A = 5 \text{ CM}$,

$$\underline{\sigma \geq 9 \times 10^6 (\Omega\text{-M})^{-1}}$$

ALUMINUM OR COPPER WILL WORK.



Coils and Bus

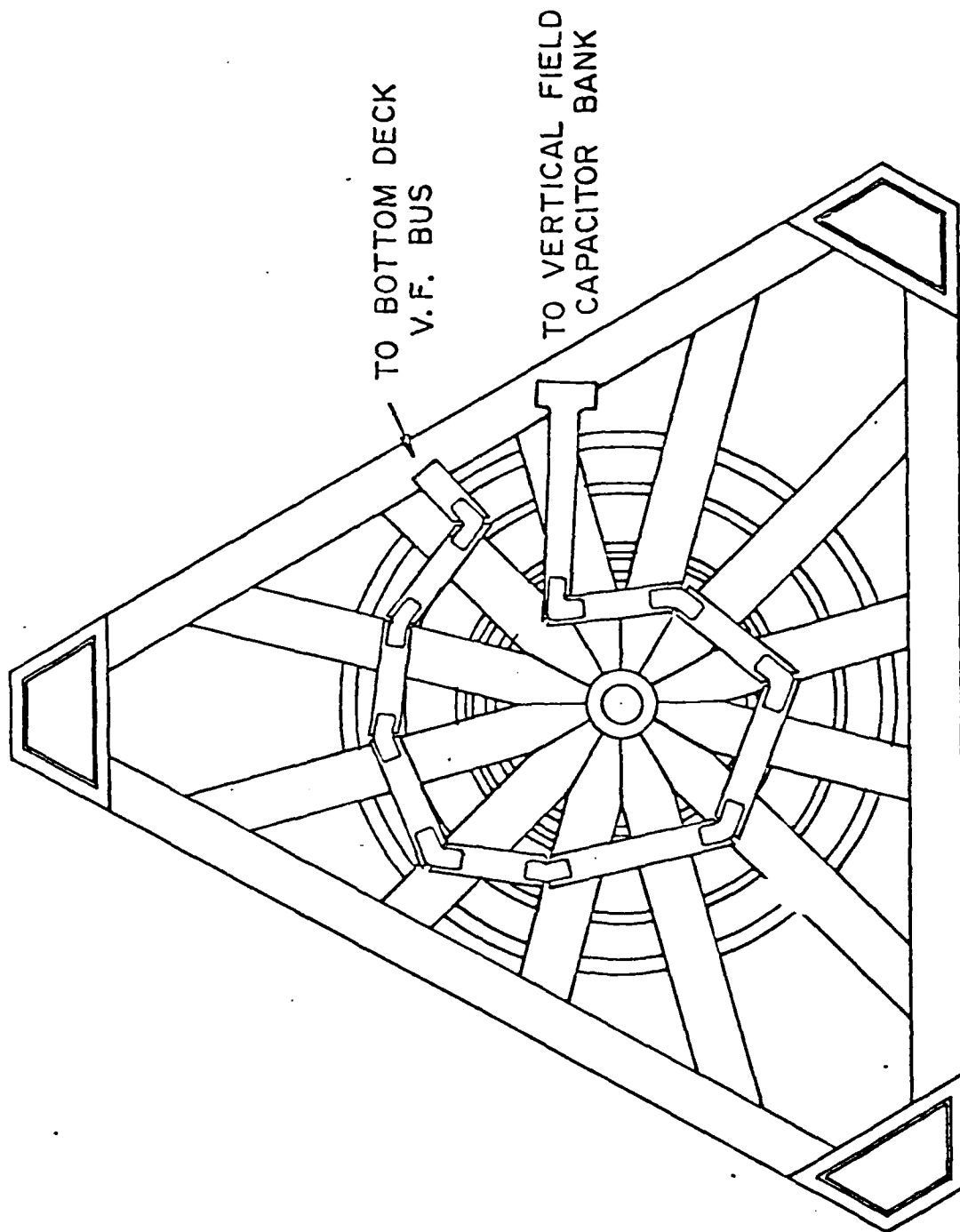


T.F. COAXIAL BUS TO COIL

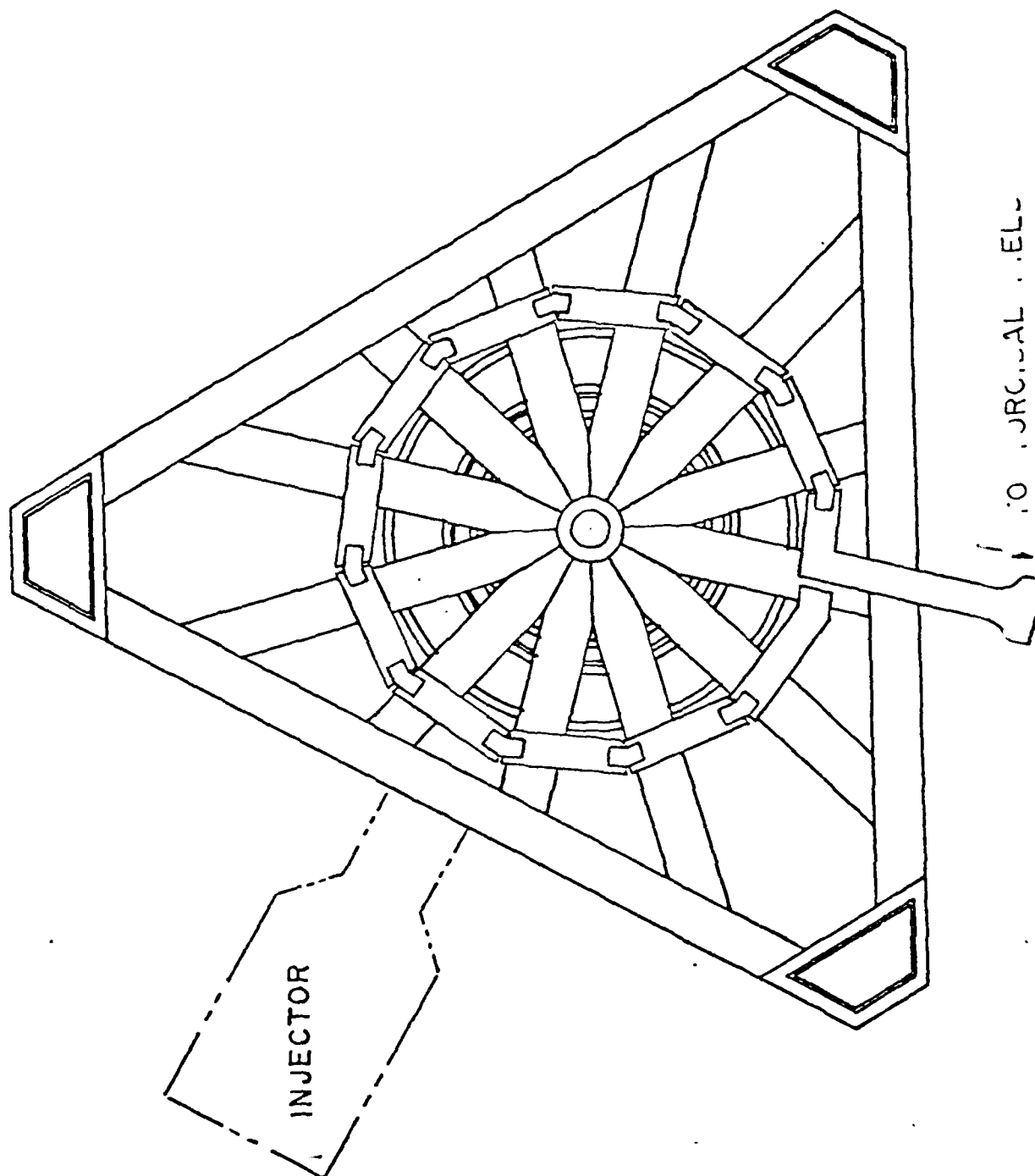
SOLUTION TO JOINT PROBLEM

- MULTILAM-A LOUVERED INTERFACE THAT PROVIDES MANY POINTS OF CONTACT
- JOINTS ARE DEMOUNTABLE AND DON'T REQUIRE PLASTIC DEFORMATION OF JOINT CONDUCTORS
- LOW RESISTANCE ($\sim 4\mu\Omega$ /JOINT WITH 210 LOUVERS FOR TF) AND HIGH CURRENT (> 210 kA FOR TF, 1 kA/LOUVER TESTED > 1 SEC) JOINTS ARE POSSIBLE

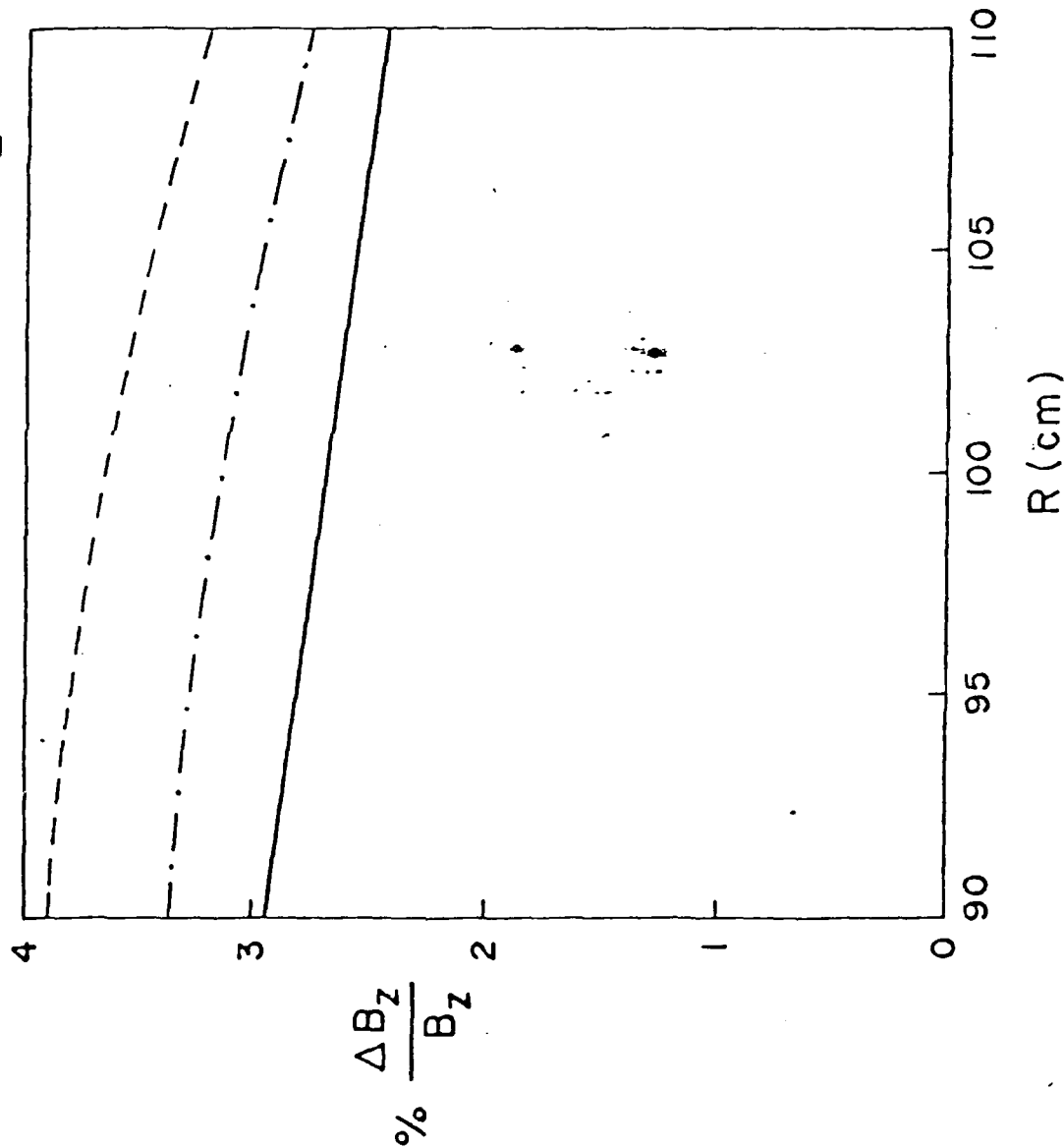
COIL TO COIL V.F. BUS



COIL TO COIL T.F. BUS

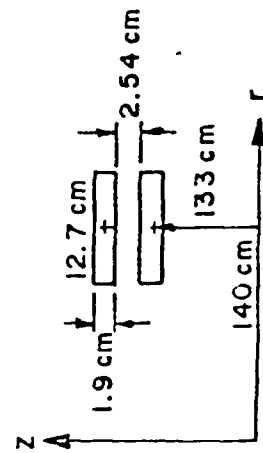


T.F. BUS ERROR IN B_z



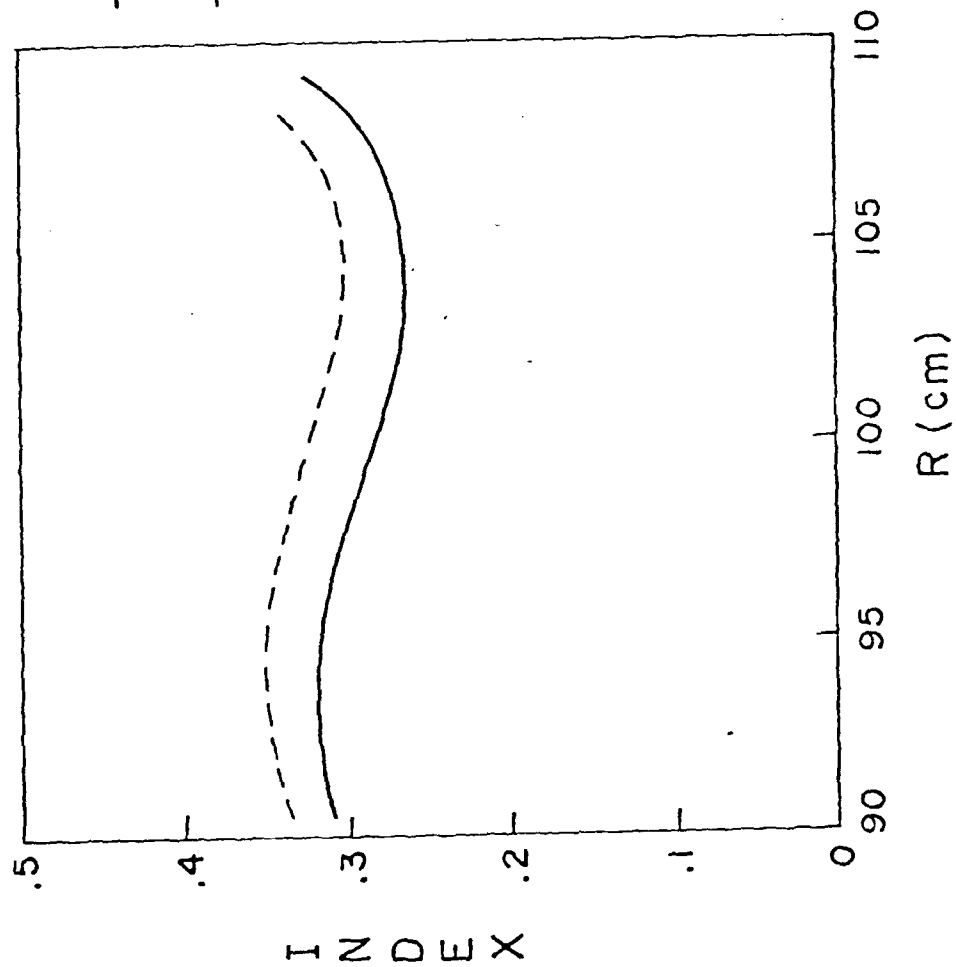
- B_z at Injection ($B_\theta = 2 \text{ K}$
 $B_z = 150$)
- Parallel Plate Bus

--- $Z = 10 \text{ cm}$
 - · - · - $Z = 0$
 — $Z = -10 \text{ cm}$



→ RELOCATING BUS WILL REDUCE ERROR, BUT FORCE IS STILL DIFFICULT TO HOLD (30 K LBS/FT), COAXIAL BUS APPEARS TO BE THE BEST SOLUTION.

T.F. BUS ERROR IN INDEX

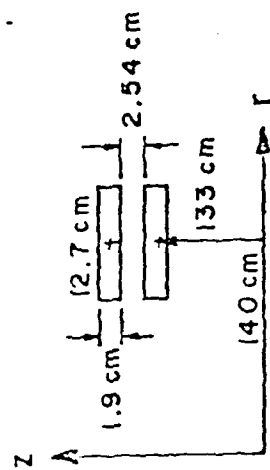


— Unperturbed Index

--- Perturbed Index

at Injection $B_{\theta} = 2 \text{ kG}$,
 $B_z = 150 \text{ G}$

o Parallel Plate Bus



TOTAL ENERGY AND CIRCUIT PARAMETERS

AFTER CONDUCTOR SELECTION THE TOTAL ENERGY CAN
BE CALCULATED,

$$\bullet E_T = E_{\text{COIL}} \left[1 + \frac{\tau R_I}{L_T} + \frac{L_{\text{BUS}}}{L_{\text{COIL}}} \right],$$

FROM TABLE V,

$$\underline{E_{TF} = 2.12 \text{ MJ}} \quad \text{AND} \quad \underline{E_{VF} = .66 \text{ MJ}}$$

THE CAPACITANCE IS DETERMINED FROM

$$\bullet X = \tan \left(\frac{\tau R_I}{2L_T} X \right), \text{ WHERE } C = \frac{4L_T/R_T^2}{X^2 + 1}$$

SEE TABLE V.

AD-A137 447

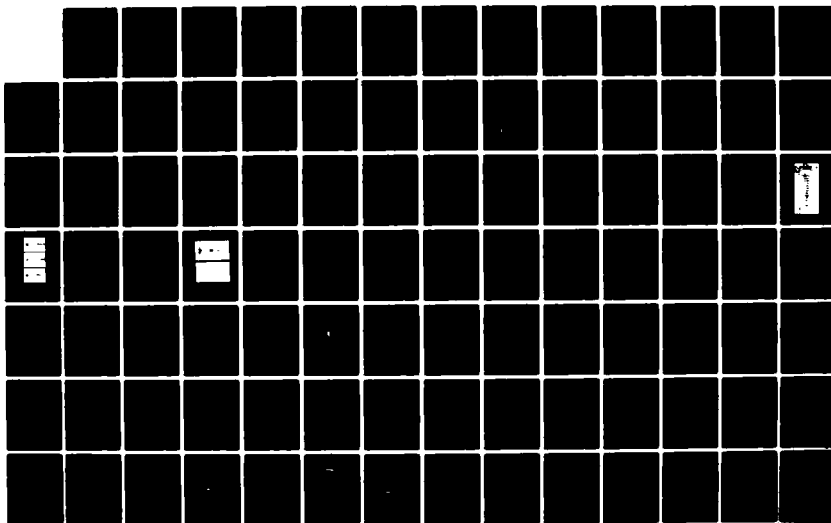
THE MODIFIED BETATRON ACCELERATOR EXPERIMENT(U) JAYCOR
ALEXANDRIA VA F M MAR 06 JAN 84
JAYCOR-J206-84-001/6207 N00014-81-C-2095

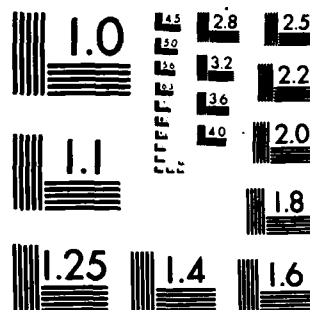
2/3

UNCLASSIFIED

F/G 20/7

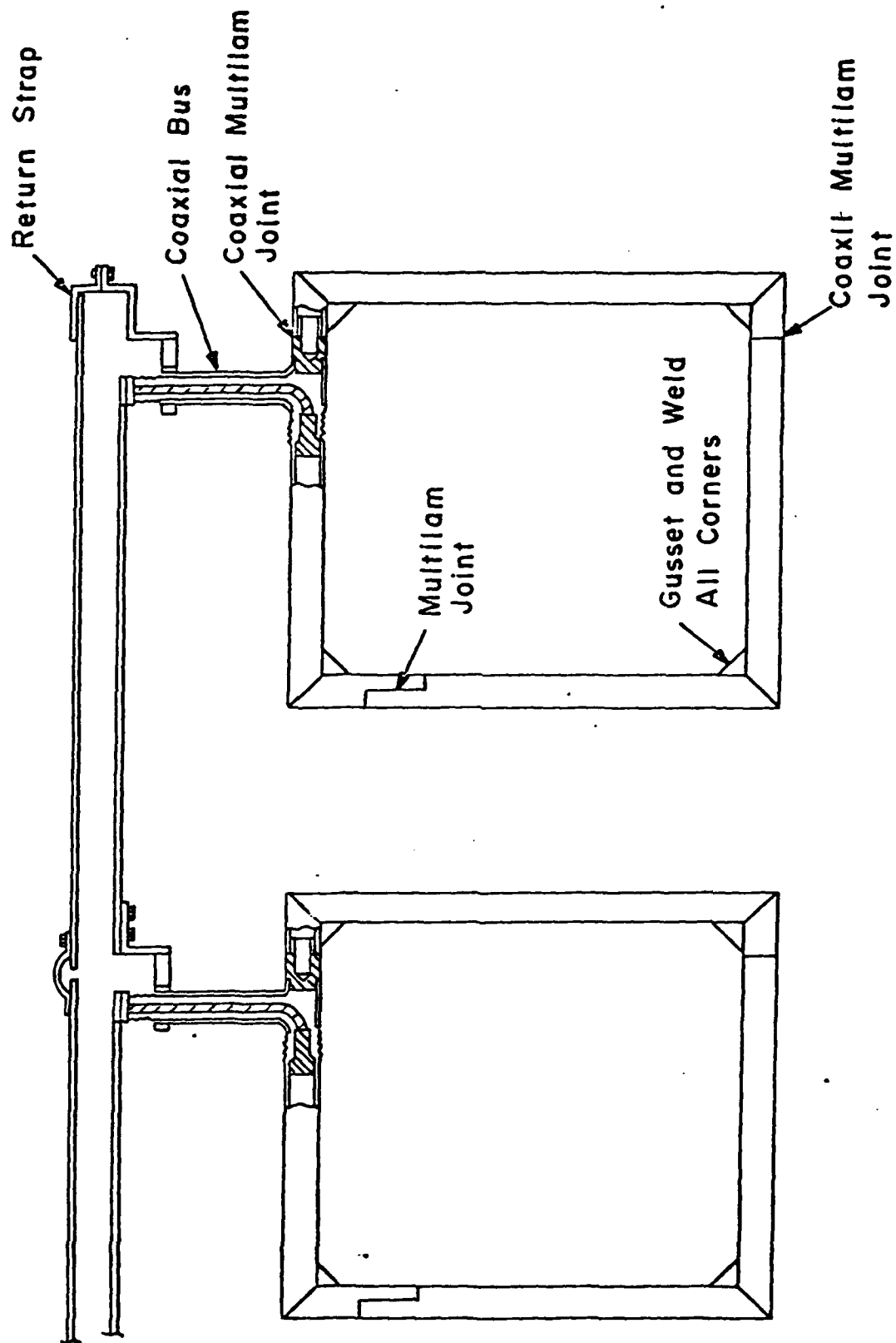
NL





MICROCOPY RESOLUTION TEST CHART
NATIONAL BUREAU OF STANDARDS-1963-A

PARAMETERS AND SPECIFICATIONS	TF SYSTEM	VF SYSTEM
COIL AC RESISTANCE ($m\Omega$)	0.65	2.9
BUS AC RESISTANCE ($m\Omega$)	0.52	12.4
JOINT DC RESISTANCE ($m\Omega$)	0.4	2
COIL INDUCTANCE (μH)	85	590
BUS INDUCTANCE (μH)	4.1	8.7
TIME TO REACH PEAK CURRENT (MS)	3.6	3.2
PEAK CURRENT (KA)	210	45
BANK ENERGY (MJ) (NOMINAL)	2.12	0.66
BANK CAPACITANCE (MF)	60.8	7.2
BANK VOLTAGE (KV)	8.5	13.6
COIL CROSS SECTION AND MATERIAL	4"x4"x $\frac{1}{2}$ " WALL 6061-T6 ALUM.	3"x3"x $\frac{1}{4}$ " WALL 6061-T6 ALUM.
VERTICAL BUS TO COIL, TYPE, SIZE AND MATERIAL	CIRCULAR COAX., 4" O.D., 3.36" I.D. OUTER CONDUCTOR 1.5" DIAM. INNER COND., 6061-T6 ALUMINUM	CIRCULAR COAX., 3.5" O.D., 3" I.D. OUTER CONDUCTOR 304 S.S., 1" DIAM., INNER COND., 6061-T6 ALUMINUM
COIL TO COIL BUS, TOP AND/OR BOTTOM DECK, TYPE, SIZE AND MATERIAL	RECTANGULAR COAX. 4"x8"x $\frac{1}{2}$ " WALL OUTER COND., 1"x 5" INNER COND. 6061-T6 ALUMINUM	SAME AS TF BUT AT T AND BOTTOM OF DECKS



Schematic of T.F. Coil To Coil Connection

SUMMARY AND CONCLUSIONS

- COIL AND BUSING DESIGN ISSUES ARE RESOLVED
- ENERGY LOSSES HAVE BEEN MINIMIZED
- LOW FIELD ERRORS CAN BE ATTAINED
- DEFLECTIONS CAN BE KEPT SMALL
- DETAILED BUS WORK DESIGN IS IN PROGRESS

External Injection into a High Current
Modified Betatron Accelerator

F. Mako, W. Manheimer, C. A. Kapetanakis
Naval Research Laboratory, Washington, DC 20375

D. Chernin
Berkeley Research Associates, Springfield, VA 22150
and F. Sandel

Sachs Freeman Associates, Bowie, MD 20715

NRL Memorandum Report 5196

September 9, 1983

Abstract

By axially tapering the current density at each end of an axial pinch a scheme is developed for injecting electrons across magnetic field lines into a modified betatron accelerator. This scheme produces only a minimal perturbation to the circulating electron beam. The axial pinch provides beam equilibrium in the transverse field and the tapering reduces the non-adiabatic growth of the perpendicular particle velocity from $0.5 c$ to $.05 c$ for the parameters of the NRL modified betatron.

Introduction

Presently, there is substantial interest in increasing the current limits of the conventional betatron.¹⁻² Several of these new approaches require at least a large toroidal magnetic field³⁻⁶ in addition to the conventional betatron field. The added toroidal field, however, makes the injection into the accelerator considerably more involved, because the injected beam must be transported across field lines before entering the torus.

In the modified betatron, i.e., an accelerator that combines a betatron and torodial field, this difficulty was avoided by locating the injector inside the torus.⁶ Such an injection scheme has several advantages but also three short comings. First, it requires a large opening on the torus, which introduces large field perturbations. Second, the debris of the diode can have an adverse effect on the quality of the vacuum system and third, it requires an injector with a short fall time to avoid perturbing the beam after the first revolution.

To avoid the difficulties of internal injection, we have developed a scheme to propagate the beam across magnetic field lines and thus to locate the injector outside the torus. In the proposed scheme, an axial pinch provides an equilibrium for the beam to cross field lines. Tapering of the current density at both ends of the axial-pinch is necessary to minimize the increase of the perpendicular particle velocity which results from the axial-pinch.

I. Electron Beam Motion

The proposed external injection scheme for the high current modified betatron is shown in Fig. 1. The anode of the injector is located at $y = 0$ and the intense beam propagates in a combined transverse and axial external magnetic field until it reaches the torus. The components of the magnetic

field for a uniform current density channel are given by,

$$B_x(z) = B_\psi \frac{z}{a} + B_{x0}, \quad (1)$$

$$B_z(x) = -B_\psi \frac{x}{a}, \quad (2)$$

$$B_y = B_{y0}. \quad (3)$$

where B_ψ is the magnitude of the plasma current magnetic field at the plasma radius a and B_{x0} , B_{y0} are the cartesian components of the toroidal magnetic field (B_θ) at the beam trajectory. The fields (B_ψ , B_{x0} , B_{y0}) are taken to be constants and the vertical magnetic field (B_{z0}) is ignored since its effect is the same as that of B_{x0} . In addition, the self fields are ignored, because the axial pinch plasma density is 5-6 orders of magnitude greater than a typical intense electron beam ($\sim 1\text{KA}/\text{cm}^2$) and thus charge and current neutralization is assumed.

After a change of variables (from time t to axial position y) using the transformation $\frac{d}{dt} = v_y \frac{d}{dy}$ and making the paraxial ray approximation [$(x'^2 + z'^2 \ll 1)$, where the prime is a derivative with respect to y] for the transverse motion, the equations of motion become

$$x'' + \frac{\Omega_\psi}{a v_0} x = -z' \frac{\Omega_y}{v_0}, \quad (4)$$

$$z'' + \frac{\Omega_\psi}{v_0 a} (z + \frac{\Omega_x}{\Omega_\psi} a) = x' \frac{\Omega_y}{v_0}, \quad (5)$$

$$\frac{dy}{dt} = \frac{v_0}{\sqrt{1 + x'^2 + z'^2}}, \quad (6)$$

where $\Omega_\psi = \frac{|e| B_\psi}{m\gamma}$, $\Omega_y = \frac{|e| B_{y0}}{m\gamma}$, $\Omega_x = \frac{|e| B_{x0}}{m\gamma}$, and $|e|$, m , γ and v_0 are the electronic charge, mass, relativistic factor and the magnitude of the (initial) velocity

vector respectively. Note also, the paraxial ray approximation implies;

$\Omega_x \ll \Omega_\psi < \Omega_y$ and small displacements.

According to Eq. (5) the B_x field displaces the particle orbits along the z -axis by, $-\frac{\Omega_x}{\Omega_\psi} a$. This is a general result and not a consequence of the paraxial ray approximation. Beam containment requires therefore that, $\Omega_x \ll \Omega_\psi$, that is, the peak field of the plasma current must be large compared to the crossed magnetic field.

The solution of Eqs. (4) and (5) is given by

$$z(y) = -\frac{\Omega_x}{\Omega_\psi} a + \left[x_0 \sin k_y y + \left(z_0 + \frac{\Omega_x}{\Omega_\psi} a \right) \cos k_y y \right] \cos ky$$

$$+ \left[\left(z'_0 - x_0 k_y \right) \cos k_y y + \left(x'_0 + z_0 k_y + k_y \frac{\Omega_x}{\Omega_\psi} a \right) \sin k_y y \right] \frac{\sin ky}{k}, \quad (7)$$

$$x(y) = \left[x_0 \cos k_y y - \left(z_0 + \frac{\Omega_x}{\Omega_\psi} a \right) \sin k_y y \right] \cos ky$$

$$+ \left[\left(z'_0 - x_0 k_y \right) \sin k_y y + \left(k_y z_0 + x'_0 + k_y \frac{\Omega_x}{\Omega_\psi} a \right) \cos k_y y \right] \frac{\sin ky}{k}, \quad (8)$$

and indicate oscillatory motion around the displaced axis. In Eqs. (7) and (8) $k_y = \frac{\Omega_y}{2v_0}$, $k = \sqrt{k_y^2 + \frac{\Omega_\psi^2}{av_0^2}}$, and x_0 , z_0 , x'_0 , and z'_0 are the initial positions and velocities respectively. Particle motion is characterized by two frequencies, a fast cyclotron motion at Ω_y and a slow rotation about the y -axis with a frequency of $\Omega_D = v_{y0} \Omega_\psi / a \Omega_y$, where v_{y0} is the magnitude of the initial axial velocity.

Although the axial pinch can provide the means for crossed field transport it also is the source for the growth of perpendicular energy. From Eqs. (7)-(8), with $x'_0 = z'_0 = 0$, the perpendicular energy is found to be,

$$\epsilon_\perp(y) = 2m v_{y0}^2 \left[\left(\frac{x_0 \Omega_\psi}{a \Omega_y} \right)^2 + \left(\frac{z_0 \Omega_\psi}{a \Omega_y} + \frac{\Omega_x}{\Omega_y} \right)^2 \right] \left[1 + 4 \frac{\Omega_D^2}{\Omega_y^2} \right] \sin^2 ky.$$

Since $\Omega_\psi \gg \Omega_x$ most of the perpendicular energy comes from the pinch, except for particles near the axis. However, in practice, most electron beams have more particles at a large radius.

An accurate calculation of the perpendicular velocity cannot be based on the paraxial equations. However, the more general equations are not easily tractable analytically. For this reason, it is assumed that $\Omega_x = 0$. Under this assumption, it can be shown from the conservation of axial P_y and canonical angular P_ψ momentum that,

$$2t = \int_{\zeta_0}^{\zeta} \frac{d\zeta}{\left\{ - \left[\frac{\Omega_y^2}{4} + \frac{P_y \Omega_\psi}{\gamma m a} \right] \zeta^2 + \left[u_0^2 - \frac{P_\psi \Omega_y}{\gamma m} - \left(\frac{P_y}{\gamma m} \right)^2 \right] \zeta - \left(\frac{P_\psi}{\gamma m} \right)^2 \right\}^{1/2}} \quad (9)$$

where $\zeta = \rho^2$, and $\frac{\Omega_\psi \rho^2 / 2a}{P_y / \gamma m}$ is the small expansion parameter.

From (9) the maximum radial velocity is,

$$u_{\rho \max} = \frac{\Omega_y \rho_0}{\sqrt{2}} \left\{ 1 + \frac{1}{2} \left(\frac{\Omega_y}{u_{y0}} \rho_0 \right)^2 - \left(1 - \left(\frac{\Omega_\psi}{2u_{y0}} \rho_0 \right)^2 \right)^2 \right\}^{1/2} + 2 \frac{\Omega_D}{\Omega_y}$$

$$= \left[1 + 4 \frac{\Omega_D}{\Omega_y} \left(1 - \frac{1}{2} \frac{\Omega_\psi a}{u_{y0}} \left(\frac{\rho_0}{a} \right)^2 \right) \right]^{1/2}$$

where ρ_0 is the initial value of ρ . For, $B_y = 2\text{KG}$, $B_\psi = 2\text{KG}$, $\rho_0 = a = 2\text{ cm}$, and $\gamma = 7$, the ratio $\frac{u_{\rho \max}}{u_{y0}} = 0.45$, which is too large to be acceptable.
 and $v_{x0} = v_{z0} = 0$

By numerically integrating the exact relativistic particle equations we obtain $u_{\rho \max}/c = 0.45$ (where c = speed of light). The numerically calculated radial velocity is shown in Fig. 2a. The results of Fig. 2a were obtained for the general case, i.e., when a transverse field is present, in addition to the axial and plasma current magnetic fields. The values of the various parameters are listed in the figure captions. Shown also in Fig. 2a are the axial profiles of the fields.

A substantial reduction of the perpendicular velocity can be achieved by axially tapering the current density at both ends of the pinch. Although the pinch field is the primary source of v_{\perp} , non-adiabatic effects contribute significantly to v_{\perp} but can be removed by an adiabatic taper. Results are shown in Fig. 2b. For a large taper length a perturbation calculation predicts a v_{\perp} that is within 20% of the numerical results. To substantially reduce the perpendicular velocity the taper length must be several times the betatron wavelength. An expression for the betatron wavelength can be calculated from Eqs. (6), (7), (8) and is given by,

$$\lambda = 2\pi \frac{v_{y0}}{\Omega_y} \left[1 + 4 \frac{\Omega_D}{\Omega_y} \right]^{-1/2}$$

Figure 3 shows the reduction of the perpendicular velocity as a function of the ratio of taper length to betatron wavelength, this is shown with and without transverse fields. For $B_y = 2\text{KG}$, $B_z = 2\text{KG}$, $a = 2\text{ cm}$, $\gamma = 7$ the betatron wavelength is approximately, $\lambda = 10.4\text{ cm}$. To reduce v_{\perp}/c substantially would require a taper length of 20-30 cm.

The feasibility of tapering the current density has been tested experimentally. Presently, a taper length of 25 cm has been achieved experimentally. The measured azimuthal magnetic field B_{θ} of the pinch with and without tapering is shown in Fig. 4. This current density profile was achieved by geometrically tapering the vacuum chamber. A cylindrical resistor taper is presently being examined for making a radially compact taper.

II Plasma Interaction

Calculations indicate that the axial pinch does not substantially interact with the electron beam nor with the external fields. However, there are limits imposed on the plasma density. To avoid an unacceptably large

displacement of the plasma column from the $J_y \times B_x$ force and enhancement of the beam emittance, the plasma density should satisfy the inequalities (in CGS)

$$\frac{\epsilon^2 \beta^2}{8\pi DZ (Z+1) \ell r_e^2 \rho_0^2 \ln [a_0 \gamma \beta^2 / 2Z^{4/3} r_e]} > n > \frac{B_\psi B_{x0} \tau^2}{4\pi \Delta z A m_p a}$$

where ϵ is the maximum beam emittance, ℓ is the length of the plasma column, Z, A are the atomic number and weight of the gas, Δz is the maximum plasma channel displacement, m_p is the proton mass, $r_e = \frac{e^2}{mc^2}$, $a_0 = \frac{\hbar^2}{me^2}$, $D = 1$ for monotomic, $D = 2$ for diatomic gas. Also, τ is the time that has elapsed from the beginning of the pinch to when the electron beam is injected. Instabilities will be considered elsewhere.

Summary

Using a tapered axial pinch of suitable plasma density and current appears so far to provide a low perturbation scheme for beam injection into a modified betatron. Extensive analytical and computational work indicates that the transverse particle velocity at the exit of the plasma column is substantially smaller than in an untapered pinch. Preliminary experimental results indicates that a pinch with tailored axial current density is achievable.

References

1. D. W. Kerst, Phys. Rev. 58, 841 (1940).
2. D. W. Kerst, G. O. Adams, H. W. Koch, and C. S. Roberson, Phys. Rev. 78, 297 (1950).
3. C. A. Kapetanacos, P. Sprangle, D. P. Chernin, S. J. Marsh, and I. Haber, Phys. Fluids 26, (6) (1983).
4. N. Rostoker, Comments Plasma Phys. Controlled Fusion 6, 91 (1980).
5. C. W. Roberson, A. Mondelli, and D. Chernin, Phys. Rev. 50, 507 (1983).
6. C. A. Kapetanacos, P. Sprangle, and S. J. Marsh, Phys. Rev. Lett. 49, 741 (1982).

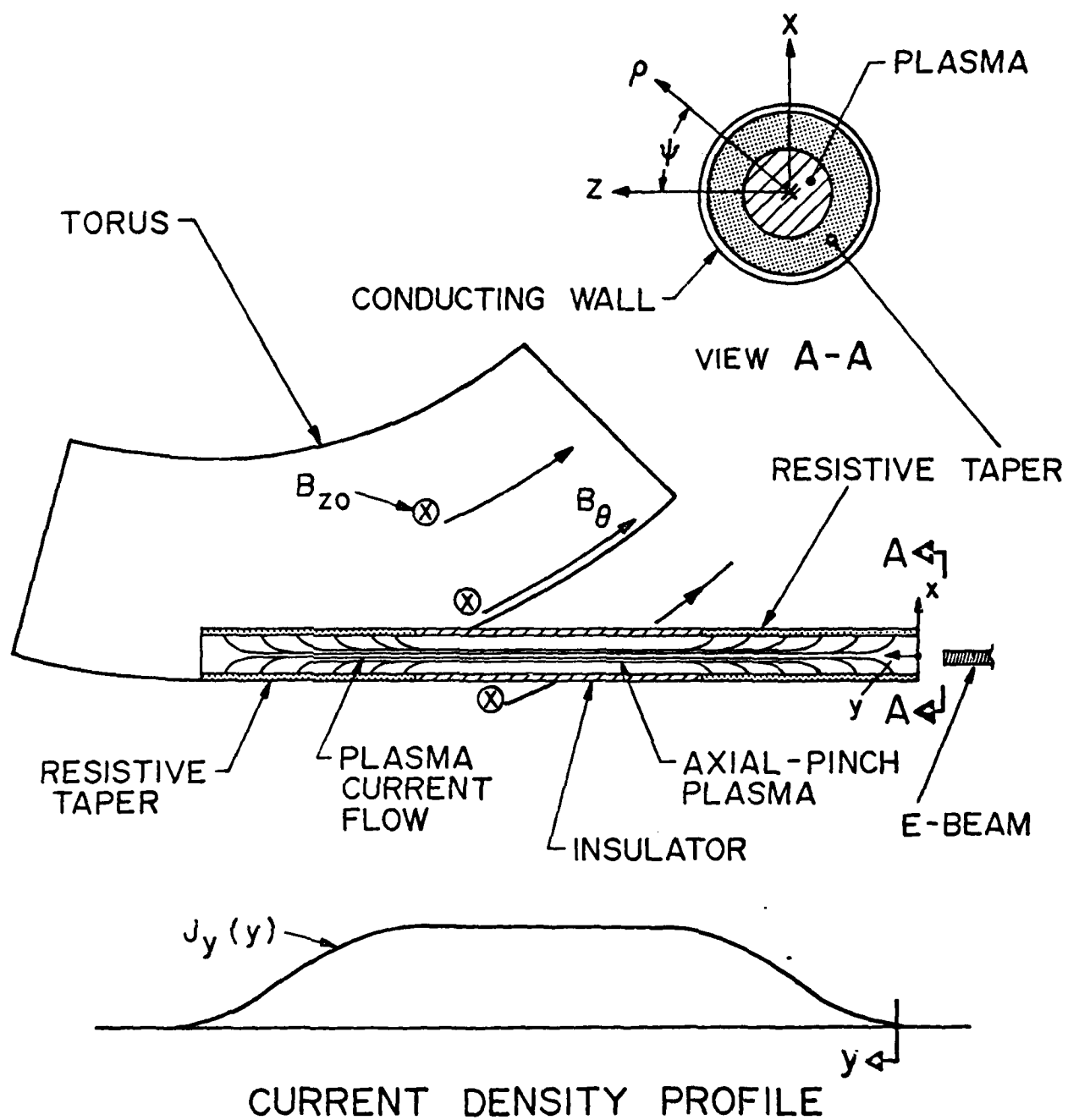


Figure 1. Schematic of tapered axial-pinch injector.

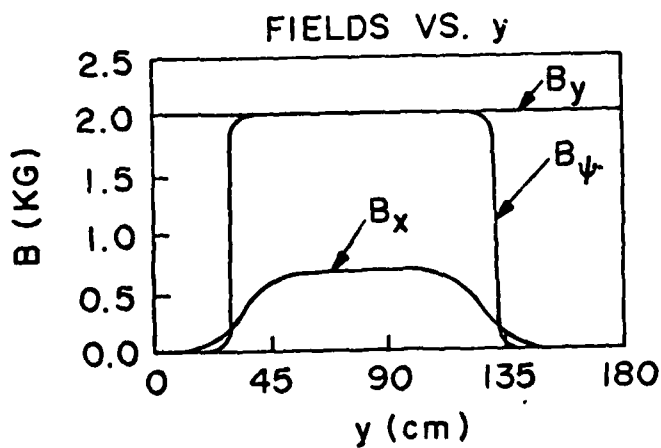
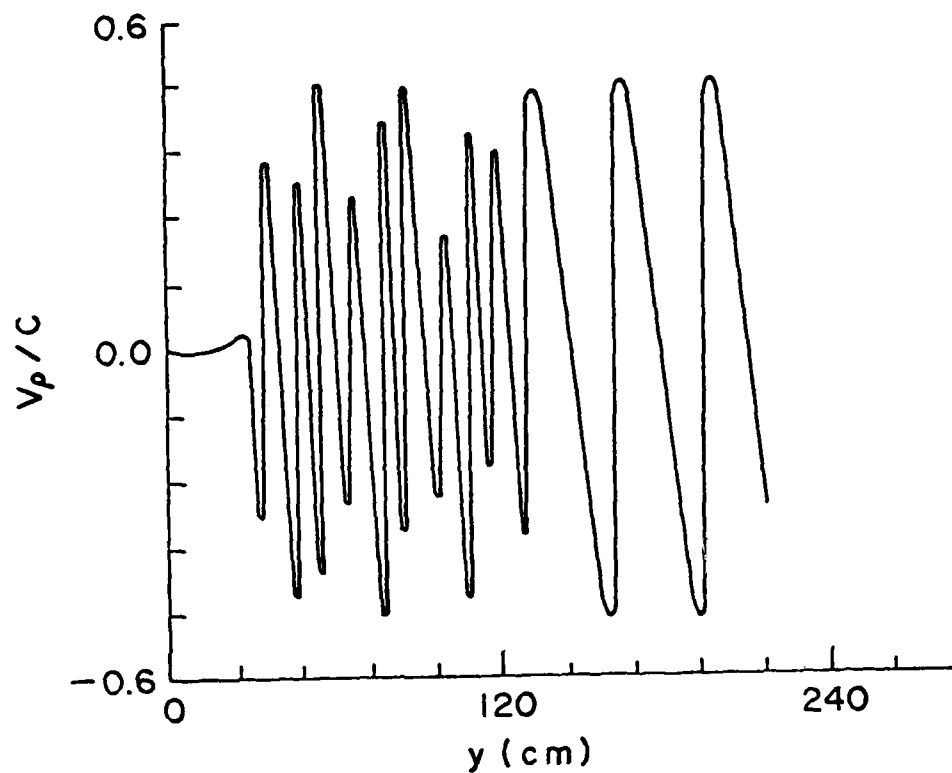


Figure 2a. Transverse particle velocity vs axial positions. The particle parameters are: $\gamma_y = 7$, $\gamma_\perp = 0$ and $P_0 = a = 2$ cm. Taper length from 10-90 percent amplitude is 2.2 cm. c = speed of light.

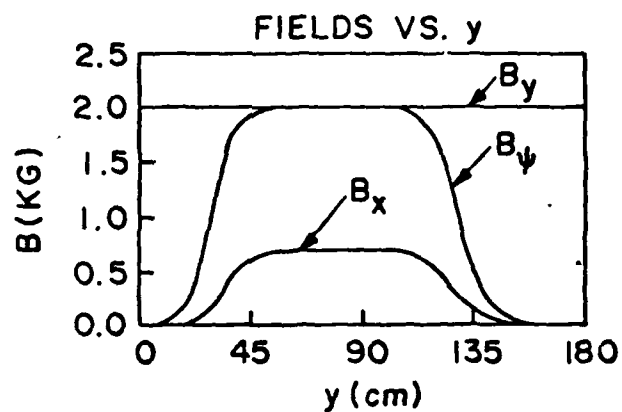
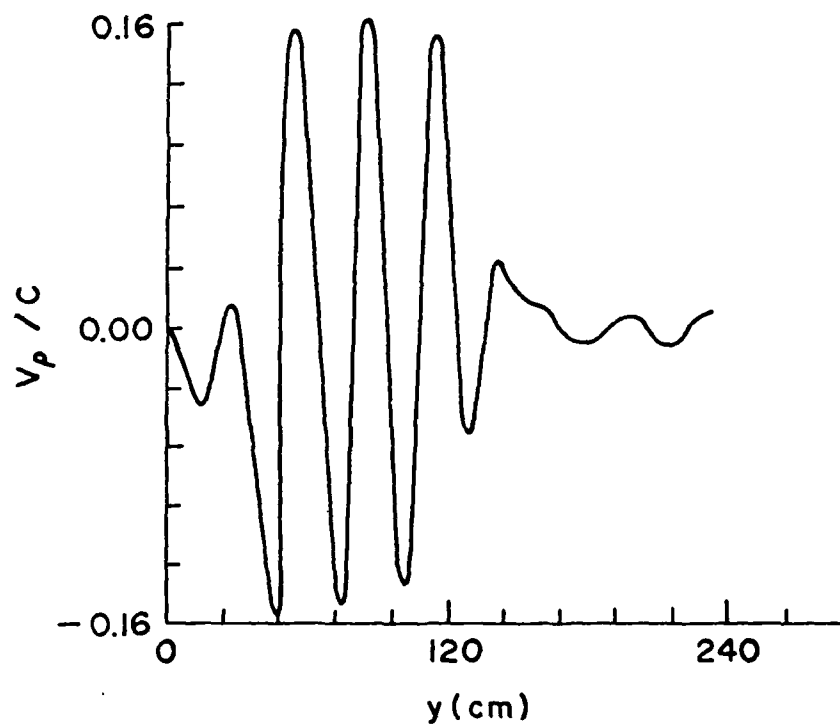


Figure 2b. Transverse particle velocity vs axial position. The same parameters as in Figure 2a but the taper length is 22 cm.

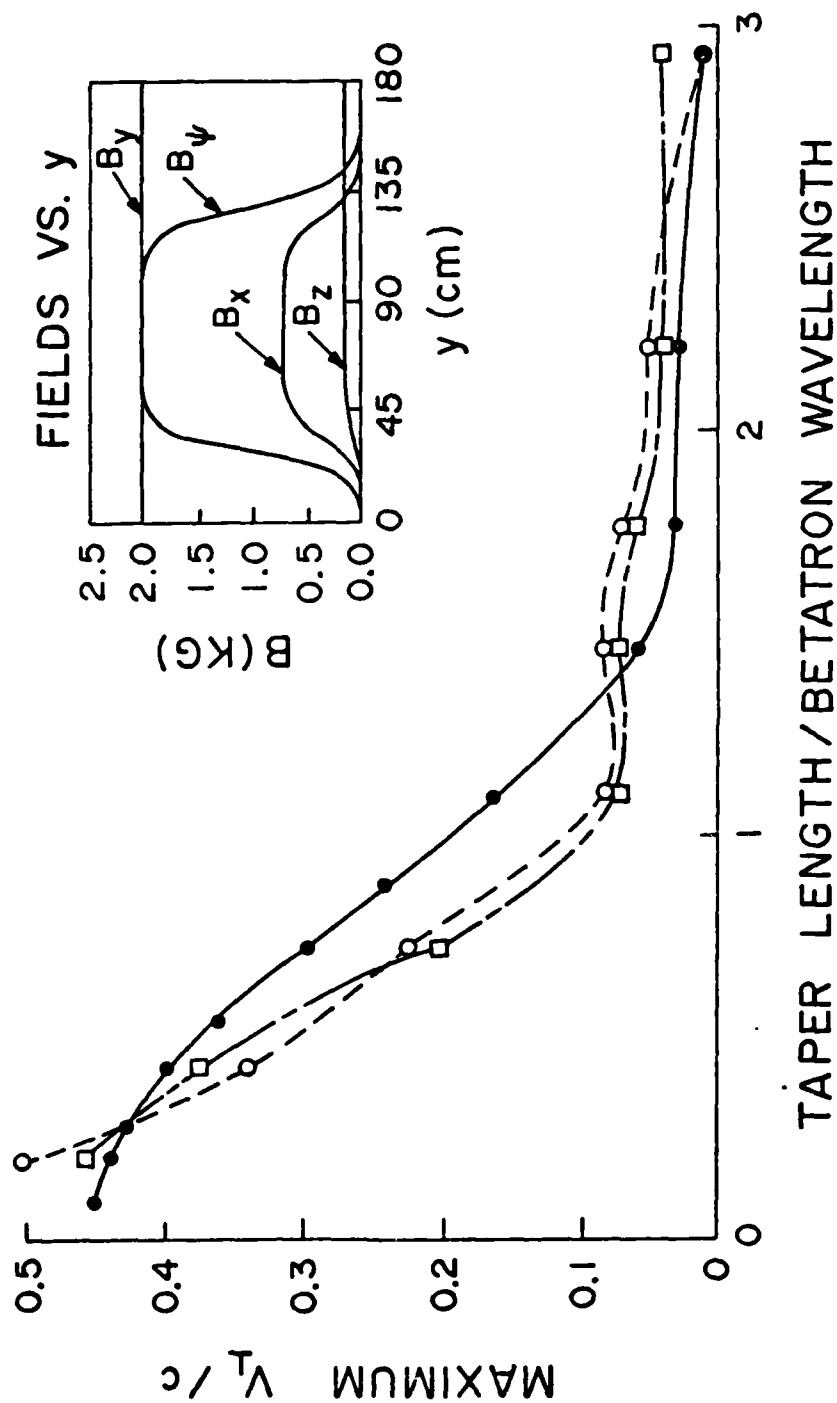


Figure 3. Maximum transverse particle velocity vs taper length. The same parameters as in Figure 2a but with variable taper length and crossed fields.

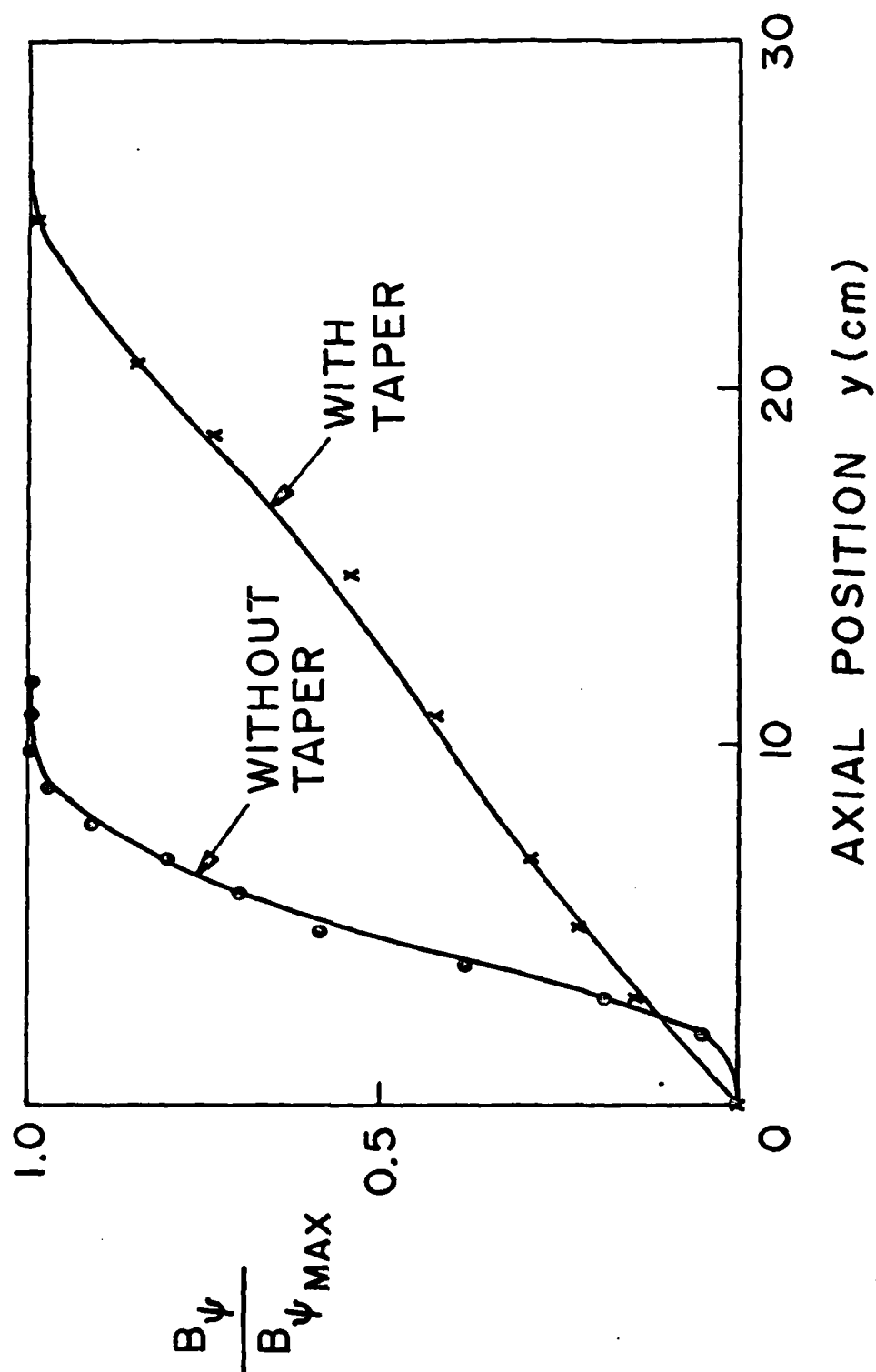


Figure 4. Axial pinch magnetic field vs axial position. Dots and crosses are experimental data and the curves indicate trend of data.

Electron Drift in a Linear Magnetic Wiggler
with an Axial Guide Field

J. A. Pasour, F. Mako and C. W. Roberson
Naval Research Laboratory

J. Appl. Phys. 53 (11)
November 1982

Electron drift in a linear magnetic wiggler with an axial guide field

J. A. Pasour, F. Mako,^{ab} and C. W. Roberson
Naval Research Laboratory, Washington, DC 20375

(Received 5 April 1982; accepted for publication 21 July 1982)

Electron trajectories through a linear magnetic wiggler in an axial guide field are calculated numerically. Off-axis electrons are shown to drift in a direction perpendicular to the wiggler field because of the wiggler gradient. Effects of self-fields and initial conditions are analyzed, and the results compared to those obtained with a helical wiggler. An empirical analytic expression for the linear wiggler drift is presented, and means of stabilizing the drift are discussed.

PACS numbers: 41.70. + t, 41.80.Dd

Recently, there has been much interest in free electron lasers (FEL's) which use spatially varying magnetic fields to modulate a relativistic electron beam (REB).¹⁻⁵ Three types of magnetic wigglers have been widely used: helical (usually produced by a bifilar helical current winding^{6,7}), linear (produced by an array of permanent magnets⁸ or by linearly alternating windings⁹), and radial¹⁰ (produced by a series of spaced conducting or ferromagnetic washers¹¹ immersed in an axial field or by a series of alternating coils³). Of these, only the first two produce a perpendicular field on axis and are therefore suitable for use with a small diameter beam of solid cross section. In this paper, we will analyze the propagation of a solid, high current REB through linear and helical wigglers with a superimposed axial guide field.

FEL experiments fall into two categories depending on the beam current. Compton regime FEL's^{1,2,5} have used high energy (tens of MeV), low current (≤ 1 A) beams while Raman FEL's^{3,4} have used lower energy (~ 1 MeV), high current (≥ 1 kA) beams. Helical wigglers have been used in both current regimes, but until recently⁹ linear wigglers were used only in the Compton regime. In this case, the linear wigglers consist of permanent magnets and there is no guide field. However, for high current beams, a guide field is required to contain the beam. Although there are advantages to a linear wiggler from the standpoint of ease of assembly and versatility (e.g., changing the periodicity or tapering the period and/or field amplitude for efficiency enhancement¹²) we will show that there is no equilibrium for off-axis particles when a beam is propagated through a linear wiggler in an axial field. The particles drift out of the wiggler unless additional focusing forces are provided.

Various authors have considered particular cases of electron motion through magnetic wigglers. These have typically been single particle (low current) calculations. Blewett and Chasman⁷ considered motion of high energy electrons (~ 24 MeV) through a helical wiggler and found stable helical orbits with superimposed betatron oscillations. Friedland¹³ has treated the case of lower energy electrons (~ 300 keV) in an idealized radially uniform helical wiggler with a superimposed axial guide field. He showed that various stable trajectories were possible and derived stability criteria relating the allowed wiggler and guide field strengths to beam energy and wiggler period λ_w . These "stable" regions are given by

^aJAYCOR, Alexandria, VA 22304.

$$\frac{B_w}{B_0} < \left[\left(\frac{vk}{\Omega_0} \right)^{2/3} - 1 \right]^{3/2} \quad (2a)$$

and

$$\Omega_0 > ck, \quad (2b)$$

where B_0 is the axial guide field, $\Omega_0 = eB_0/\gamma m$ is the corresponding cyclotron frequency, v is the electron velocity, and $k = 2\pi/\lambda_w$. Physically, these conditions stem from the resonance in the perpendicular velocity of an electron in the wiggler and guide fields:

$$v_w = - \frac{v_z \Omega_0}{v_z k - \Omega_0} \quad (3)$$

Freund and Drobot¹⁴ have considered this case further and also conclude that stable trajectories with nearly constant axial velocities and relatively large wiggler amplitudes are possible when $\Omega_0 \ll ck$. This is consistent with condition (2a).

The present analysis employs a relatively simple computer code which solves the equations of motion of an electron in any electric and magnetic field configuration using a fourth-order Runge-Kutta method. Self-electric and magnetic fields are calculated by assuming that the electron is at the edge of an azimuthally symmetric beam of current I , so that the self-fields can be written as (mks)

$$E_r = \frac{-I}{2\pi\epsilon_0 r v_z}, \quad (4)$$

$$B_\theta = \frac{-\mu_0 I}{2\pi r},$$

where $r(t)$ is the electron radius. The axial self-fields are neglected.

For the particular cases considered here, the external magnetic field consists of a solenoidal field produced by a 15.3-cm-i.d. \times 2-m-long solenoid together with a wiggler that begins in the uniform portion of the solenoidal field. The wiggler field, which may be either helical or linear, rises adiabatically over ten periods and then oscillates with constant amplitude. The envelope enclosing the wiggler amplitude is given by

$$b(z) = \begin{cases} \frac{1}{2} \left[\left(\frac{z}{10\lambda_w} \right)^2 + \left(\frac{z}{10\lambda_w} \right)^3 \right], & 0 \leq z < 10\lambda_w \\ 1, & z > 10\lambda_w \end{cases} \quad (5)$$

Here, z is the axial distance from the beginning of the wiggler. This variation closely fits the linear wiggler used in the NRL induction linac FEL. The field on axis from this wiggler is plotted in Fig. 1 along with the envelope equation (5).

The linear wiggler field components are

$$\begin{aligned} B_z' &= b(z)B_w \cosh kx \cos kz, \\ B_y' &= 0, \\ B_x' &= -b(z)B_w \sinh kx \sin kz, \end{aligned} \quad (6)$$

where B_w is the peak wiggler field on axis. For the NRL linear wiggler,⁹ which has $\lambda_w = 3$ cm and winding layers spaced by 3.2 cm, these expressions are valid for $r \leq 1$ cm.

We will be primarily concerned with relatively low energy (~ 1 MeV), high current (\sim kA) beams. Of particular interest are the effect of self-fields, guide field and wiggler amplitude, and initial beam conditions corresponding to a field immersed ($v_{\theta 0} = 0$) or a shielded source ($P_{\theta 0} = 0$), where $v_{\theta 0}$ is the initial azimuthal electron velocity and $P_{\theta 0}$ the initial canonical angular momentum. If the axial self-magnetic field is neglected, $P_{\theta 0} = 0$ implies $v_{\theta 0} = erB_z/(2\gamma m)$ in a uniform field B_z .

First, we consider a beam with $\gamma = 2.2$, $I = 250$ A, $B_0 = 2$ kG, $B_w = 1$ kG, and $\lambda_w = 3$ cm. Note that Eq. (2a) would require $B_w < 3$ kG for stability in this case with a helical wiggler. The x - y trajectories of electrons injected with $v_{\theta 0} = 0$ and $r_0 = 0.4$ cm into a linear wiggler are shown in Fig. 2. Each particle initially begins to $E \times B$ drift in the self-fields, but when it reaches a region of large wiggler field it begins drifting in the y direction. In each case the electron reaches an imaginary wall, located at $r = 1.2$ cm, only partially transverse the wiggler. It should be noted that the assumptions used to calculate the self-fields become invalid as the beam distorts. Consequently, to determine if these self-fields are responsible for this drift, the calculations are repeated with $I = 0$ (Fig. 3). A third trajectory is also plotted for $B_w = 0.5$ kG. The electron that originates on the y axis is well confined, but electrons off the y axis again drift to the wall, with a velocity much higher for $B_w = 1$ kG ($\langle v_d \rangle$

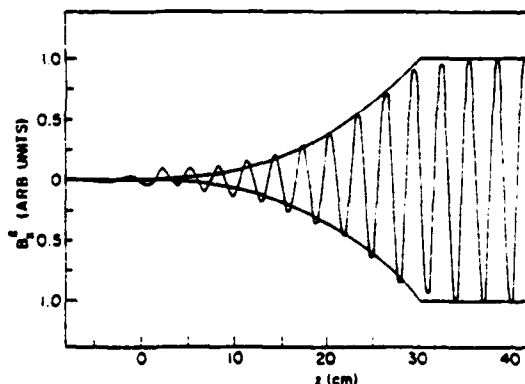


FIG. 1. Plot of measured $B_z'(z)$ from NRL linear wiggler together with envelope $b(z)$ from Eq. (5).

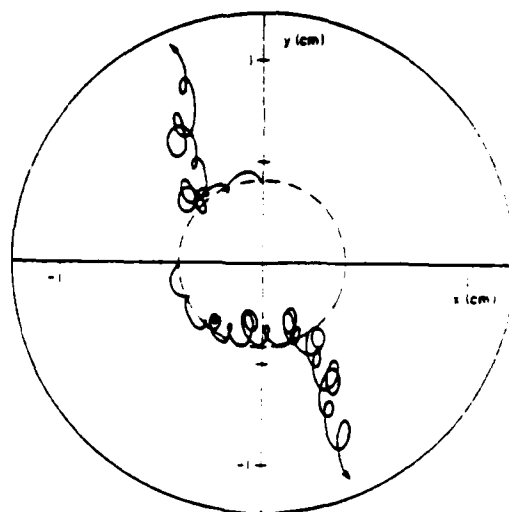


FIG. 2. Electron trajectories in linear wiggler with $\lambda_w = 3$ cm, $B_0 = 2$ kG, $\gamma = 2.2$, $r_0 = 0.4$ cm, $I = 250$ A, and $B_w = 1$ kG.

≈ 0.047 c) than for $B_w = 0.5$ kG ($\langle v_d \rangle \approx 0.011$ c).

This behavior can be explained by the increasing gradient in the wiggler field, and consequently the emergence of a significant axial field component, as the distance from the y axis increases. Although the present drift arises from the gradient in B_w and is in the direction of $\nabla B_w \times B_0$, it is quantitatively different from the usual guiding center approximation because the field variation over one gyroperiod is so extreme. For example, when $kx = 0.8$ ($x \approx 0.4$ cm in the present case), B_x' varies from $+B_w$ to $-B_w$ over one period. However, the physical mechanism is the same as for the usual gradient drift; i.e., the gyroradius in the part of the

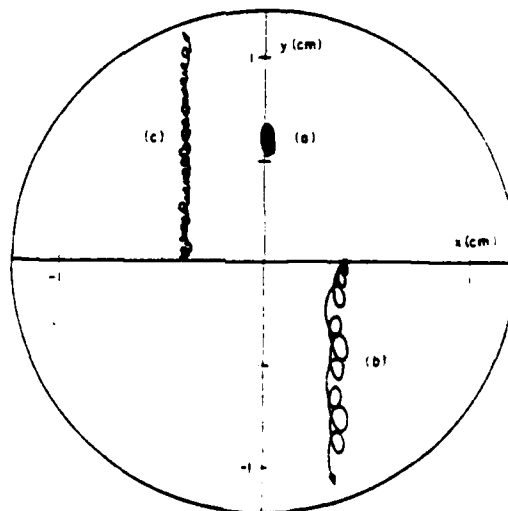


FIG. 3. Electron trajectories in linear wiggler with $\lambda_w = 3$ cm, $B_0 = 2$ kG, $\gamma = 2.2$, $r_0 = 0.4$ cm, and $I = 0$. $B_w = 1$ kG for particles a and b and $B_w = 0.5$ kG for particle C.

TABLE I. Comparison of drift velocities computed from the code with those from Eq. (9) for various cases.

B_0 (kG)	B_w (kG)	γ	Ω_0/kv_z	X (cm)	V_d/c (code)	V_d/c [Eq. (9)]
2	1	2.2	0.29	0.4	0.047	0.050
4	1	2.2	0.57	0.4	0.042	0.046
2	0.5	2.2	0.29	0.4	0.011	0.013
2	1	2.2	0.29	0.2	0.019	0.022
2	1	3.0	0.21	0.4	0.029	0.034
4	1	3.0	0.42	0.4	0.019	0.022
4	0.5	3.0	0.42	0.4	0.0051	0.0056
4	1	10.0	0.11	0.4	0.0043	0.0049
10	5	10.0	0.28	0.4	0.057	0.056

orbit where B_z is a minimum, or where $\|x\|$ is a minimum in Fig. 3, is larger than where B_z is a maximum. The addition of self-fields merely imposes an additional $E \times B$ rotation on the orbit, so that an electron that originates on the y axis (and is therefore confined when $I = 0$) begins to drift into a region of increasing B_z . Therefore, it actually is "lost" sooner than an electron on the x axis which initially $E \times B$ drifts into a region of smaller B_z .

An approximate, empirical expression for the drift has been found which is in quite good agreement with the code results when $\Omega_w < \Omega_0 < kv_z$ (below the cyclotron resonance). In terms of the wiggler gradient, the expression is

$$v_d \approx \frac{1}{2} \frac{v_z^2}{\Omega_0} \frac{\nabla(B')^2}{2(B')^2} \times \frac{B_0}{B_0}, \quad (7)$$

which has the same form as the usual grad B drift but is quantitatively different. The single particle equations of motion are $\dot{v}_x = -v_z \Omega_z$, $\dot{v}_y = -v_z \Omega_z + v_z \Omega_z$, and $\dot{v}_z = v_z \Omega_z$. Assuming $v_z \approx$ constant and that the gyration velocities are $v_x = v_{1x} \sin kz$ and $v_y = v_{1y} \cos kz$, it follows that

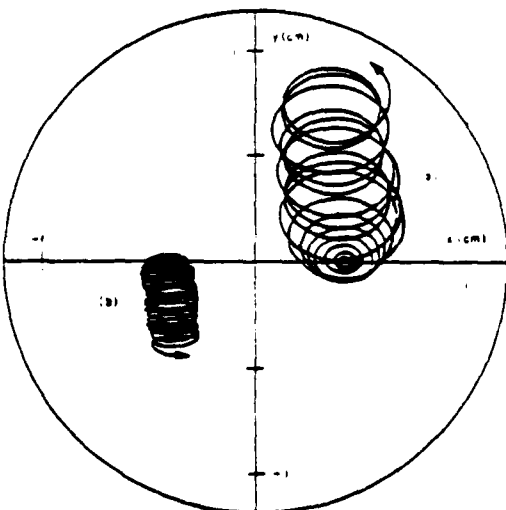


FIG. 4. Electron trajectories in linear wiggler with $I = 0$, $\gamma = 2.2$, $B_w = 1$ kG, and $r_0 = 0.4$ cm. (a) $B_0 = 8$ kG. (b) $B_0 = 10$ kG.

$$v_{1y} \approx v_z \frac{kv_z \Omega_w \cosh kx}{\Omega_0^2 - k^2 v_z^2}, \quad (8)$$

$$v_{1x} \approx v_z \frac{\Omega_0 \Omega_w \cosh kx}{\Omega_0^2 - k^2 v_z^2}.$$

for $B_z' > B_z$. These assumptions are reasonably valid for $kx \lesssim 0.8$ and for B_0 sufficiently far from resonance and B_w small enough that $v_z \ll v_{1z}$. Furthermore, to insure that $\cosh kx \approx$ constant over the orbit, we restrict $v_{1x} \ll v_z$, (i.e., $\Omega_0 < kv_z$). Then using Eqs. (8) and (6) in Eq. (7), we obtain

$$v_d \approx \frac{1}{2} v_z \frac{kv_z}{\Omega_0} \frac{(\Omega_w kv_z)^2}{(\Omega_0^2 - k^2 v_z^2)^2} \cosh kx \sinh kx. \quad (9)$$

Table I compares drift velocities for various cases from the code with $I = 0$ to those from Eq. (9). In general, the agreement is very good.

Clearly, the gradient drift is more severe when B_w is a considerable fraction of B_0 . However, if B_w is held constant at 1 kG and B_0 increased to 4 kG, v_d ($\gamma = 2.2$) is not significantly reduced. This relative insensitivity to B_0 is due to the increased v_{1z} , and hence a larger v_d , as B_0 approaches the cyclotron resonance field B_c . One consequence of this large drift near resonance is that it limits the degree of gain enhancement achievable through the magnetoresonance effect.⁴

If B_0 sufficiently exceeds B_c , the drift can be quite small. For $\gamma = 2.2$ and $\lambda_w = 3$ cm, the resonant magnetic field $B_c \approx 7$ kG. With $B_0 = 8$ kG and $B_w = 1$ kG, the particle still drifts to the wall as shown in Fig. 4(a). The drift is now in the opposite direction to that below resonance since v_{1z} changes sign with $B_z > B_c$. This has the effect of changing the phase of v_z oscillations with respect to those of B_z ; i.e., v_z is positive (for $x > 0$) when B_z is a minimum, so that the particle drifts in the $+y$ direction. When B_0 is increased to 10 kG for this case, the drift is small enough that the electron remains confined for > 30 periods as shown in Fig. 4(b). The confinement remains very good when the self-fields of a 500-A beam are added.

In principle, operation of FEL experiments with $B_0 > B_c$ is possible and has been demonstrated with a high current, $\gamma \approx 3.5$ beam in a helical wiggler.⁴ However, competing processes such as the cyclotron maser¹⁵ interaction can in general produce large radiated powers at frequencies

close to those of the FEL interaction for beam energy ~ 1 MeV and $B_0 \gtrsim 10$ –20 kG. Consequently, analysis of experimental results is more difficult. Also, arbitrarily large guide fields are not possible with a magnetically shielded diode simply because the electrons will be mirrored by the field. The equilibrium beam radius¹⁶ in such a case depends only on γ , I , B_0 , and the beam emittance ϵ , so for particular beam parameters suitable values of B_0 are limited. The required field¹⁷ in kG for a matched beam radius R in cm can be written

$$B^2 = \frac{1.36 I}{R^2 B \gamma} + \frac{11.56 \epsilon_n^2}{R^4}, \quad (10)$$

where I is in kA and ϵ_n is the normalized emittance in rad cm. For example, if $\epsilon_n = 0.14$ rad cm (about the lowest value expected for a thermionic cathode beam with $I \approx 750$ –1000 A),¹⁷ a $\gamma = 2.2$ beam with $R = 0.3$ (0.5) cm requires $B_0 = 5.5$ (2) kG for $I \leq 800$ A. In this regime, the beam is emittance dominated so that the required field is relatively insensitive to I . In principle, smaller radius beams could be used with larger B_0 , thereby doubly reducing v_d . However, experimentally this is very difficult at high current levels.¹⁶

To analyze the effect of a shielded diode on propagation through the wiggler, we repeat the above calculations with an initial v_d corresponding to $P_{d0} = 0$. Note that $I = 1.75$ kA in this case, which is the current required for constant radius propagation in only the solenoidal field with these initial conditions. As shown in Fig. 5, the electron propagates at nearly constant radius until the wiggler amplitude becomes large enough that the gradient drift begins to dominate. Then the particle is lost just as in the $v_{d0} = 0$ case.

The behavior of an off-axis electron in a linear wiggler and axial guide field should be compared to that when a helical wiggler is used.¹³ We approximate the helical wiggler field by⁶

$$B_z^h = b(x)B_w [-\sin kz \{1 + \frac{1}{2}k^2(x^2 + y^2)\} + \frac{1}{2}k^2xy \cos kz], \quad (11)$$

$$B_y^h = b(x)B_w [\cos kz \{1 + \frac{1}{2}k^2(x^2 + y^2)\} - \frac{1}{2}k^2xy \sin kz],$$

$$B_x^h = -kb(x)B_w [1 + \frac{1}{2}k^2(x^2 + y^2)](x \cos kz - y \sin kz).$$

This expansion of the true Bessel function expression for B^h is valid for $kr \ll 1$. Friedland's treatment¹³ of electron propagation in this case assumes a radially uniform wiggler, and his stability condition [Eq. (2a)] is not stringent enough when the radial variation is included. For example, Friedland finds stable orbits when $\gamma = 1.587$, $B_w = 4$ cm, $v_{d0} = 0$, $r_0 = 0$, $B_0 = 1.26$ kG, and $B_w = 1.04$ kG, so that Eq. (2a) is barely satisfied, and we can duplicate his results if we remove the radial variation from B^h . However, with the B^h given in Eq. (11), we find that the wiggler field must be reduced to ~ 625 G to obtain stable orbits.

Although the radial dependence in B^h does narrow the allowable range of operating parameters, stable orbits with $\langle r \rangle \approx \text{constant}$ are achievable with a helical wiggler in a guide field. Electron trajectories in a helical wiggler for the same conditions as used previously with a linear wiggler are shown in Figs. 6 and 7. Figure 6 is to be compared to Fig. 2 and Fig. 7 to Fig. 5. In both cases, the electron is well confined. It is interesting to note that in Fig. 6, the electron born at $(x, y) = (0.4, 0)$ initially $E \times B$ drifts in the $+\theta$ direction, but then reverses direction as the wiggler amplitude increases. Since $\text{grad } B^h$ is radial, the $\text{grad } B^h$ drift is in the $-\theta$ direction and does not lead to the beam expansion observed with the linear wiggler.

The linear wiggler drift described here imposes additional constraints on the parameters of an FEL experiment. Obviously, the beam radius must be kept as small as possible

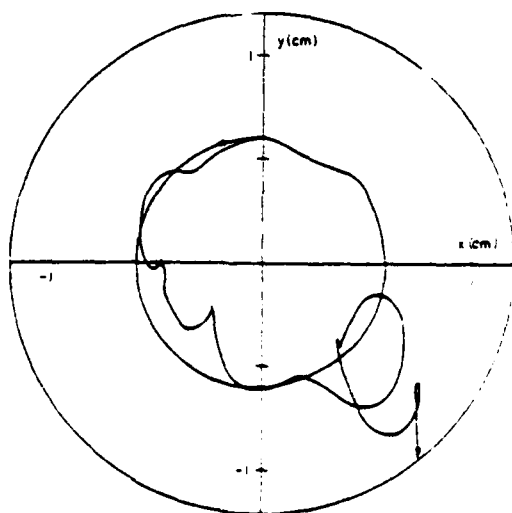


FIG. 5. Electron trajectories in linear wiggler with $P_{d0} = 0$, $I = 1.75$ kA, $\gamma = 2.2$, $B_0 = 2$ kG, $B_w = 1$ kG, $r_0 = 0.6$ cm.

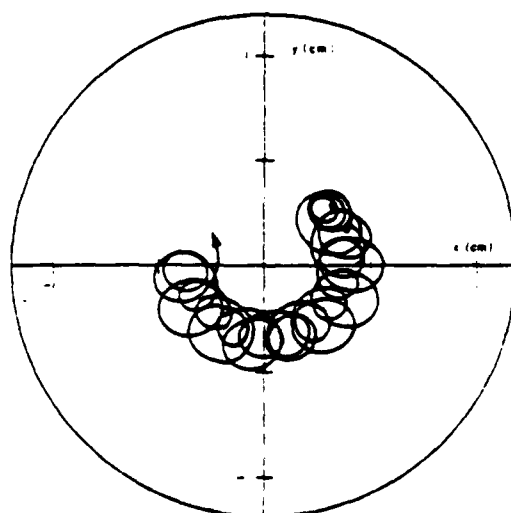


FIG. 6. Electron trajectories with helical wiggler and $\gamma = 2.2$, $B_0 = 2$ kG, $B_w = 1$ kG, $\lambda_w = 3$ cm, $I = 250$ A, $r_0 = 0.4$ cm, and $v_{d0} = 0$.

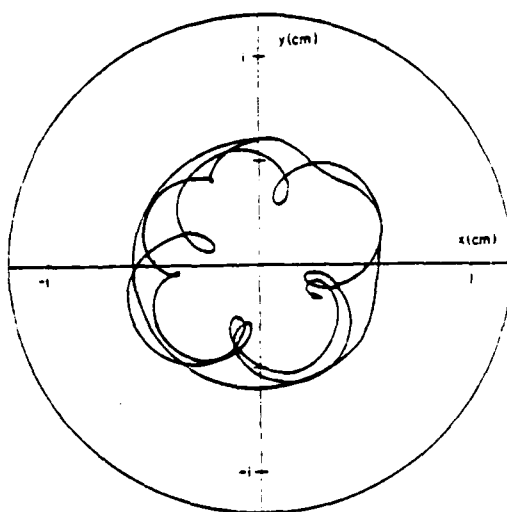


FIG. 7. Electron trajectories in helical wiggler with $P_{\text{e0}} = 0$, $I = 1.75$ kA, $\gamma = 2.2$, $B_0 = 2$ kG, $B_z = 1$ kG, and $r_0 = 0.6$ cm.

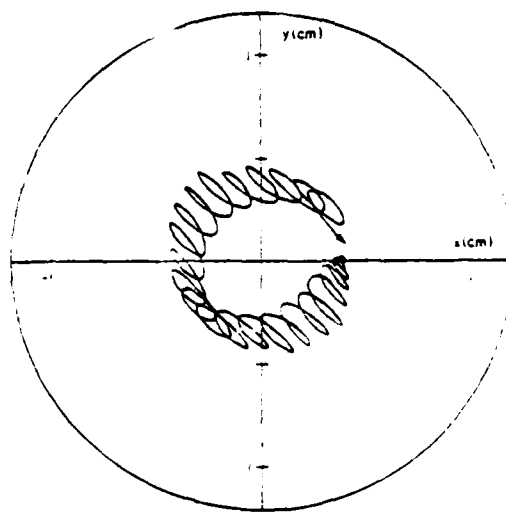


FIG. 8. Electron trajectories in symmetrized linear wiggler with $I = 0$, $\gamma = 2.2$, $B_0 = 2$ kG, $B_z = 1$ kG, $r_0 = 0.4$ cm, and $v_{\text{e0}} = 0$.

to minimize particle loss from the edge of the beam. Preliminary experimental results by our group with a field immersed, apertured source indicate that particle losses can be kept acceptably small in this way. Also, if γ is large enough that $B_z \gg B_0 \gg B_w$ can be satisfied for relatively large B_w , then the drift can be kept small while achieving acceptably large v_w .

Finally, it should be noted that the drift arises from the asymmetry of the linear wiggler and the corresponding absence of focusing forces in the direction perpendicular to the wiggler field. Therefore, it should be possible to stabilize the drift by imposing an additional focusing force in that direction. For example, preliminary results indicate that electron propagation through a "square" or symmetrized linear wiggler is very stable. Such a wiggler has an additional component $B_z' = \cosh ky \cos kz$ and a corresponding addition to B_z' of $-B_w \sinh ky \sin kz$. An electron trajectory through such a wiggler is shown in Fig. 8.

In conclusion, a gradient drift has been shown to exist for a linear wiggler in an axial guide field. The drift can be substantial with small or large beam current in some parameter ranges for a wide range of initial conditions. However, the advantages of a linear wiggler are sufficient in many cases to either limit operation to a "stable" parameter regime or to impose additional focusing forces to stabilize the drift.

ACKNOWLEDGMENT

The authors gratefully acknowledge useful discussions with C. A. Kapetanakis, H. Freund, and C. M. Tang.

- ¹L. R. Elias, W. M. Fairbank, J. M. J. Madey, H. A. Schwettman, and T. I. Smith, *Phys. Rev. Lett.* **36**, 717 (1967).
- ²D. A. G. Deacon, L. R. Elias, J. M. J. Madey, G. J. Ramian, H. A. Schwettman, and T. I. Smith, *Phys. Rev. Lett.* **38**, 892 (1977).
- ³D. B. McDermott, T. C. Marshall, S. P. Schlesinger, R. K. Parker, and V. L. Granatstein, *Phys. Rev. Lett.* **41**, 1368 (1978).
- ⁴R. K. Parker, R. H. Jackson, S. H. Gold, H. P. Freund, V. L. Granatstein, P. C. Efthimion, M. Herndon, and A. K. Kinkad, *Phys. Rev. Lett.* **48**, 238 (1982).
- ⁵H. Boehmer, M. A. Caponi, J. Edighoffer, S. Fornace, J. Munch, G. R. Neil, B. Saur, and C. Shih, *Phys. Rev. Lett.* **48**, 141 (1982).
- ⁶B. M. Kincaid, *J. Appl. Phys.* **48**, 2684 (1977).
- ⁷J. P. Blewett and R. Chasman, *J. Appl. Phys.* **48**, 2692 (1977).
- ⁸K. Halbach, *IEEE Trans. Nucl. Sci.* **NS-28**, 3136 (1981).
- ⁹C. W. Roberson, J. A. Pasour, F. Mako, R. Lucey, and P. Sprangle, Proceedings of the 6th International Conference on Infrared and Millimeter Waves, Miami Beach (1981) to be published in *Int. J. IR and MM Waves*.
- ¹⁰R. M. Phillips, *IRE Trans. Electron Devices* **ED-7**, 231 (1960).
- ¹¹K. D. Jacobs, R. E. Shefer, and G. Bekefi, *Appl. Phys. Lett.* **37**, 583 (1980).
- ¹²N. M. Kroll, P. L. Morton, and M. N. Rosenbluth, "Variable Parameter Free Electron Laser," in *Free Electron Generators of Coherent Radiation*, Physics of Quantum Electronics, Vol. 7, edited by S. F. Jacobs, J. S. Pillof, M. Sargent III, M. O. Scully, and R. Spitzer (Addison-Wesley, Reading, Mass., 1980).
- ¹³L. Friedland, *Phys. Fluids* **23**, 2376 (1981).
- ¹⁴H. P. Freund and A. Drobot, *Phys. Rev. A* **24**, 1965 (1981).
- ¹⁵R. E. Shefer and G. Bekefi, *Bull. Am. Phys. Soc.* **26**, 364 (1981).
- ¹⁶M. Resser, *Phys. Fluids* **20**, 477 (1977).
- ¹⁷V. K. Neil, JASON Tech. Report JSR-79-10, SRI International, Arlington, VA (1979) (unpublished).

A Broadband High Power Millimeter to
Centimeter Spectrometer

F. Mako, J. A. Pasour, C. W. Roberson and R. Lucey

NRL Memorandum Report 4945
August 8, 1983

SECURITY CLASSIFICATION OF THIS PAGE (When Data Entered)

REPORT DOCUMENTATION PAGE		READ INSTRUCTIONS BEFORE COMPLETING FORM
1. REPORT NUMBER	2. GOVT ACCESSION NO.	3. RECIPIENT'S CATALOG NUMBER
NRL Memorandum Report 4945		
4. TITLE (and Subtitle)		5. TYPE OF REPORT & PERIOD COVERED
A BROADBAND HIGH POWER MILLIMETER TO CENTIMETER SPECTROMETER		Interim report on a continuing NRL problem.
		6. PERFORMING ORG. REPORT NUMBER
7. AUTHOR(s)		8. CONTRACT OR GRANT NUMBER(s)
F. Mako,* J.A. Pasour, C.W. Roberson,** and R. Lucey†		
9. PERFORMING ORGANIZATION NAME AND ADDRESS		10. PROGRAM ELEMENT PROJECT, TASK AREA & WORK UNIT NUMBERS
Naval Research Laboratory Washington, DC 20375		61153N: RR011-09-41; 47-1484-0-3
11. CONTROLLING OFFICE NAME AND ADDRESS		12. REPORT DATE
Office of Naval Research Arlington, VA 22217		August 8, 1983
		13. NUMBER OF PAGES
		22
14. MONITORING AGENCY NAME & ADDRESS (if different from Controlling Office)		15. SECURITY CLASS. (of this report)
		UNCLASSIFIED
		15a. DECLASSIFICATION/DOWNGRADING SCHEDULE
16. DISTRIBUTION STATEMENT (of this Report)		
Approved for public release; distribution unlimited.		
17. DISTRIBUTION STATEMENT (of the abstract entered in Block 20, if different from Report)		
18. SUPPLEMENTARY NOTES		
*Present address: JAYCOR, Inc., Alexandria, VA 22304 **Present address: Office of Naval Research, Arlington, VA 22217 †Present address: Pulse Sciences, Inc., San Leandro, CA 94577		
19. KEY WORDS (Continue on reverse side if necessary and identify by block number)		
Spectrometer High power microwaves Gas breakdown		
20. ABSTRACT (Continue on reverse side if necessary and identify by block number)		
A simple spectrometer is described for measuring directly both a high electric field (0.1- 100 kV/cm) and wavelength over a broadband (0.1- 10 cm). The combination of interference and gas breakdown are utilized in measuring the electric field and wavelength. Electron diffusion and the characteristic breakdown relation limit resolution of sub-millimeter wavelengths by requiring very high electric fields (>100 kV/cm).		

DD FORM 1473
1 JAN 73

EDITION OF 1 NOV 65 IS OBSOLETE
S/N 3102-014-6601

SECURITY CLASSIFICATION OF THIS PAGE (When Data Entered)

CONTENTS

I. INTRODUCTION.....	1
II. SPECTROMETER DESIGN.....	1
III. EXPERIMENTAL RESULTS.....	2
IV. LIMITATIONS.....	6
V. CONCLUSION.....	12
REFERENCES.....	20

A BROADBAND HIGH POWER MILLIMETER TO CENTIMETER SPECTROMETER

I. INTRODUCTION

Over the last several years there has been considerable interest in generating high power microwaves from relativistic electron beams.¹ One of the most important parameters to be determined in such experiments is the power spectrum. Interferometers have been used for spectral measurements,² but they are only useful over a very narrow band of frequencies. An improved bandwidth is obtained with a grating spectrometer³ but noise and expense then become issues. Dispersive lines have also been used but they are impractical for long pulses (> 1 ns). Also, all of the above mentioned devices must be calibrated for absolute power. In the beginning of a microwave experiment quick but less precise information about the entire power spectrum are of primary importance. To fit this purpose, we have developed a simple and inexpensive spectrometer which is insensitive to noise and can directly measure selected wavelengths at full power.

II. SPECTROMETER DESIGN

Figure 1 shows a schematic of the spectrometer. Radiation is collected in the horn on the left. It then travels through a high pass filter and expands through the horn on the right to a collimating or weakly focusing lens. The microwaves are reflected from a metallic boundary which is located inside the gas filled chamber. Gas breakdown occurs at the spatially periodic peaks in the electric field which result from interference between the reflected and

Manuscript approved May 23, 1983.

incident waves. Gas breakdown occurs at about half wavelength intervals apart. The wavelength is related to the spot spacing d and the angle of incidence α_i (see Fig. 1) by

$$\lambda = 2 d \cos \alpha_i. \quad (1)$$

Thus, by measuring from a photograph of the breakdown region the spot spacing and diameter, and knowing the gas pressure, then the electric field, power and wavelength can be determined. A relationship between breakdown electric field and gas pressure will be given later. It should be noted that the chamber length does not determine the wavelength since the radiation is reflected from only one highly reflecting boundary. For low power microwaves the focusing lens increases the electric field to facilitate gas breakdown.

The aluminum horns are conical with an inside diameter that is reduced from 12.5 cm to 5 cm. An aluminum taper matches the end of the horns to the high pass filter. Focusing is accomplished with one of three lucite lenses having focal lengths of 12, 24, and 48 cm. Focusing inside and outside the chamber end plate has been tried; however, the clearest interference patterns are observed when focusing is outside the 30 cm long, 14 cm i.d. lucite chamber.

III. EXPERIMENTAL RESULTS

In the present experiment microwaves are generated when a 130 A, 550 keV, 2 μ s long electron beam is passed through a "wiggler" magnetic field. The

wiggler field is produced from the eddy currents induced in a set of spatially periodic conducting rings when an axial magnetic field is pulsed. In this particular case the rings are made of aluminum and have an inside diameter of 7.5 cm, a radial thickness of 0.6 cm and an axial extent of 1 cm. The ring period is 6 cm and the composite ring structure and axial guide field are 200 cm long.

Figure 2 is a time integrated photograph of the resulting interference pattern. Microwave radiation has entered from the left of the photograph, where the lens is located (but cannot be seen), and is reflected off a copper plate located at the right of the photograph (arrow indicates copper plate). The white spots are due to light produced from the gas breakdown. Type 57 (ASA 3000) Polaroid film was used with a Graphflex camera ($f/4.5$) to obtain these results. The gas density was selected experimentally so that enough light was available to be recorded photographically but not high enough to allow microwave reflections from the plasma.

From Fig. 2 the spot spacing is measured to be 2.25 cm which corresponds to a frequency of 6.67 GHz. The breakdown electric field E_b is estimated from the semi-empirical formula

$$E_b = AP\{1 + (a/P\lambda)^2\}^{1/2}, \quad (2)$$

where $A = 3000 \text{ Vm}^{-1}\text{Torr}^{-1}$ and $a = 0.9 \text{ Torr-m}$ for air or nitrogen, P is the gas pressure in Torr, and λ is the wavelength in meters.

Equation (2) has been derived semi-empirically from McDonald's precision

data⁴ and agrees in the worst case to within 30%. This formula is valid on the high pressure side of the breakdown curve, i.e. for $P\lambda > 0.26$ Torr-meters, pulse lengths > 1 μ s, low repetition rate (< 100 pps), and for no electron collisions with the chamber walls. For the results of Fig. 2 the measured pressure is 25 Torr and the wavelength is 4.5 cm, corresponding to an electric field of about 1 kV/cm. From the spot diameter of 2.5 cm the power is estimated, for a plane wave, to be 8 kW.

Wavelength discrimination is accomplished by utilizing the pressure and wavelength dependence of Eq. 2. That is, at a given pressure a shorter wavelength will require a higher electric field in order to achieve breakdown. As stated before, Eq. 2 is valid for $P\lambda > 0.26$ Torr-meter. In the other limit, i.e., for $P\lambda < 0.26$, it will be shown later that short wavelengths cannot be resolved as a result of diffusion.

Discrimination is not possible for all wavelengths in certain electric field versus wavelength distributions. If any two spectral lines in a discrete distribution satisfy the relation

$$\Delta E = E_1 \left\{ 1 - \left[1 + \left(\frac{Aa}{\lambda_1 E_1} \right)^2 \alpha \frac{(2-\alpha)}{(1-\alpha)^2} \right]^{1/2} \right\}, \quad (3)$$

then discrimination is not possible. In Eq. (3), $\Delta\lambda = \lambda_1 - \lambda_2$, $\lambda_1 > \lambda_2$,

$\Delta E = E_1 - E_2$, $E_1 < E_2$ and $\alpha = \Delta\lambda/\lambda_1$, where $E_{1,2}$ is the electric field for wavelength $\lambda_{1,2}$. Eq. 3 simply states that the two spectral lines satisfy Eq. 2 at the same pressure. Even if Eq. (3) is satisfied there is a way to

circumvent this difficulty, provided the wavelengths are sufficiently separated. In such a case, a high pass filter can be used to eliminate the longer wavelength.

There are two more points to consider regarding Eq. 3. If ΔE is greater than the right hand side of Eq. 3 then the pressure can be adjusted so that E_2 is not large enough to breakdown the gas. However, if ΔE is less than the right hand side of Eq. 3 then the pressure can be adjusted to prevent breakdown by E_1 . To resolve every wavelength in a continuous distribution $E(\lambda)$, it follows from Eq. 3 that

$$\frac{dE}{d\lambda} > - \frac{(aA)^2}{\lambda^3 E_b} \quad (4)$$

for every λ .

In order to verify that the observed breakdown pattern is due to an interference effect, the boundary conditions on the incident wave are changed with the results shown in Fig. 3. In each case microwaves are focused by a lens located at the left of the photograph to a region in front of the boundary at the right. By comparing Figs. 3a and 3b, it is clear that the total electric field has increased by increasing the surface reflectivity. In Fig. 3a the boundary is composed primarily of graphite whereas in Fig. 3b the material is lucite (index = 1.63). It should be noted that the thickness of the lucite was selected not to satisfy the resonant reflection condition. In Fig. 3c an absorbing surface is used to eliminate the reflected wave. The interference pattern is absent but a single region of breakdown remains.

This residual breakdown region results from the method used to absorb the radiation. The absorber was constructed from Eccosorb (Emmerson and Cuming, Inc.) in the shape of a "V" and oriented so that microwaves enter the opening of the "V". This technique results in substantial reduction of the reflected wave. The gas breakdown now occurs within the "V" shaped absorber region.

IV. LIMITATIONS

There are several limitations which are inherent in the above type of spectrometer. Practical considerations limit both the wavelength and the electric field strength that can be measured. Long wavelength (>10 cm) operation is impractical while trying to maintain the geometrical optics condition. Short wavelengths (<1 mm) are bounded by the ability to resolve the spot spacing. Resolution is maximized by operating with a highly reflective chamber end plate and a high gas pressure, which limits electron diffusion. High pressures, however, require very high electric fields (> 100 kV/cm) for submillimeter resolution. At low electric fields (< 100 V/cm) a limit is set by the ability of the electrons to gain sufficient energy to breakdown the gas.

In order to make the wavelength measurements two conditions must be satisfied: the breakdown region must be visible and the wavelength must be resolvable. The dashed curve in Fig. 4 shows the total RMS electric field of the standing wave divided by the peak incident electric field. When the

breakdown electric field is above the peak total RMS electric field (top line in Fig. 4), the gas does not breakdown. Also wavelength resolution is not possible if the breakdown electric field is below the minimum total RMS electric field (as in the bottom line), since breakdown occurs everywhere. Resolution is maximized when the breakdown field (solid line in Fig. 4) is just slightly below the peak total RMS electric field, so that the length of the breakdown region is considerably smaller than the wavelength. The length of the breakdown region can be determined from the total RMS electric field for two plane waves traveling in opposite directions,

$$E_{rms} = \{E_i^2/2 + E_r^2/2 - E_i E_r \cos(2kx)\}^{1/2}, \quad (5)$$

where E_i and E_r are the incident and reflected electric field amplitudes for a plane polarized wave incident normally on a partially reflecting surface located at $X = 0$, and $k = 2\pi/\lambda$ is the wavenumber. From Eq. 5 the length of the breakdown region is given by

$$L_b = \lambda/2 \left\{ 1 - \frac{1}{\pi} \cos^{-1} \left(\frac{E_i^2 + E_r^2 - 2E_b^2}{2E_i E_r} \right) \right\}, \quad (6)$$

where $E_i - E_r < 2 E_b < E_i + E_r$ for resolvable breakdown. An important observation here is that for a poorly reflecting boundary, the minimum E_{rms} approaches the maximum E_{rms} and breakdown will occur nearly everywhere or not at all, and again a wavelength measurement cannot be made. Figure 5 is a plot of the ratio of the total RMS electric field to the peak incident electric

field versus position for three different values of E_r/E_i . It is clear that a highly reflecting boundary is desirable for wavelength resolution. It should be mentioned that a shallow focusing angle is necessary in order to keep the reflected wave amplitude comparable to the incident amplitude. This accounts for the fact that clearer interference patterns were observed when the radiation was focused beyond the end plate.

So far, only the initial breakdown region has been considered. However, electron diffusion will increase the length of this initial region, and hence further restrict the ability to resolve a given wavelength. Diffusion contributes a length given by

$$x_d = (Dt)^{1/2}, \quad (7)$$

where D is the diffusion coefficient and t is the time. In order to relate the diffusion length to properties of the gas and the electrons, the diffusion coefficient must be evaluated. From elementary kinetic theory the diffusion coefficient for a Maxwellian distribution of electrons can be shown to be in MKS units

$$D = 2eU/(3mf_c), \quad (8)$$

where m is the electron mass, eU is the mean electron energy (U is in eV), and f_c is the electron-neutral collision frequency. From Reference 4, a simple

relation is available that connects the collision frequency to the pressure and is given by,

$$f_c = bP, \quad (9)$$

where $b = 5.3 \times 10^9/\text{sec-Torr}$ for air or nitrogen. Also, from Reference 4 the measured electron energy is typically a couple of eV. When Eqs. (7)-(9) are combined it becomes clear that for long pulses and short wavelengths a high pressure is required in order to achieve wavelength resolution. Higher pressures will then require high electric fields to obtain gas breakdown.

Figure 6 demonstrates the combined effects of diffusion and breakdown field, on wavelength resolution. In Fig. 6a the image is cloudy which makes a wavelength determination dubious. By raising the pressure (from 2 to 20 torr) the image becomes clear as shown in Fig. 6b. A lucite wall was used as a reflector in Fig. 6a and 6b. At 20 torr the one dimensional diffusion length is from Eq. (7) equal to 0.26 cm. Since diffusion occurs in both directions from the center of the breakdown, the calculated spot thickness will be twice the one dimensional diffusion length, namely 0.52 cm. The measured spot thickness (Fig. 6b) is 0.5 cm which is in very good agreement with the calculated value. At 2 torr the two directional diffusion length is 1.6 cm which accounts for smearing of discrete spots. However, there may be an additional effect which clouds the image of Fig. 6a. Plasma motion has been observed when the electric field is substantially above the breakdown electric field.⁵ The conditions for Fig. 6a are such that the electric field is three

times the breakdown field which is sufficient for plasma motion to occur, and since this is a time integrated photograph plasma motion could account for some of the image clouding.

In general, the breakdown field versus pressure exhibits a minimum. This fact combined with diffusion imposes a limit on the minimum resolvable wavelength. This electric field minimum corresponds to a maximum transfer of energy to the electrons from the electromagnetic field, which occurs when the time between collisions is some fraction of half the wave period. That is

$$1/f_c = T/(2i), \quad (10)$$

where T is the wave period and i is a number that depends on the electron-neutral scattering angle. For a 180° angle, $i = 1$; for smaller angles, i becomes larger than 1. For electrons with a low energy (< 5 eV) the scattering angle is large, thus i will be of order 1. By combining Eqs. (9) and (10) a relation for the pressure at the minimum breakdown field can be obtained. When this is done and the results are compared with the data of Reference 4, then $i = 1.86$ is obtained for air.

At the minimum breakdown field the shortest resolvable wavelength can now be calculated. By setting $x_d = \lambda/4$ in Eq. (7) and solving Eqs. (7), (8), and (10) for the wavelength, the shortest resolvable wavelength is found to be

$$\lambda_s = 16 eUt/(3 \text{ mic}), \quad (11)$$

where c is the speed of light. This result represents a rather fundamental relationship for any gas and only a knowledge of the mean electron energy and scattering angle constant is required. But since the mean electron energy for any gas is less than 5 eV, the scattering angle will be large and i will be of order 1. For the present experiment, $t = 2 \mu s$, $i = 1.86$, and $U = 1.5$ eV, so that $\lambda_s = 0.5$ cm.

If it is desirable to resolve shorter wavelengths, then shorter pulses and/or higher electric fields could be used as shown in Fig. 7. The dotted curve is a plot of the diffusion relation (Eq. 7) with $x_d = \lambda/4$, $U = 1.5$ eV, and $t = 2 \mu s$. The solid lines are plots of the higher pressure side of the breakdown curve (Eq. 2) for air at different electric field strengths. Since $x_d < \lambda/4$ is required for resolution when diffusion is considered, only wavelengths above the diffusion curve can be resolved. Also, for a particular electric field, λ must lie on the breakdown curve in order for the gas to breakdown only at the standing wave peaks. Thus, the minimum resolvable wavelength at any particular field is given by the intersection of the breakdown and diffusion curves. When the curves do not intersect, diffusion is not a limiting factor and the minimum wavelength is just determined by the field strength. It should be noted that very large electric fields are required as one approaches submillimeter wavelengths.

An expression for the minimum resolvable wavelength in air versus electric field can be found by eliminating the pressure in Eq. (2), (7), (8) and (9) and is given by

$$\lambda^2 = \frac{1}{2E_b^2} \left\{ (aA)^2 + \left[(aA)^4 + \left(\frac{64eUtAE_b}{3mb} \right)^2 \right]^{1/2} \right\}. \quad (12)$$

For high electric fields, Eq. (12) reduces to

$$\lambda = \left(\frac{32eUtA}{3mbE_b} \right)^{1/2}. \quad (13)$$

This very slow dependence on electric field gives a practical limit to the minimum resolvable wavelength.

In order to use this spectrometer for longer wavelengths a larger chamber and lens would have to be built in order to preserve the geometric optics condition. This then sets a practical limit on the utility of this spectrometer for long wavelengths. Effects from electrons hitting the chamber wall and ion motion occur at such low frequencies that they are not a limiting factor in view of the diffraction condition.

V. CONCLUSION

In summary then, a simple spectrometer has been described which is capable of both high power and broadband wavelength measurement. Wavelength resolution has been shown to depend on the reflectivity of the chamber end plate and electron diffusion. Electron diffusion and the characteristic breakdown curve limits the resolvability of submillimeter wavelengths by requiring very high electric fields (> 100 kV/cm). At high fields, the minimum resolvable wavelength is proportional to the reciprocal square root of the breakdown field. This slow dependence on electric field gives a practical limit to both electric field and submillimeter wavelength measurements.

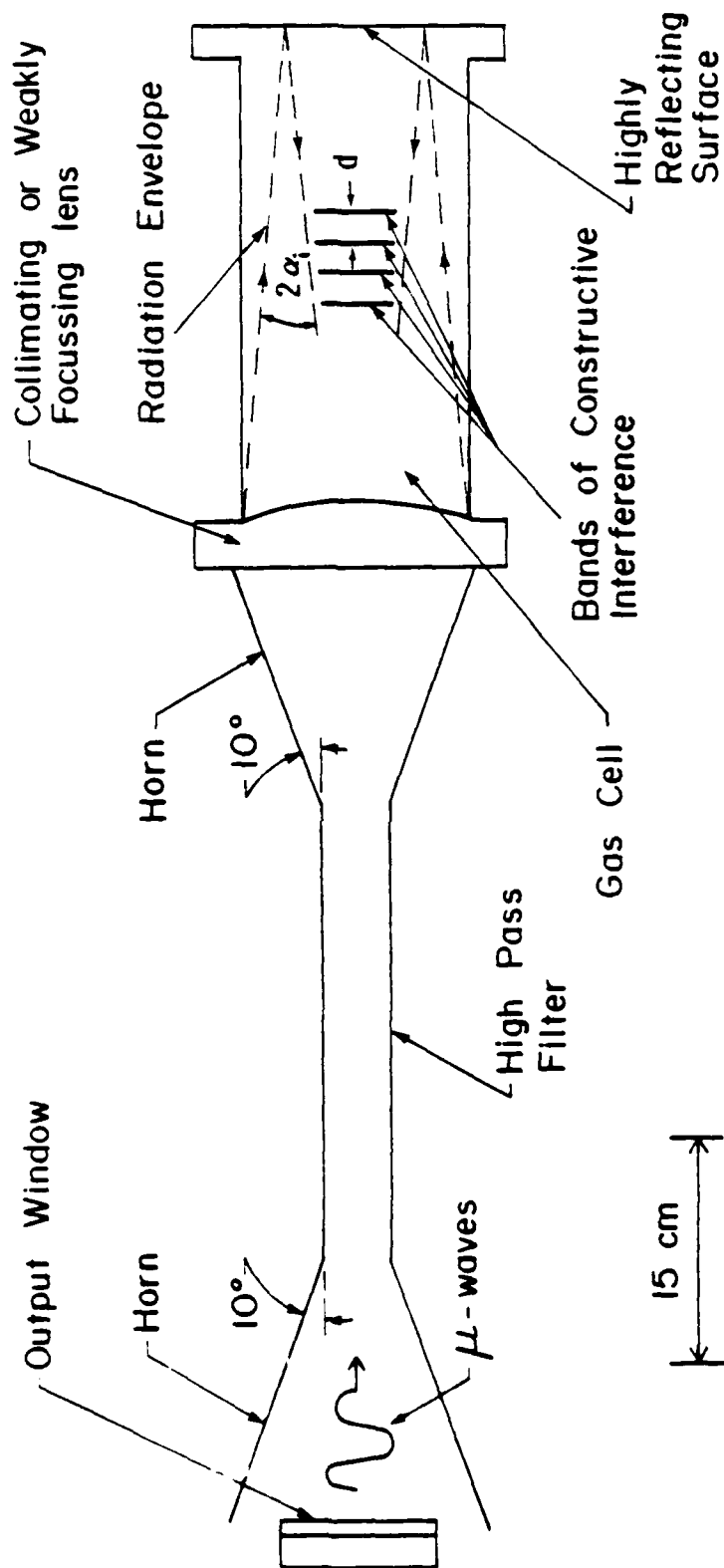
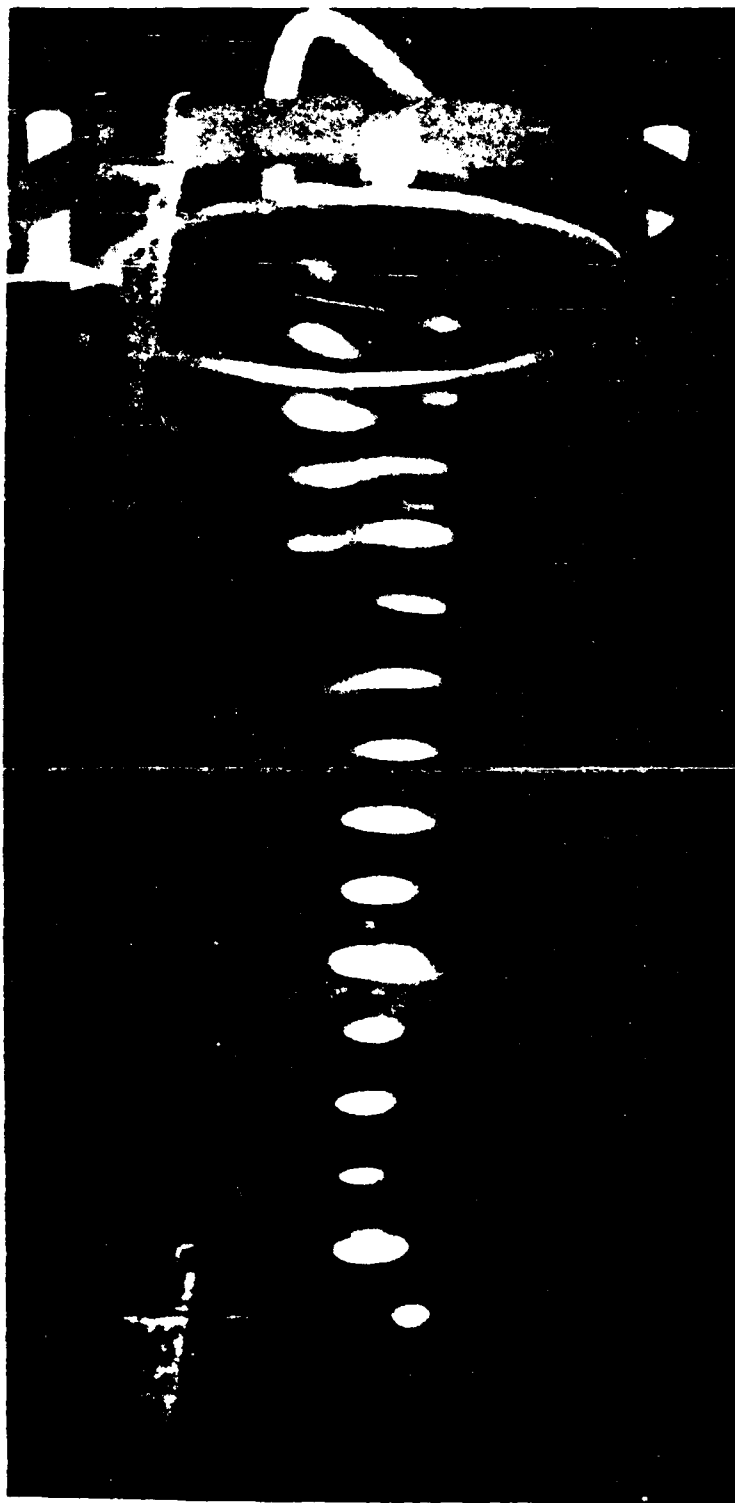
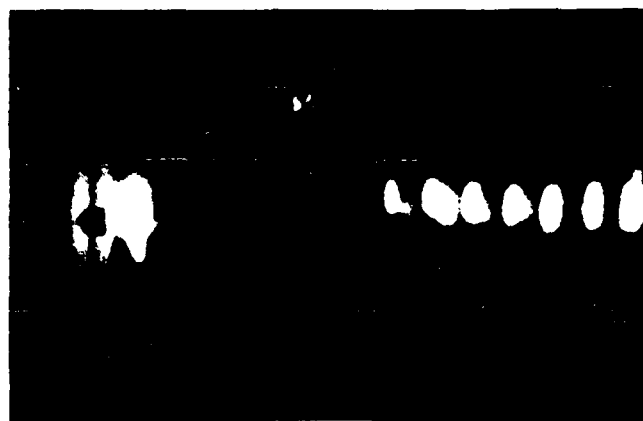


Figure 1. Schematic of the spectrometer.

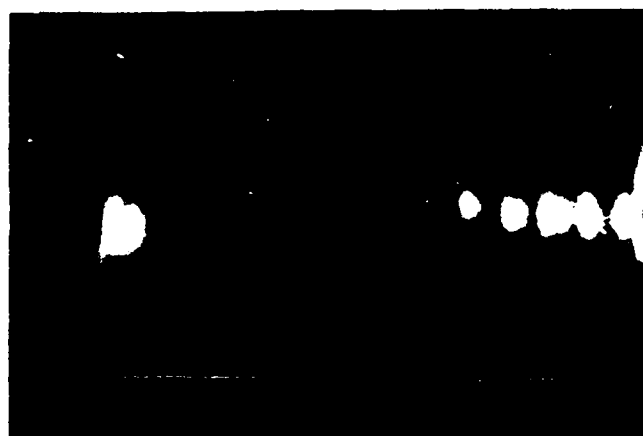


R-897

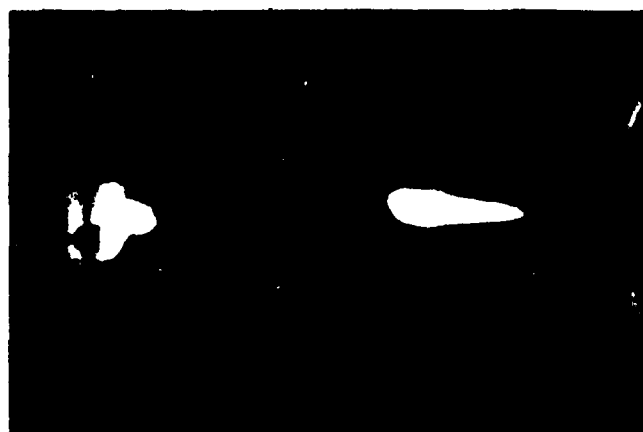
Figure 2. A time integrated photograph of the microwave interference pattern. Bright spots result from breakdown of the gas, in this case nitrogen at 25 Torr. The arrow indicates the location of the copper plate.



a



b



c

R-898

Figure 3. Microwaves entering from the left are focused in front of three different boundaries on the right. a) Highly reflecting boundary. b) Partially reflecting boundary. c) Absorbing boundary. In each case the pressure is 20 Torr.

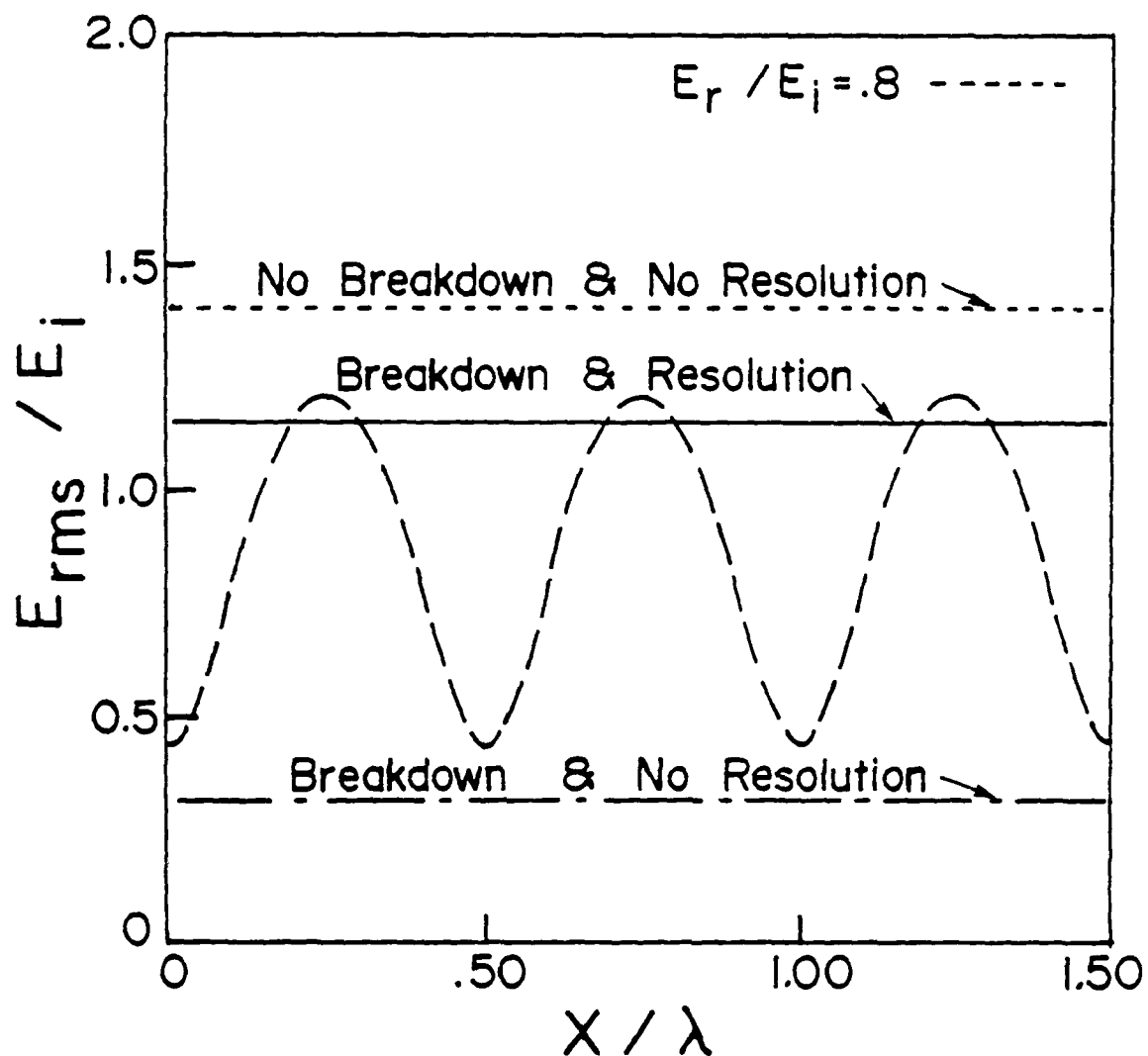


Figure 4. Conditions necessary for wavelength measurement. The dashed curve is the total RMS electric field normalized to the peak incident amplitude. When the required breakdown field is too high (top line) no breakdown occurs. When the breakdown field is too low (bottom line) breakdown occurs everywhere. The correct breakdown is indicated by the solid line. The reflecting surface is located at $X = 0$.

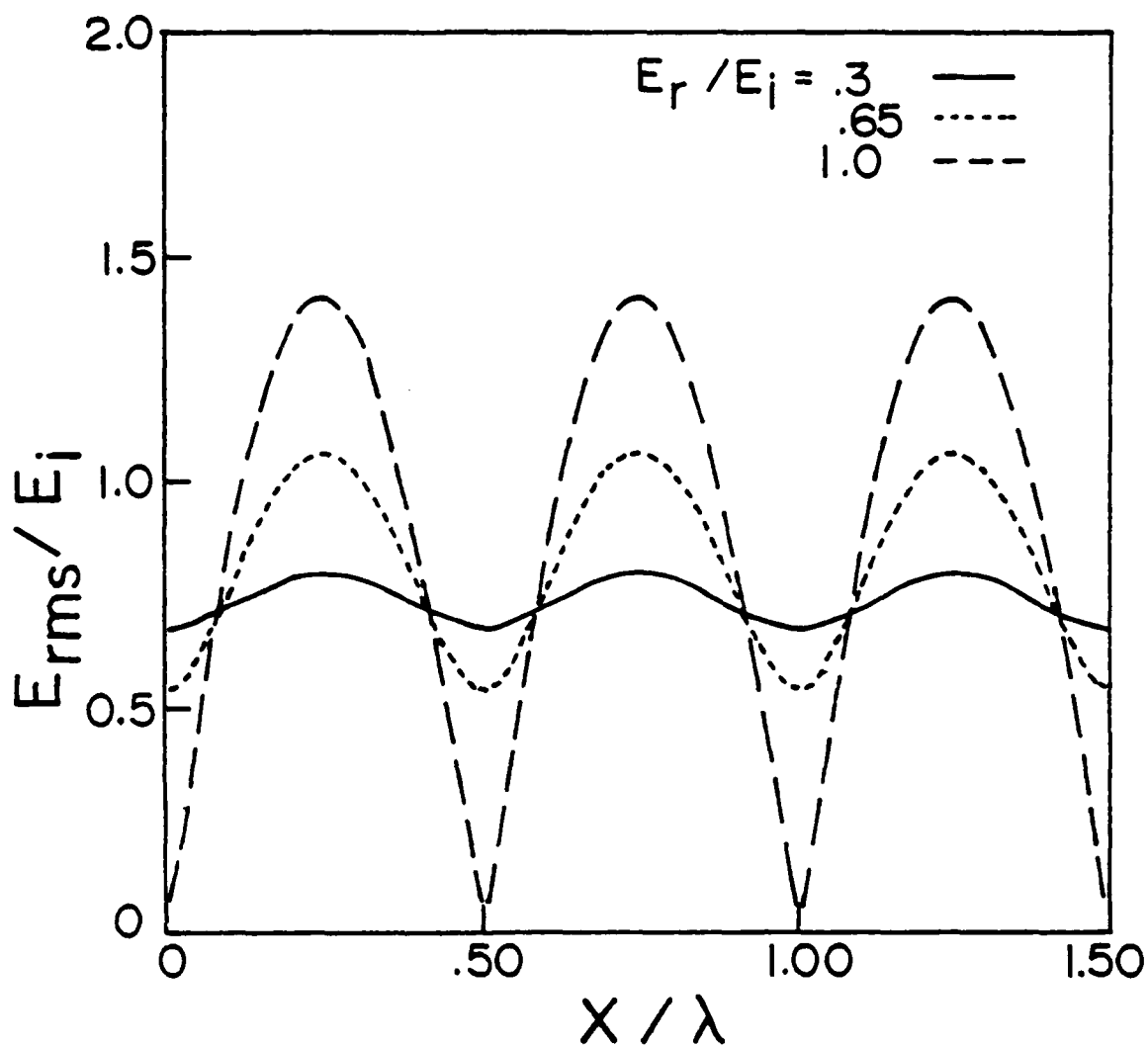
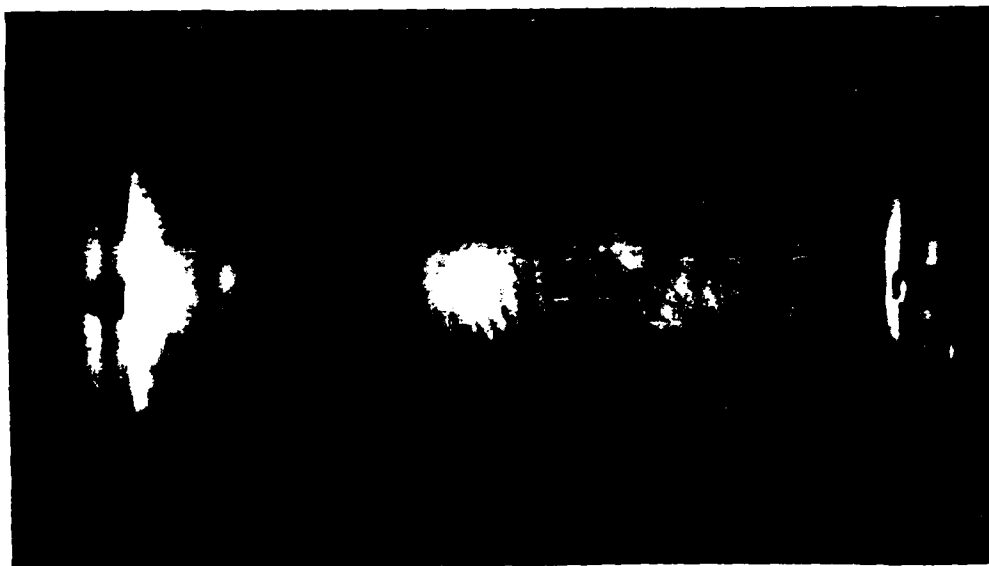
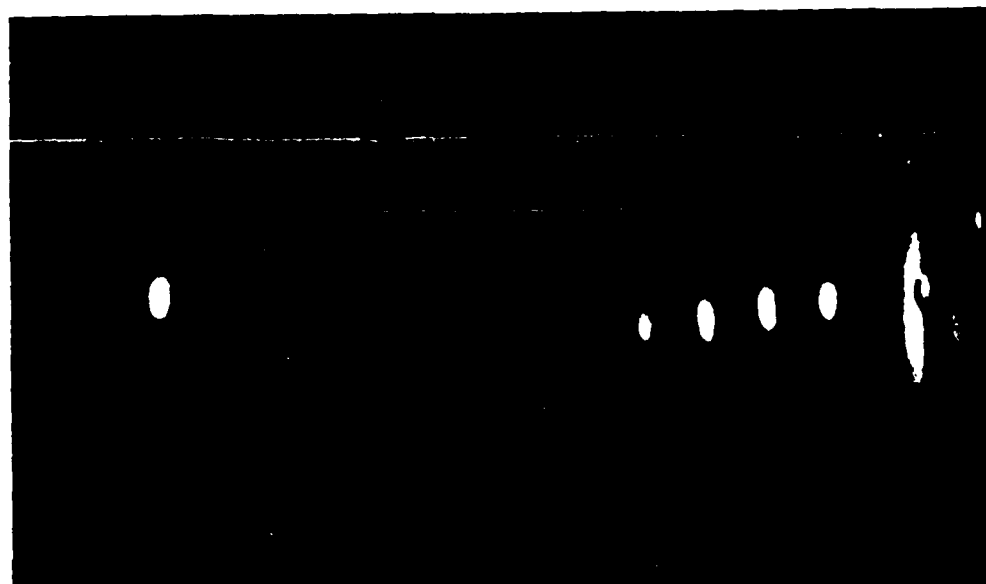


Figure 5. The effect of the boundary reflectivity on the total RMS electric field. Reflected to incident wave amplitude is indicated in the upper right hand corner. Low reflectivity greatly diminishes the ability to select the proper breakdown condition for wavelength measurement.



a



b

R-899

Figure 6. The impact of low reflectivity and diffusion on wavelength resolution. In (a) a wavelength measurement is not possible; however, by increasing the pressure (b) a wavelength measurement is easily established.

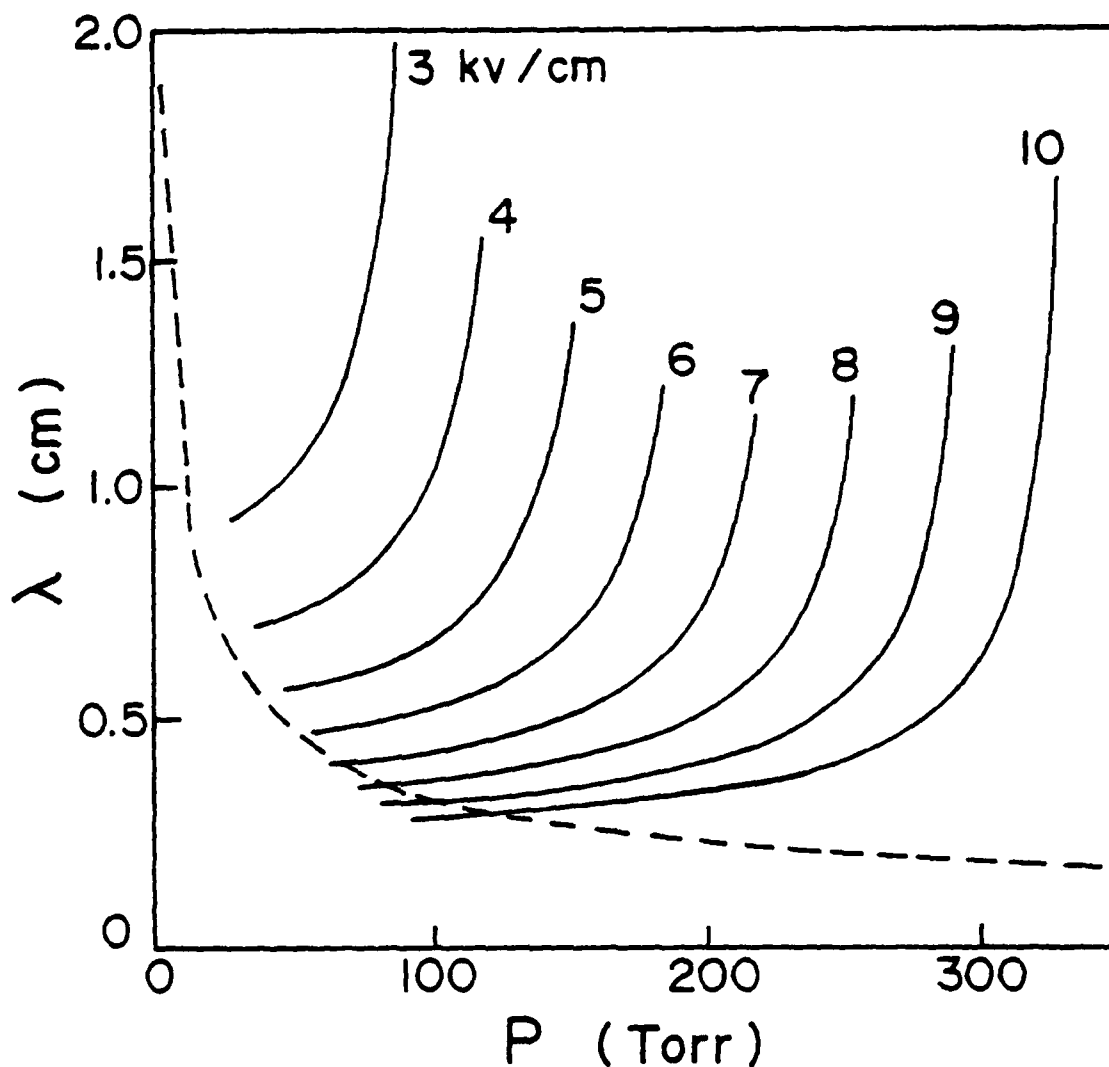


Figure 7. Shortest resolvable wavelength at various electric field strengths. The dotted curve is the diffusion length equated to $\lambda/4$, and the solid curves are the characteristic breakdown curves for different electric field strengths. Minimum resolvable wavelength is given by the intersection of the diffusion and breakdown curves, or simply by the bottom of the breakdown curves when the two curves do not intersect. The curves are for air with a diffusion time of 2 μsec and an electron energy of 1.5 eV.

REFERENCES

1. Infrared and Millimeter Waves, Ed. K.J. Button, Vol. 1, Academic Press (1979).
2. D.B. McDermott, T.C. Marshall, S.P. Schlesinger, R.K. Parker and V.L. Granatstein, Phys. Rev. Lett. 41, 1368 (1978).
3. J.A. Pasour, S.P. Schlesinger, Rev. Sci. Instrum. 48, 1355 (1977).
4. A.D. MacDonald, Microwave Breakdown in Gases, John Wiley & Sons Inc. (1966).
5. W.M. Bollen, C.L. Yee, A.W. Ali, M.J. Nagurney and M.E. Read, J. Appl. Phys. 54 (1), 101 (1983).

Electron Drift in a Linear Magnetic
Wiggler with an Axial Guide Field

J. A. Pasour, C. W. Roberson and F. Mako

NRL Memorandum Report 4791

June 18, 1982

SECURITY CLASSIFICATION OF THIS PAGE (When Data Entered)

REPORT DOCUMENTATION PAGE		READ INSTRUCTIONS BEFORE COMPLETING FORM
1. REPORT NUMBER	2. GOVT ACCESSION NO.	3. RECIPIENT'S CATALOG NUMBER
NRL Memorandum Report 4791		
4. TITLE (and Subtitle)		5. TYPE OF REPORT & PERIOD COVERED
ELECTRON DRIFT IN A LINEAR MAGNETIC WIGGLER WITH AN AXIAL GUIDE FIELD		Interim report on a continuing NRL problem.
		6. PERFORMING ORG. REPORT NUMBER
7. AUTHOR(s)		8. CONTRACT OR GRANT NUMBER(s)
J.A. Pasour, F. Mako*, and C.W. Roberson		
9. PERFORMING ORGANIZATION NAME AND ADDRESS		10. PROGRAM ELEMENT PROJECT TASK AREA & WORK UNIT NUMBERS
Naval Research Laboratory Washington, DC 20375		61153N; RR011-09-41; 47-1484-0-2
11. CONTROLLING OFFICE NAME AND ADDRESS		12. REPORT DATE
		June 18, 1982
		13. NUMBER OF PAGES
		23
14. MONITORING AGENCY NAME & ADDRESS (if different from Controlling Office)		15. SECURITY CLASS. (of this report)
		UNCLASSIFIED
		15a. DECLASSIFICATION/DOWNGRADING SCHEDULE
16. DISTRIBUTION STATEMENT (of this Report)		
Approved for public release; distribution unlimited.		
17. DISTRIBUTION STATEMENT (of the abstract entered in Block 20, if different from Report)		
18. SUPPLEMENTARY NOTES		
*Present address: JAYCOR, Inc., Alexandria, VA		
19. KEY WORDS (Continue on reverse side if necessary and identify by block number)		
Free electron laser Magnetic wiggler		
20. ABSTRACT (Continue on reverse side if necessary and identify by block number)		
<p>Electron trajectories through a linear magnetic wiggler in an axial guide field are calculated numerically. Off-axis electrons are shown to drift in a direction perpendicular to the wiggler field because of the wiggler gradient. Effects of self fields and initial conditions are analyzed, and the results are compared to those obtained with a helical wiggler. An empirical analytic expression for the linear wiggler drift is presented, and means of stabilizing the drift are discussed.</p>		

DD FORM 1473
1 JAN 73EDITION OF 1 NOV 65 IS OBSOLETE
S/N 0102-014-6601

SECURITY CLASSIFICATION OF THIS PAGE (When Data Entered)

ELECTRON DRIFT IN A LINEAR MAGNETIC WIGGLER WITH AN AXIAL GUIDE FIELD

Recently, there has been much interest in free electron lasers (FEL's) which use spatially varying magnetic fields to modulate a relativistic electron beam (REB).¹⁻⁵ Three types of magnetic wigglers have been widely used: helical (usually produced by a bifilar helical current winding^{6,7}), linear (produced by an array of permanent magnets⁸ or by linearly alternating windings⁹), and radial¹⁰ (produced by a series of spaced conducting or ferromagnetic washers¹¹ immersed in an axial field or by a series of alternating coils³). Of these, only the first two produce a perpendicular field on axis and are therefore suitable for use with a small diameter beam of solid cross-section. In this paper, we will analyze the propagation of a solid, high current REB through linear and helical wigglers with a superimposed axial guide field.

FEL experiments fall into two categories depending on the beam current. Compton regime FEL's^{1,2,5} have used high energy (10's of MeV), low current ($\lesssim 1$ A) beams while Raman FEL's^{3,4} have used lower energy (~ 1 MeV), high current ($\gtrsim 1$ kA) beams. Helical wigglers have been used in both current regimes, but until recently⁹ linear wigglers were used only in the Compton regime. In this case, the linear wigglers consist of permanent magnets and there is no guide field. However, for high current beams, a guide field is required to contain the beam. Although there are advantages to a linear wiggler from the standpoint of ease of assembly and versatility (e.g., changing the periodicity or tapering the period and/or field amplitude for efficiency enhancement¹²) we will show that there is no equilibrium for off-axis particles when a beam is propagated through a linear wiggler in an axial field. The particles drift out of the wiggler unless additional focusing forces are provided.

Various authors have considered particular cases of electron motion through magnetic wigglers. These have typically been single particle (low current) calculations. Blewett and Chasman⁷ considered motion of high energy electrons (~ 24 MeV) through a helical wiggler and found stable helical orbits with superimposed betatron oscillations. Friedland¹³ has treated the case of lower energy electrons (~ 300 keV) in an idealized radially uniform helical wiggler with a superimposed axial guide field. He showed that various stable trajectories were possible and derived stability criteria relating the allowed wiggler and guide field strengths to beam energy and wiggler period λ_w . These "stable" regions are given by

$$\frac{B_w}{B_0} < \left[\left(\frac{vk}{\Omega_0} \right)^{2/3} - 1 \right]^{3/2} \quad (2a)$$

and

$$\Omega_0 > ck, \quad (2b)$$

where B_0 is the axial guide field, $\Omega_0 = eB_0/\gamma m$ is the corresponding cyclotron frequency, v is the electron velocity, and $k = 2\pi/\lambda_w$. Physically, these conditions stem from the resonance in the perpendicular velocity of an electron in the wiggler and guide fields:⁴

$$v_w = - \frac{v_z \Omega_0}{v_z k - \Omega_0} \quad (3)$$

Freund and Drobot¹⁴ have considered this case further and also conclude that stable trajectories with nearly constant axial velocities and relatively large

wiggler amplitudes are possible when $\Omega_0 \ll ck$. This is consistent with condition (2a).

The present analysis employs a relatively simple computer code which solves the equations of motion of an electron in any electric and magnetic field configuration using a fourth-order Runge-Kutta method. Self electric and magnetic fields are calculated by assuming that the electron is at the edge of an azimuthally symmetric beam of current I , so that the self fields can be written as (mks)

$$\begin{aligned} E_r &= \frac{-I}{2\pi\epsilon_0 r v_z} \\ B_\theta &= \frac{-\mu_0 I}{2\pi r}, \end{aligned} \quad (4)$$

where $r(t)$ is the electron radius. The axial self fields are neglected.

For the particular cases considered here, the external magnetic field consists of a solenoidal field produced by a 15.3-cm-I.D. x 2-m-long solenoid together with a wiggler that begins in the uniform portion of the solenoidal field. The wiggler field, which may be either helical or linear, rises adiabatically over ten periods and then oscillates with constant amplitude. The envelope enclosing the wiggler amplitude is given by

$$b(z) = \begin{cases} \frac{1}{2} \left[\left(\frac{z}{10\lambda_w} \right)^2 + \left(\frac{z}{10\lambda_w} \right)^3 \right], & 0 \leq z \leq 10 \lambda_w \\ 1, & z > 10 \lambda_w. \end{cases} \quad (5)$$

Here, z is the axial distance from the beginning of the wiggler. This variation closely fits the linear wiggler used in the NRL induction linac FEL. The field on axis from this wiggler is plotted in Fig. 1 along with the envelope equation (5).

The linear wiggler field components are

$$\begin{aligned} B_x^L &= b(z)B_w \cosh kx \cos kz \\ B_y^L &= 0 \\ B_z^L &= -b(z)B_w \sinh kx \sin kz. \end{aligned} \tag{6}$$

where B_w is the peak wiggler field on axis. For the NRL linear wiggler,⁹ which has $\lambda_w = 3$ cm and winding layers spaced by 3.2 cm, these expressions are valid for $r \lesssim 1$ cm.

We will be primarily concerned with relatively low energy (~ 1 MeV), high current (\sim kA) beams. Of particular interest are the effects of self-fields, guide field and wiggler amplitude, and initial beam conditions corresponding to a field-immersed ($v_{\theta 0} = 0$) or a shielded source ($P_{\theta 0} = 0$), where $v_{\theta 0}$ is the initial azimuthal electron velocity and $P_{\theta 0}$ the initial canonical angular momentum. If the axial self magnetic field is neglected, $P_{\theta 0} = 0$ implies $v_g = e r B_z / (2 \gamma m)$ in a uniform field B_z .

First, we consider a beam with $\gamma = 2.2$, $I = 250$ A, $B_0 = 2$ kG, $B_w = 1$ kG, and $\lambda_w = 3$ cm. Note that Eq. (2a) would require $B_w < 3$ kG for stability in this case with a helical wiggler. The x-y trajectories of electrons injected

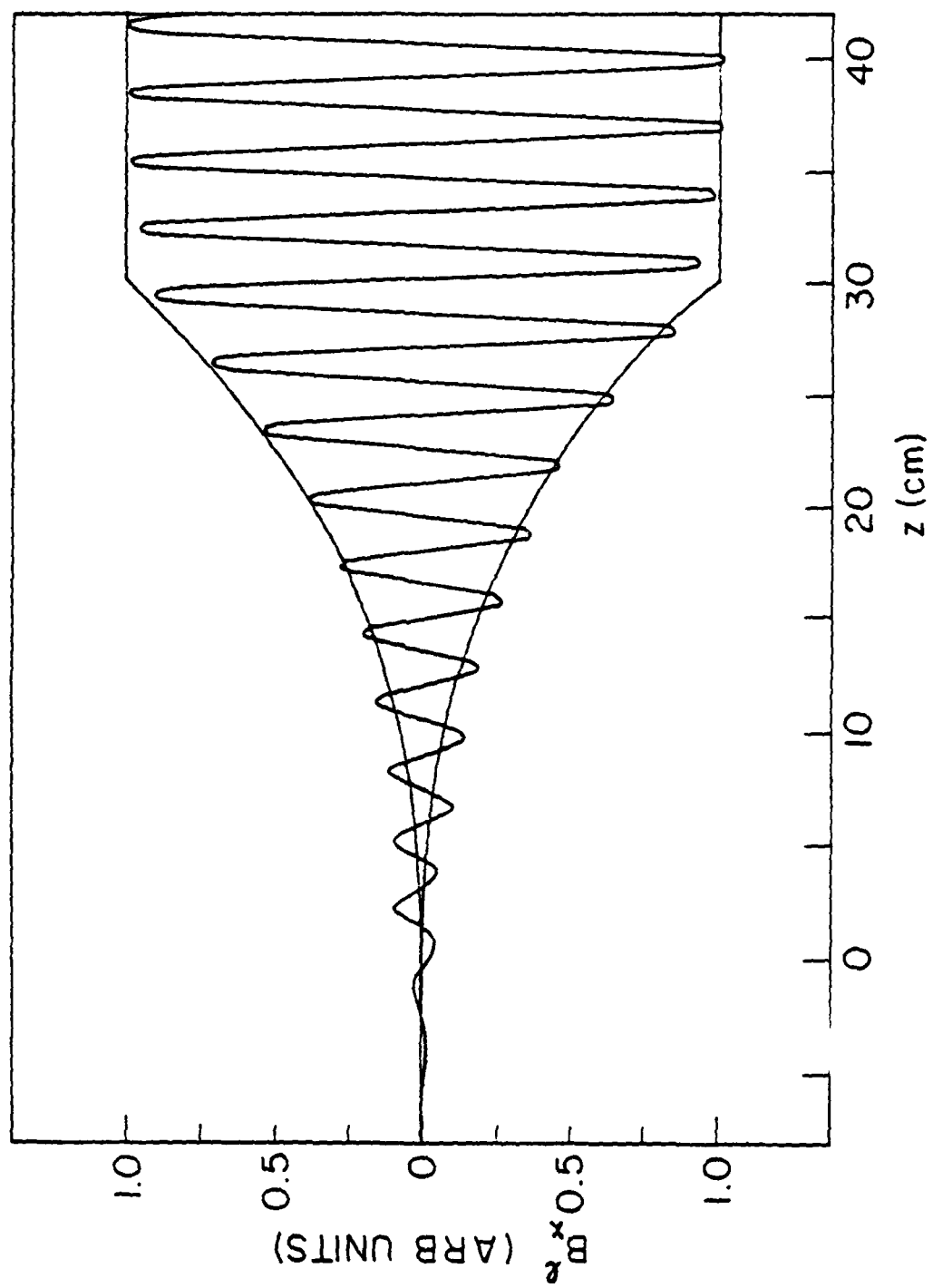


Fig. 1 - Plot of measured $B_x^e(z)$ from NRL linear wiggler together with
envelope $b(z)$ from Eq. (5)

with $v_{10} = 0$ and $r_0 = 0.4$ cm into a linear wiggler are shown in Fig. 2. Each particle initially begins to $\vec{E} \times \vec{B}$ drift in the self fields, but when it reaches a region of large wiggler field it begins drifting in the y-direction. In each case the electron reaches an imaginary wall, located at $r = 1.2$ cm, after only partially traversing the wiggler. It should be noted that the assumptions used to calculate the self fields become invalid as the beam distorts. Consequently, to determine if these self fields are responsible for this drift, the calculations are repeated with $I = 0$ (Fig. 3). A third trajectory is also plotted for $B_w = 0.5$ kG. The electron that originates on the y-axis is well confined, but electrons off the y-axis again drift to the wall, with a velocity much higher for $B_w = 1$ kG ($\langle v_d \rangle = .047$ c) than for $B_w = .5$ kG ($\langle v_d \rangle = .011$ c).

This behavior can be explained by the increasing gradient in the wiggler field, and consequently the emergence of a significant axial field component, as the distance from the y axis increases. Although the present drift arises from the gradient in B_w and is in the direction of $\nabla B_w \times \vec{B}_0$, it is quantitatively different from the usual guiding center approximation because the field variation over one gyroperiod is so extreme. For example, when $kx = .8$ ($x = .4$ cm in the present case), B_z^2 varies from $+B_w$ to $-B_w$ over one period. However, the physical mechanism is the same as for the usual gradient drift; i.e., the gyroradius in the part of the orbit where B_z is a minimum, or where $|x|$ is a minimum in Fig. (3), is larger than where B_z is a maximum. The addition of self fields merely imposes an additional $\vec{E} \times \vec{B}$ rotation on the orbit, so that an electron that originates on the y-axis (and is therefore confined when $I=0$) begins to drift into a region of increasing B_z^2 . Therefore, it actually is "lost" sooner than an electron on the x-axis which

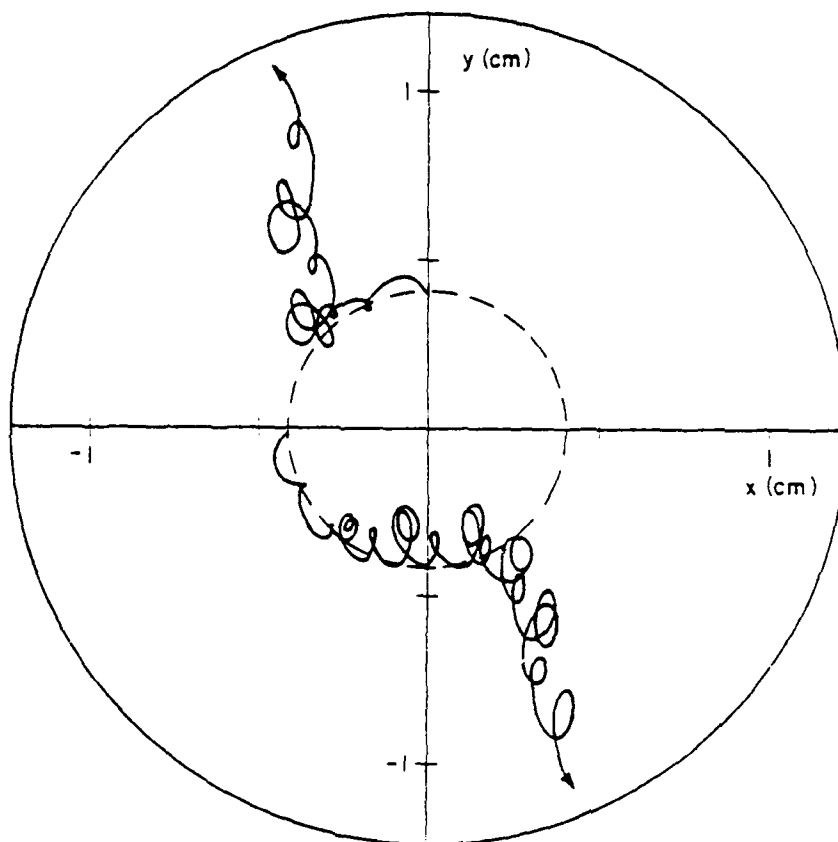


Fig. 2 - Electron trajectories in linear wiggler with $\lambda_w = 3$ cm, $B_0 = 2$ kG, $\gamma = 2.2$, $r_0 = .4$ cm, $I = 250$ A, and $B_w = 1$ kG.

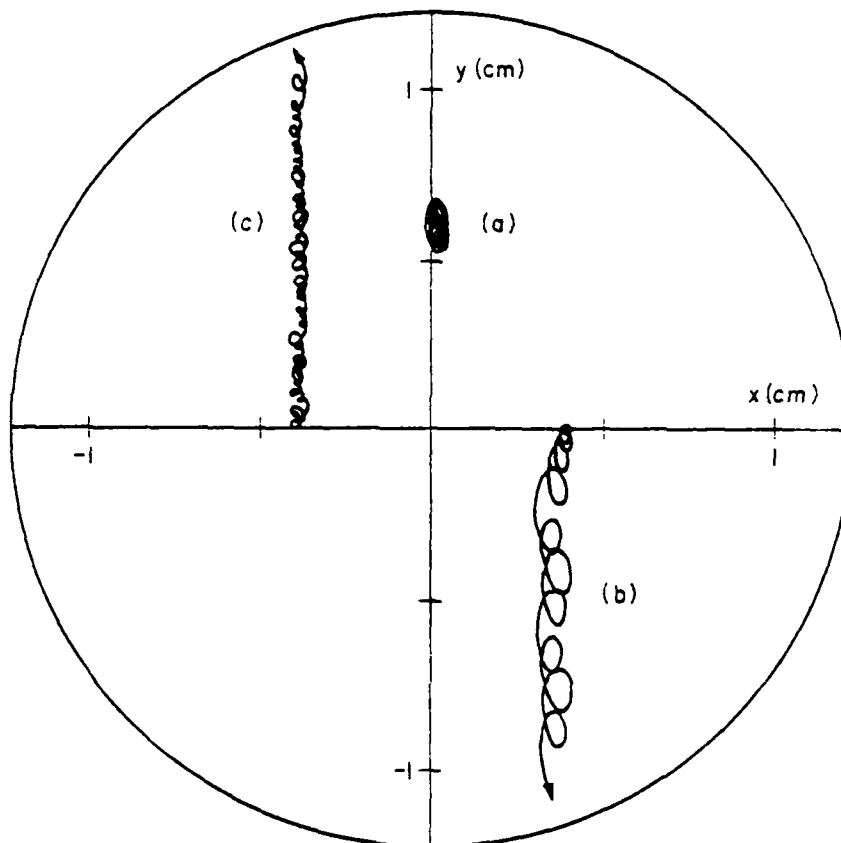


Fig. 3 - Electron trajectories in linear wiggler with $\lambda_w = 3$ cm, $B_0 = 2$ kG, $\gamma = 2.2$, $r_0 = .4$ cm, and $I = 0$. $B_w = 1$ kG for particles a and b, and $B_w = .5$ kG for particle C.

initially $\vec{E} \times \vec{B}$ drifts into a region of smaller B_z^2 .

An approximate, empirical expression for the drift has been found which is in quite good agreement with the code results when $\Omega_w < \Omega_o < kv_z$ (below the cyclotron resonance). In terms of the wiggler gradient, the expression is

$$\vec{v}_d = \frac{1}{2} \frac{v_\perp^2}{\Omega_o} \frac{\nabla(B_z^2)}{2(B_z^2)^2} \times \frac{\vec{B}_o}{B_o}, \quad (7)$$

which has the same form as the usual grad B drift but is quantitatively

different. The single particle equations of motion are $\dot{v}_x = v_y \Omega_z$,

$\dot{v}_y = -v_z \Omega_x + v_x \Omega_z$, and $\dot{v}_z = v_y \Omega_x$. Assuming $v_z = \text{constant}$ and that the gyration velocities are $v_y = v_{ly} \sin kz$ and $v_x = v_{lx} \cos kz$, it follows that

$$v_{ly} = v_z \frac{kv_z \Omega_w \cosh kx}{\Omega_o^2 - k^2 v_z^2} \quad (8)$$

$$v_{lx} = v_z \frac{\Omega_o \Omega_w \cosh kx}{\Omega_o^2 - k^2 v_z^2}$$

for $B_x^2 \gg B_z^2$. These assumptions are reasonably valid for $kx \lesssim .8$ and for B_o sufficiently far from resonance and B_w small enough that $v_\perp \ll v_z$.

Furthermore, to insure that $\cosh kx = \text{constant}$ over the orbit, we restrict

$v_{lx} \ll v_{ly} = v_\perp$ (i.e., $\Omega_o < kv_z$). Then using Eqs. (8) and (6) in Eq. (7), we obtain

$$v_d = \frac{1}{2} v_z \frac{kv_z}{\Omega_o} \frac{(\Omega_w kv_z)^2}{(\Omega_o^2 - k^2 v_z^2)^2} \cosh kx \sinh kx. \quad (9)$$

Table 1 compares drift velocities for various cases from the code with $I = 0$ to those from Eq. (9). In general, the agreement is very good.

Clearly, the gradient drift is more severe when B_w is a considerable fraction of B_0 . However, if B_w is held constant at 1 kG and B_0 increased to 4 kG, $v_d(\gamma = 2.2)$ is not significantly reduced. This relative insensitivity to B_0 is due to the increased v_{\perp} , and hence a larger v_d , as B_0 approaches the cyclotron resonance field B_r . One consequence of this large drift near resonance is that it limits the degree of gain enhancement achievable through the magneto-resonance effect.^{4,16}

If B_0 sufficiently exceeds B_r , the drift can be quite small. For $\gamma = 2.2$ and $\lambda_w = 3$ cm, the resonant magnetic field $B_r = 7$ kG. With $B_0 = 8$ kG and $B_w = 1$ kG, the particle still drifts to the wall as shown in Fig. 4a. The drift is now in the opposite direction to that below resonance since v_{\perp} changes sign when $B_z > B_r$. This has the effect of changing the phase of v_y oscillations with respect to those of B_z ; i.e., v_y is positive (for $x > 0$) when B_z is a minimum, so that the particle drifts in the $+y$ direction. When B_0 is increased to 10 kG for this case, the drift is small enough that the electron remains confined for > 30 periods as shown in Fig. (4b). The confinement remains very good when the self fields of a 500 A beam are added.

In principle, operation of FEL experiments with $B_0 > B_r$ is possible and has been demonstrated with a high current, $\gamma = 3.5$ beam in a helical wiggler.⁴ However, competing processes such as the cyclotron maser¹⁵ interaction can produce large radiated powers at frequencies close to those of the FEL interaction in this beam energy and magnetic field regime.

Table 1.

B_0 (kG)	B_w (kG)	γ	$\frac{\Omega_0}{kv_z}$	X (cm)	$\frac{v_d}{c}$ (code)	$\frac{v_d}{c}$ (Eq. 9)
2	1	2.2	.29	.4	.047	.050
4	1	2.2	.5	.4	.042	.046
2	.5	2.2	.29	.4	.011	.013
2	1	2.2	.29	.2	.019	.022
2	1	3.0	.21	.4	.029	.034
4	1	3.0	.42	.4	.019	.022
4	.5	3.0	.42	.4	.0051	.0056
4	1	10.0	.11	.4	.0043	.0049
10	5	10.0	.28	.4	.057	.056

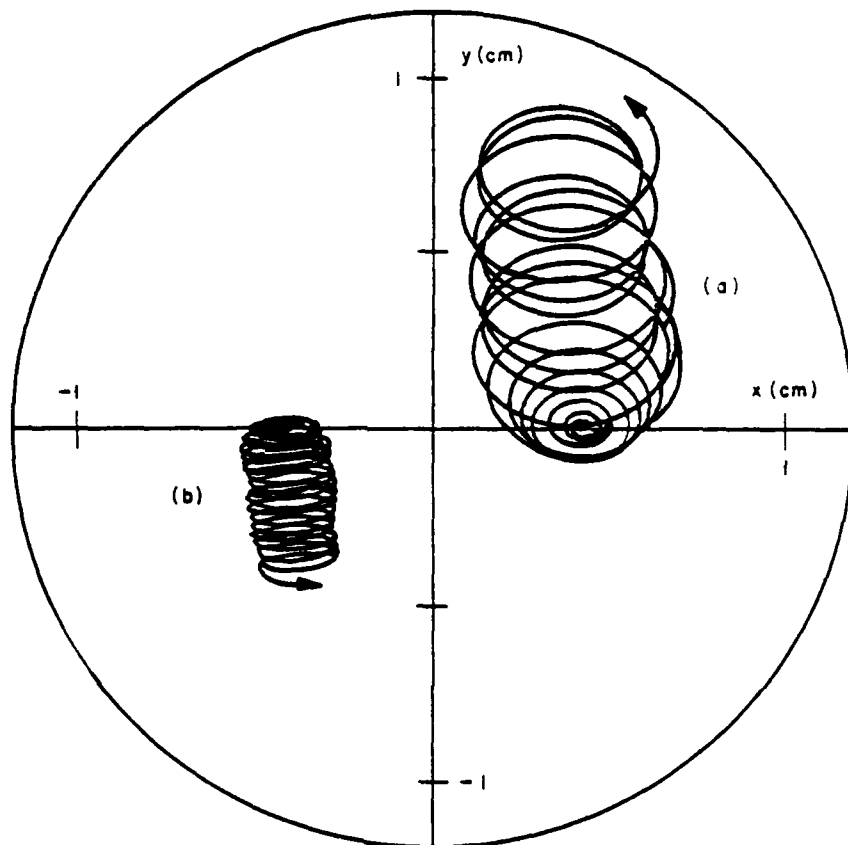


Fig. 4 - Electron trajectories in linear wiggler with $I = 0$, $\gamma = 2.2$, $B_w = 1$ kG, and $r_0 = .4$ cm. a) $B_0 = 8$ kG, b) $B_0 = 10$ kG.

Consequently, analysis of experimental results is more difficult. Also, arbitrarily large guide fields are not possible with a magnetically shielded diode simply because the electrons will be mirrored by the field. The equilibrium beam radius¹⁷ in such a case depends only on γ , I , B_0 , and the beam emittance ϵ , so for particular beam parameters suitable values of B_0 are limited. The required field¹⁸ in kG for a matched beam radius R in cm can be written

$$B^2 = \frac{1.36 I}{R^2 \beta \gamma} + \frac{11.56 \epsilon_n^2}{R^4}, \quad (10)$$

where I is in kA and ϵ_n is the normalized emittance in rad cm. For example, if $\epsilon_n = .14 \pi$ rad-cm (about the lowest value expected for a thermionic cathode beam with $I \approx 750$ -1000 A)¹⁸, a $\gamma = 2.2$ beam with $R = .3$ (.5) cm requires $B_0 = 5.5$ (2) kG for $I \leq 800$ A. In this regime, the beam is emittance dominated so that the required field is relatively insensitive to I . In principle, smaller radius beams could be used with larger B_0 , thereby doubly reducing v_d . However, experimentally this is very difficult at high current levels.¹⁷

To analyze the effect of a shielded diode on propagation through the wiggler, we repeat the above calculations with an initial v_g corresponding to $P_{\theta 0} = 0$. Note that $I = 1.75$ kA in this case, which is the current required for constant radius propagation in only the solenoidal field with these initial conditions. As shown in Fig. 5, the electron propagates at nearly constant radius until the wiggler amplitude becomes large enough that the

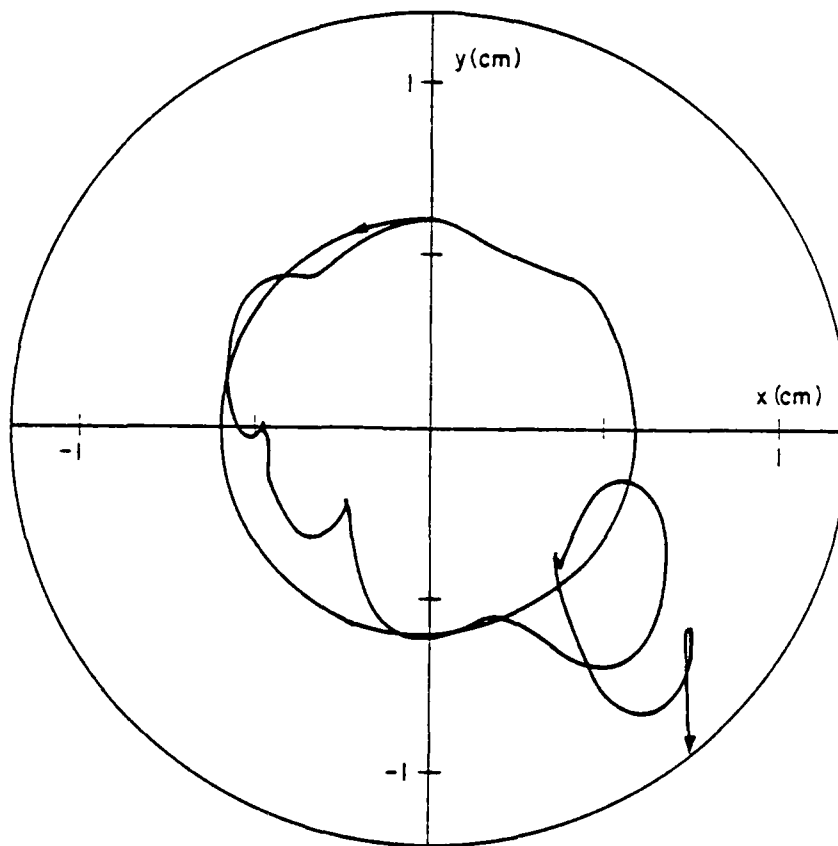


Fig. 5 - Electron trajectories in linear wiggler with $P_{\theta 0} = 0$, $I = 1.75$ kA,
 $\gamma = 2.2$, $B_0 = 2$ kG, $B_w = 1$ kG, $r_0 = .6$ cm.

gradient drift begins to dominate. Then the particle is lost just as in the $v_{\theta 0} = 0$ case.

The behavior of an off-axis electron in a linear wiggler and axial guide field should be compared to that when a helical wiggler is used.¹³ We approximate the helical wiggler field by⁶

$$\begin{aligned} B_x^h &= b(z)B_w \left\{ -\sin kz \left[1 + \frac{1}{8} k^2 (3x^2 + y^2) \right] + \frac{1}{4} k^2 x y \cos kz \right\} \\ B_y^h &= b(z)B_w \left\{ \cos kz \left[1 + \frac{1}{8} k^2 (x^2 + 3y^2) \right] - \frac{1}{4} k^2 x y \sin kz \right\} \end{aligned} \quad (11)$$

$$B_z^h = -kb(z)B_w \left[1 + \frac{1}{8} k^2 (x^2 + y^2) \right] (x \cos kz + y \sin kz).$$

This expansion of the true Bessel function expression for B^h is valid for $kr \ll 1$. Friedland's treatment¹³ of electron propagation in this case assumes a radially uniform wiggler, and his stability condition (Eq. 2a) is not stringent enough when the radial variation is included. For example, Friedland finds stable orbits when $\gamma = 1.587$, $\lambda_w = 4$ cm, $v_{\perp 0} = 0$, $r_0 = 0$, $B_0 = 1.26$ kG, and $B_w = 1.04$ kG, so that Eq. 2a is barely satisfied, and we can duplicate his results if we remove the radial variation from B^h . However, with the B^h given in Eq. 11, we find that the wiggler field must be reduced to ~625 G to obtain stable orbits.

Although the radial dependence in B^h does narrow the allowable range of operating parameters, stable orbits with $\langle r \rangle = \text{const}$ are achievable with a helical wiggler in a guide field. Electron trajectories in a helical wiggler for the same conditions as used previously with a linear wiggler are shown in

Figs. 6 and 7. Figure 6 is to be compared to Fig. 2 and Fig. 7 to Fig. 5. In both cases, the electron is well-confined. It is interesting to note that in Fig. 6, the electron born at $(x,y) = (.4,0)$ initially $\vec{E} \times \vec{B}$ drifts in the $+\theta$ direction, but then reverses direction as the wiggler amplitude increases. Since $\text{grad } B^h$ is radial, the $\text{grad } B^h$ drift is in the $-\theta$ direction and does not lead to the beam expansion observed with the linear wiggler.

The linear wiggler drift described here imposes additional constraints on the parameters of an FEL experiment. Obviously, the beam radius must be kept as small as possible to minimize particle loss from the edge of the beam. Preliminary experimental results by our group with a field immersed, apertured source indicate that particle losses can be kept acceptably small in this way. Also, if γ is large enough that $B_r \gg B_0 \gg B_w$ can be satisfied for relatively large B_w , then the drift can be kept small while achieving acceptably large v_w .

Finally, it should be noted that the drift arises from the asymmetry of the linear wiggler and the corresponding absence of focusing forces in the direction perpendicular to the wiggler field. Therefore, it should be possible to stabilize the drift by imposing an additional focusing force in that direction. For example, preliminary results indicate that electron propagation through a "square" or symmetrized linear wiggler is very stable. Such a wiggler has an additional component $B_y^L = \cosh ky \cos kz$ and a corresponding addition to B_z^L of $-B_w \sinh ky \sin kz$. An electron trajectory through such a wiggler is shown in Fig. 8.

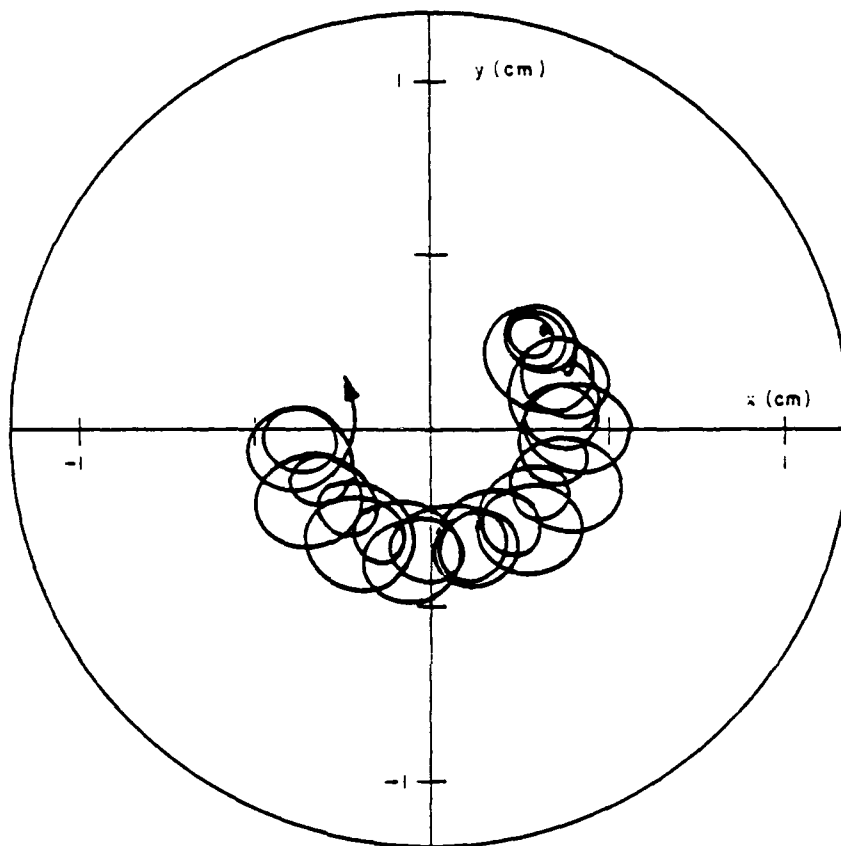


Fig. 6 - Electron trajectories with helical wiggler and $\gamma = 2.2$, $B_0 = 2$ kG, $B_w = 1$ kG, $\lambda_w = 3$ cm, $I = 250$ A, $r_0 = .4$ cm, and $v_{10} = 0$.

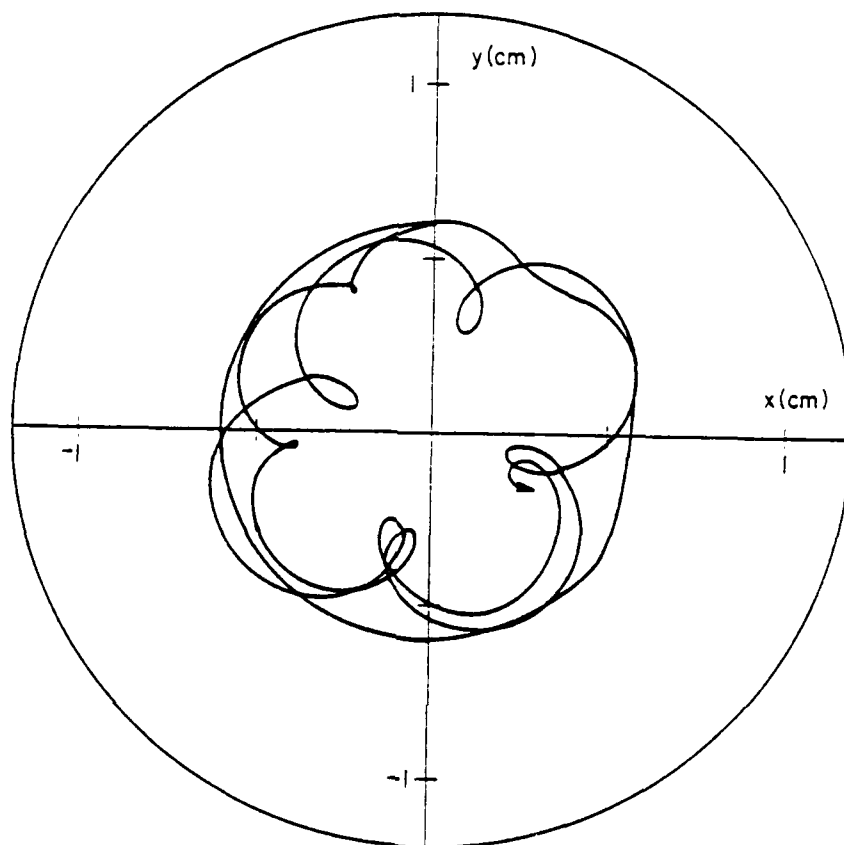


Fig. 7 - Electron trajectories in helical wiggler with $P_{\theta 0} = 0$,
 $I = 1.75$ kA, $\gamma = 2.2$, $B_0 = 2$ kG, $B_w = 1$ kG, and $r_0 = .6$ cm.

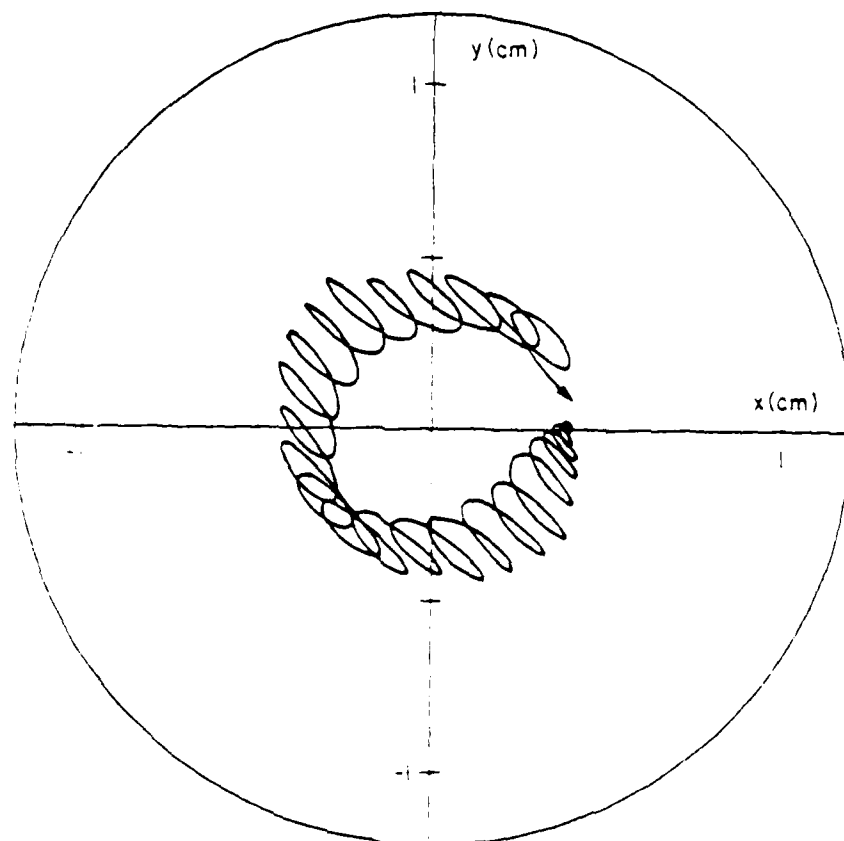


Fig. 8 - Electron trajectories in symmetrized linear wiggler with $I = 0$, $\gamma = 2.2$, $B_0 = 2$ kG, $B_w = 1$ kG, $r_0 = .4$ cm, and $v_{10} = 0$.

In conclusion, a gradient drift has been shown to exist for a linear wiggler in an axial guide field. The drift can be substantial with small or large beam current in some parameter ranges, for a wide range of initial conditions. However, the advantages of a linear wiggler are sufficient in many cases to either limit operation to a "stable" parameter regime or to impose additional focusing forces to stabilize the drift.

The authors gratefully acknowledge useful discussions with C.A. Kapetanacos, H. Freund, and C.M. Tang.

REFERENCES

1. L.R. Elias et al., Phys. Rev. Lett. 36, 717 (1976).
2. D.A.G. Deacon et al., Phys. Rev. Lett. 38, 892 (1977).
3. D.B. McDermott et al., Phys. Rev. Lett. 41, 1368 (1979).
4. R.K. Parker et al., Phys. Rev. Lett. 48, 238 (1982).
5. H. Boehmer et al., Phys. Rev. Lett. 48, 141 (1982).
6. B.M. Kincaid, J. Appl. Phys. 48, 2684 (1977).
7. J.P. Blewett and R. Chasman, J. Appl. Phys. 48, 2692 (1977).
8. K. Halbach, IEEE Trans. Nucl. Sci. 28, 3136 (1981).
9. C.W. Roberson et al., Proc. of 6th Int'l Conf. on Infrared and Millimeter Waves, Miami Beach, (1981) to be published in Int'l J. IR and MM Waves .
10. R.M. Phillips, Trans. IRE ED-7, 231 (1960).
11. K.D. Jacobs, R.E. Shefer, and G. Bekefi, Appl Phys. Lett. 37, 583 (1980).

12. N.M. Kroll, P.L. Morton, and M.N. Rosenbluth, "Variable Parameter Free Electron Laser," in Free Electron Generators of Coherent Radiation, Physics of Quantum Electronics, Vol. 7, Ed. by S.F. Jacobs, J.S. Pillof, M. Sargent III, M.O. Scully and R. Spitzer, Addison-Wesley Pub. Co. (1980).
13. L. Friedland, Phys. Fluids 23, 2376 (1980).
14. H.P. Freund and A. Drobot, Phys. Rev. A 24, 1965 (1981).
15. R.E. Shefer and G. Bekefi, Bul. Am. Phys. Soc. 26, 864 (1981).
16. H.P. Freund et al., to be published.
17. M. Reiser, Phys. Fluids 20, 477 (1977).
18. V.K. Neil, JASON Tech. Report JSR-79-10, SRI International, Arlington, VA (1979).

Numerical Simulation of High Energy Light
Ion Beam Flow Through a Foilless Diode

R. J. Barker, C. W. Roberson and F. Mako

NRL Memorandum Report 5058
July 21, 1983

REPORT DOCUMENTATION PAGE		READ INSTRUCTIONS BEFORE COMPLETING FORM
1. REPORT NUMBER	2. GOVT ACCESSION NO. 3. RECIPIENT'S CATALOG NUMBER	
NRL Memorandum Report 5058		
4. TITLE (and Subtitle)	5. TYPE OF REPORT & PERIOD COVERED	
NUMERICAL SIMULATION OF HIGH ENERGY LIGHT ION BEAM FLOW THROUGH A FOILLESS DIODE	Interim report on a continuing NRL problem.	
6. PERFORMING ORG. REPORT NUMBER		
7. AUTHOR(s)	8. CONTRACT OR GRANT NUMBER(s)	
R.J. Barker,* C.W. Roberson† and F.M. Mako@		
9. PERFORMING ORGANIZATION NAME AND ADDRESS	10. PROGRAM ELEMENT, PROJECT, TASK AREA & WORK UNIT NUMBERS	
Naval Research Laboratory Washington, DC 20375	61153N: RR0110941; 47-1484-0-3	
11. CONTROLLING OFFICE NAME AND ADDRESS	12. REPORT DATE	
Office of Naval Research Arlington, VA 22217	July 21, 1983	
13. NUMBER OF PAGES		
22		
14. MONITORING AGENCY NAME & ADDRESS (if different from Controlling Office)	15. SECURITY CLASS. (of this report)	
	UNCLASSIFIED	
15a. DECLASSIFICATION/DOWNGRADING SCHEDULE		
16. DISTRIBUTION STATEMENT (of this Report)		
Approved for public release; distribution unlimited.		
17. DISTRIBUTION STATEMENT (of the abstract entered in Block 20, if different from Report)		
18. SUPPLEMENTARY NOTES		
*Present Address: Mission Research Corp. Alexandria, VA †Present Address: JAYCOR, INC. Alexandria, VA @Present Address: Office of Naval Research, Arlington, VA		
19. KEY WORDS (Continue on reverse side if necessary and identify by block number)		
Numerical Simulation Foilless Diode Intense Relativistic Electron Beams Intense Ion Beams Collective Ion Acceleration		
20. ABSTRACT (Continue on reverse side if necessary and identify by block number)		
A numerical and theoretical study is reported which treats the effects upon a 500 keV, hollow electron beam in a foilless diode along the centerline of which has been injected a beam of 30 MeV protons. Specifically, the results of simulations of three, separate equilibrium diode states (for electron-only, 1 kA of protons, and 5 kA of protons) are reported. The computational findings are compared to rough, theoretical predictions and very good agreement is observed. The conclusion may be drawn that, for the diode parameters studied, a 1 kA beam of 30 MeV protons		

(Continued)

DD FORM 1473

JAN 73

EDITION OF 1 NOV 65 IS OBSOLETE
S/N 0102-014-6601

SECURITY CLASSIFICATION OF THIS PAGE (When Data Entered)

20 ABSTRACT (Continued)

does not seriously disrupt the electron beam. On the other hand, a 5 kA proton beam not only radically alters the REB characteristics but also itself falls prey to strong, radial ballooning.

CONTENTS

I. INTRODUCTION	1
II. THE FOILLESS DIODE	2
III. NUMERICAL IMPLEMENTATION	3
IV. RESULTS	3
V. THEORY COMPARISON	5
VI. CONCLUSIONS	8
REFERENCES	8

NUMERICAL SIMULATION OF HIGH ENERGY LIGHT ION BEAM FLOW THROUGH A FOILLESS DIODE

I. INTRODUCTION

Interest remains high in the quest for a compact, high energy, intense light-ion beam accelerator. Some of the areas of application for such an accelerator include directed energy systems, inertial confinement fusion drivers and magnetic fusion fuel injectors. The desired operating parameters for such an accelerator are an ion energy of from 0.1 to 1 GeV, a beam intensity of from 10^{13} to 10^{16} ions/cm² per pulse, and a pulse length of from less than one nanosecond to a millisecond. To be termed "compact," the device should not measure more than 10 to 30 meters in any dimension.

The ability to generate intense relativistic electron beams (IREB's) in foilless diodes^{1,2} has brought the concept of a compact ion accelerator very close to a reality in the form of collective ion accelerators (CIA's). These collective accelerators have received much attention over the years.³⁻⁶ Their operation relies upon the existence of localized, collective field gradients in excess of 1 MV/cm in an IREB. In comparison, conventional accelerators provide electric fields on the order of only 0.01 MV/cm which is unacceptable for a "compact" device. Although many approaches exist for achieving the acceleration of positive ions via the collective electric field produced by an intense relativistic electron beam, not all approaches can be scaled-up to achieve high ion energies. Scaleability implies a systematic procedure for maintaining synchronization between the ion being accelerated and its accelerating electrostatic potential well. This requirement of scaleability may be generalized to any type of accelerator.

The "space charge wave accelerator" concept has been proposed at NRL to achieve such scaleability.⁷ The fundamental idea behind the concept is the sustained matching of ion beam velocity with the phase velocity of the accelerating IREB space charge wave along the entire length of the CIA (collective ion accelerator). The most formidable challenge to this concept is the matching of injected ion beam velocity with the minimum electron space charge wave velocity. Technical restraints appear to place a lower limit of 0.2-0.3 c on the phase velocity of the fundamental mode of a 1 MeV IREB space charge wave. This dictates an injected proton energy of 16-30 MeV. If that synchronization of initial velocities can be met, the geometry of the accelerator cavity can be designed to keep v_{ion} and v_{phase} in step. The specific design used is termed the Converging Guide Accelerator or CGA.⁸ The phase velocity of the wave in a conducting cylinder depends on the ratio of beam to wall radii. The phase velocity increases inversely with this ratio. Thus, the wave can be accelerated by accelerating the beam. The beam can be accelerated by passing it through a metal tube with a converging radius.

In Fig. 1, ions are injected from the right along the central axis of the electron beam which is also propagating from right to left. Next, a space charge wave is excited and grows around the ions. The ions loaded into the wave are accelerated by it as it too accelerates in step. The electron beam is then dumped and the ions extracted from the far left. Two meters of magnetic field at a strength of 20 kG are required for this system. Initially, the electron beam planned for use with this system will have an energy of 0.5 MeV and a current of 1.4 kA for 250 nsec. Also, the electron beam generator can be operated at 10 pulses per second. The trace that is shown in Fig. 1 is a photograph of the machine voltage versus time. The high voltage machine was used in conjunction with a resistive load. For proof-of-principle testing, low-current, 30 MeV proton beams could be injected from a conventional ion accelerator such as the cyclotron at NRL.

Manuscript approved March 28, 1983.

Such a low ion current experiment can indeed test the wave accelerator concept but there remains another question to be answered before kiloamp-level, injected beam devices are constructed. What are the consequences of injecting into a foilless diode a 30 MeV proton beam of comparable amperage to the current normally carried by the electrons alone in the diode. How will the structure of the potential well inside the hollow electron beam be effected? Will the net electron current flowing through the diode increase and, if so, by how much? These are the matters addressed by the computational research reported herein. The findings demonstrate that an injected 30 MeV proton beam carrying 10% of the normal diode electron current will not seriously effect the potential well structure in or the electron current of the foilless diode. A five-fold increase in the ion beam current, on the other hand, destroys the well and doubles the electron current. Thus, clearly "safe" and clearly "unsafe" ion current levels have been established. The determination of an exact "critical" ion current for use in the CGA device is not important at this time and has been left for future research.

In the section that follows, the actual physical device to be simulated is described in detail. Section III then outlines the key characteristics of the DIODE2D computer code which was used to conduct the numerical simulation. The numerical results are presented in Section IV including such information as radial profiles of beam current density and plots of the electrostatic potential well structure in the diode. In order to give added emphasis and understanding to the numerics, Section V is devoted to a simple theoretical analysis of the physics of the ion beam and diode. Good agreement is found between the theoretical predictions and the numerical findings. Finally, Section VI summarizes the major conclusions that can be drawn from this work and suggests material for future research.

II. THE FOILLESS DIODE

The physical diode designed for the experimental testing of this new CGA concept closely resembles that shown in Fig. 2. It corresponds roughly to the "wave growth" section of the accelerator shown in Fig. 1. The coaxial, vacuum, power feed line tapers inward radially as it traverses the axial length of the near-conical cathode. The tip of the cathode coincides with the entrance plane of a long (>1 meter) cylindrical drift tube. The outer radius of the cathode is about 1.5 cm. A hole 0.5 cm in radius is bored through the center of the cathode to serve as the injection port for the high energy ion beam. The coaxial, conical A-K gap has a length of about five centimeters. The drift tube is given an inner radius of about 1.7 cm. The entire apparatus is immersed in a uniform axial magnetic field of about 10 kilogauss.

Ideally, the model diode to be numerically simulated would correspond exactly to that depicted in Fig. 2. Unfortunately, the simulation code, DIODE2D, which was used in these studies was incapable of efficiently handling that specific geometry. Particularly troublesome are the sloped walls of the cathode and of the coaxial power feed line as well as the overall meter-long length of the physical system. The existing code was capable of treating only conducting surfaces and boundaries which are strictly radial or strictly coaxial (i.e., they must have a rectangular $R-Z$ cross-section). Thus, a cylindrical cathode shank of some finite thickness must be substituted for the conical one. Furthermore, a combination of limited resolution and finite computer data storage capabilities prohibits the accurate treatment of a system less than 2 cm in radius but over 100 cm long. The total axial length of the model system will be shortened instead to 10 cm. The peculiarities of the Poisson-solver for the electric and magnetic potentials in that system also required that the tube be terminated by a fixed-potential, conducting wall.⁹ The final approximation to the original system took the form shown in Fig. 3.

The cathode used in the numerical model is a hollow cylinder 1.2 cm in radius with a shank wall thickness of 0.4 cm. It projects axially 2.5 cm into the 10.0 cm long drift-tube (anode). The anode tube inner radius is at 1.7 cm. This leaves a radial A-K (anode-cathode) gap of 0.5 cm which very comfortably exceeds the 0.17 cm gyroradius of a 0.5 MeV electron in a 10 kG magnetic field. Analysis using existing theory¹⁰⁻¹² leads to estimates of foilless diode electron beam currents of 8-10 kA or diode

power levels of 4-5 GW. Along the central axis of this device will be injected a 0.7 cm radius beam of 30 MeV protons. Three separate simulations were conducted of this configuration. The first was a "benchmark" run to determine the normal, electrons-only operating characteristics of the foilless diode. Of importance is not only the gross e -beam current but also the beam profile and the structure of the electrostatic potential well inside the beam. The final two simulations were conducted with the high-energy proton beam flowing through the device. Specific ion beam currents of 1 kA and 5 kA were chosen for these two test cases.

III. NUMERICAL IMPLEMENTATION

A modified, electrostatic-magnetostatic version of NRL's DIODE2D computer code was used to carry out the simulations. The details of the code may be found elsewhere.¹³ It is sufficient here to note that the code is 2-1/2-dimensional in that it explicitly moves particles in R and Z (radially and axially) in space while keeping track of all three components of their canonical momentum. The treatment is fully relativistic for both electrons and protons. Unlike a full electromagnetic simulation code, DIODE2D is designed to find only equilibrium charge, current, and field configurations in the device under study.

Particle contributions to net charges and currents as well as the resulting E and B field values are stored in a mesh of discrete data points covering the entire diode. The spacing between data points was fixed at $R = 0.05$ cm radially and $Z = 0.078$ cm axially. This allowed for 34 data cells to span the 1.7 cm from the centerline to the inner radius of the anode tube and 128 cells from the back of the cathode to the anode endplate. The protruding cathode shank measured 8 data cells thick and 32 cells long. On its front face, electron emission was permitted from the outer 7 of the 8 possible emission points. The eighth cell was not allowed to emit in order to obtain additional numerical accuracy in the field values governing electron emission from the inside lip of the cathode shank. Emission was permitted all along that inner, as well as the outer shank surface except for the rearmost 6 cells.

The magnitude of the electron emission from a given cathode surface is determined by the amount of space charge necessary to zero out the perpendicular component of the electric field at the emission point. In order to simulate the injection of the 30 MeV proton beam of predetermined amperage, the inner 14 cells of the cathode endplate inside the shank were designated as proton "emission" points. The emission at those points, however, was completely independent of the adjacent electric field values. A constant, emitted current density, J_e , of 0.65 kA/cm² was imposed for the 1 kA beam case and 3.25 kA/cm² for the 5 kA case at each of the 14 points. Particles of both species were perfectly absorbed upon hitting any of the boundary surfaces, including the surfaces of the protruding cathode shank.

All quantities of interest in the device were monitored by the computer code's extensive diagnostics. Electron and ion, emitted and collected current densities were recorded over all relevant surfaces. Electrostatic equipotential contour lines and magnetic field lines throughout the device were plotted. Sample values of all three components of the magnetic field are similarly recorded. Net charges and currents were periodically listed. Finally, the positions of statistical samplings of electrons and protons were plotted at equilibrium.

IV. RESULTS

First, a "benchmark" simulation was run in which only electrons were allowed in the diode. In agreement with theory (see Section V), a net electron current of 9.6 kA was measured. Of that total amount, 2.8 kA was emitted from the face of the cathode shank tip while the remaining 6.8 kA originated from the outside surface of the shank. Emission from the inner shank surface was negligible. A net electron charge of -1.86×10^6 statcoulombs was found to be in the system. Figure 4 presents a

plot of sample electron positions at equilibrium. Of note is the waviness of the outer envelope of the electron beam. Similar beam behavior was observed in foilless diode simulations conducted by R. Jackson^{14, 15} and others. The electrostatic potential contour plot for the device modeled in simulation is shown in Fig. 5. The beam envelope waviness is mirrored in these equipotentials. It is also clear from this figure that the electric field inside the hollow cathode is negligible, in agreement with the vanishingly small electron emission observed there. It also appears that electrons leaving the cathode are fairly rapidly accelerated to the 40% equipotential (0.2 MeV) before entering a virtual "drift region" about 3.5 cm long starting about 2.0 cm downstream of the cathode tip. Electron energy and velocity are nearly constant in this region as would be the case in an actual full-length foilless diode drift tube. It is therefore that region where beam behavior will most closely mimic a realistic device. Finally, the self-magnetic field lines generated by the α -beam are depicted in Fig. 6. Imposed over this self-field pattern is the uniform 10 kG background field. Up to about $Z = 8.5$ cm, the beam field is diamagnetic in nature, lowering the inside, imposed B_z by about 40-80 gauss and intensifying the field near the anode tube by a like amount. The self-field between $Z = 8.5$ and 10.0 cm, where electrons receive a final 0.3 MV of acceleration, is of the opposite orientation. However, that region as well can boast of only 50-100 gauss field strengths.

The second case to be tested was that involving the 1 kA, 30 MeV proton beam injected in the manner described in the previous section. The net electron current in the new equilibrium increased by 2 kA to 11.6 kA. Of that total current, 4.3 kA was being emitted from the tip (compared to 2.8 kA for the electrons-only case), 0.4 kA were coming from the inner shank surface, while the outer shank surface emission remained practically unchanged at 6.9 kA. The ion beam had introduced a total charge of $+4.06 \times 10^3$ statcoulombs into the diode while the electron charge had increased to -2.11×10^4 statcoulombs. Thus, the electron beam characteristics of the diode itself had changed very little. In addition, the ion beam envelope experienced virtually no ballooning. This is evident from Fig. 7 which presents the steady-state ion beam envelope superimposed over the sample electron position plot. The qualitative character of the hollow electron beam has likewise remained essentially unchanged. The first truly major change manifests itself in the equipotential plot of Fig. 8. Comparison with Fig. 5 shows the distortions caused by the concentration of positive space charge along the axis. The contours are sucked into the hollow cathode up to the 40% potential. This accounts for the turn-on of electron emission there. Also, electrons reaching the previously-mentioned "drift region" between $Z = 4.5$ to $Z = 8.0$ cm are now at about 0.25 MeV instead of the 0.20 MeV of the electrons-only case. Finally, Fig. 9 shows the changes made to the self-magnetic field lines generated by the electron beam. The magnitudes of those fields in the drift region remain unchanged in the range of 40 to 80 gauss, but the orientation of the field has reversed. The imposed B_z is now strengthened inside the beam and weakened outside. Although this effect is interesting, the small field strengths make it unimportant to the operation of the diode.

For the third and final test case, the current of the 30 MeV proton beam was increased to 5 kA. The steady state electron current rose to 19.7 kA with 8.3 kA from the shank face, 4.7 kA from its inner surface, and an outer shank emission current almost identical to the previous two cases at 6.7 kA. Of course, the ion charge increased by the same factor of five as its current to $+2.04 \times 10^4$ statcoulombs. In partial compensation, the net electron charge had grown to -3.32×10^4 statcoulombs. Clearly the normal operation of the foilless diode has been seriously disrupted. Its electron current has more than doubled. Even more dramatic is the destruction of the ion beam. This is illustrated by the equilibrium sample particle plot of Fig. 10. The proton beam envelope has expanded halfway through the width of the hollow electron beam by the time it arrived at the end of the drift tube. Similarly the electrostatic potential contours shown in Fig. 11 no longer bear much resemblance to the ion-free case of Fig. 5. Electrons now experience almost 80% of the total diode potential increase before entering the "drift region." There no longer exists any effective "potential well" through which the proton beam can travel. Finally, the self-magnetic field of the electrons (see Fig. 12) can no longer be ignored. Its drift region magnitudes now range from about 200 to 700 gauss which is an appreciable fraction of the

imposed 10 kG field. As in the 1 kA ion beam case, this self-field strengthens the B_z along the axis and weakens it outside the e -beam radius.

The major results of the above three simulations are summarized in Table 1. The statement can be made that the injection of a 1 kA, 30 MeV proton beam along the axis of the foilless diode being studied, does not seriously disrupt the normal operating characteristics of the device. The injection of a 5 kA, 30 MeV ion beam does cause serious disruption. Correspondingly, the 1 kA beam is virtually unaffected by its passage through the diode, while the 5 kA beam undergoes severe ballooning. In order to better understand these macroscopic results, it is important to examine the modifications made by each case on the individual current density profiles of each case. Figure 13 depicts the radial profiles of the electron current density, J_e , emitted from the tip face of the cathode shank. The profiles all have a characteristic double-pronged shape.¹⁴ They show that for this diode the doubling of the emitted currents on this surface is predominantly occurring at the points of lower radius. Those points are closer to the ion beam, whose space-charge has grossly distorted the electric field values there. From Fig. 14, however, it is obvious that the electron emission from both the inner and the outer shank surfaces are virtually identical for the electrons-only and the 1 kA beam case. Since some 70% of the total diode current originates on the outer surface, this agrees with the overall close similarity between the two cases. The 5 kA beam case is quite a different matter. Although the net outside shank emission is about the same as the previous cases, the axial profile of J_e is grossly depressed over the front half of the shank and mildly enhanced over the rear half. This is a manifestation of the 2 1/2-fold increase in the value of B_z along that surface. The near-normal amount of negative charge emitted from the rear half is prevented from leaving the near vicinity of the shank as it travels toward the front face. This negative space charge then impedes the electron emission along the front half of that surface. The most dramatic change, however, is in the inner shank surface emission. For the 5 kA beam case, the emission there rivals that of the outside surface. For the other two cases that inner surfaces had been effectively non-emitting. The combined emission changes are all reflected in the radial profiles of electron current densities collected at the anode face ($Z = 10$ cm). These are shown in Fig. 15. In addition to the overall enhancement of collected current from case to case, a distinct pinching of the beam toward the central axis can be seen. This is to be expected due to the increased self-magnetic field strength but the magnitude of the radial displacement of the mean current density is limited by the imposed 10 kG axial B -field.

The final diagnostic measured the radial profiles of the 30 MeV proton beam in the plane located at $Z = 7.5$ cm, well inside the electron beam "drift region." Two profiles are shown for the 1 kA beam case in Fig. 16. The first represents the initial, imposed beam profile a mere 50 timesteps ($\Delta t = 2 \times 10^{-12}$ sec) after the beginning of the simulation. The other profile shows the modest spread of the beam about 0.8 nano-seconds later. The change is quite negligible, indicating excellent confinement and stability of the beam. Once again, the 5 kA case is dramatically different. The corresponding profiles for that high current beam are shown in Fig. 17. Over the same 0.8 nanosecond period, this beam has expanded from its initial 0.7 cm radius to over 1.0 cm, well beyond the inner cathode shank radius and the inner radius of the hollow electron beam. That configuration is clearly unstable.

V. THEORY COMPARISON

In this section analytic expressions are derived and compared to the simulation results. The two major results are the radial ballooning of the ion beam and the increase in the electron limit current as the ion current is increased. Agreement between theory and computation is quite good.

The radial equation of motion for the ions decouples and only the ion beam's self fields determine the ion motion. This is true for times that are short in comparison to the axial gyro-period. That is, $t^2 \ll \Omega_i^{-2}$, where, $\Omega_i = \frac{qB_z}{\gamma M}$ and B_z is the axial magnetic field. Also, for $\beta^2 \ll 1/2$, where β is

the ion velocity divided by the speed of light, then changes in the relativistic mass factor can be neglected. With these assumptions the equation of motion for the ions at the beam surface is given by

$$\gamma M \frac{d^2 r}{dt^2} = qE_r - qV_z B_\theta \quad (1)$$

where: q and M are the ion charge and mass, E_r and B_θ are the self electric and magnetic fields in the ion beam, γ is the relativistic mass factor, V_z is the axial ion velocity, and r is the radial position of ions at the beam surface. Assuming current conservation Eq. (1) reduces to¹⁷

$$\frac{d^2 r}{dt^2} = \frac{k}{r} \quad (2)$$

where: $k = \frac{qI}{2\pi\epsilon_0 M V_z \gamma^3}$, I is the ion beam current, and ϵ_0 is the dielectric constant of free space. Equation (2) can be solved in series form¹⁸ to give,

$$\sum_{n=0}^{\infty} \frac{(\ln(r/r_0))^{n-1/2}}{(2n+1)n!} = \frac{\sqrt{k/2}}{r_0} t, \quad (3)$$

where: r_0 is the initial beam radius at $t = 0$ and r is the final radius at time t . In Table 2, a comparison is made between the code time, t , to reach the final radius, r , and the time calculated by Eq. (3). This comparison is made for 30 MeV protons.

It is clear from the comparison that the self fields of the ion beam determine its motion. Of the self fields, the electric field dominates in the expansion. This result does not limit the maximum ion current. Since, the ion beam expands to the diameter of the electron beam, its electric field is reduced thus allowing for more ion current to flow. Increasing the ion current then increases the electron limit current which in turn allows for an increase in the ion current, etc.

In addition to the problem of ion beam ballooning, the simulation also addressed the major question of changes in the diode's electron current due to the presence of the ion beam. The maximum electron current is determined by the potential distribution along the electron-emitting cathode surfaces. When ions are present the potential is raised and hence the limit current is increased.

In Fig. 18 electrons and ions are moving in the same axial direction. A large external magnetic field is applied in the direction of particle motion, z . This field is large enough to magnetize the electrons but not the ions. Furthermore, the assumptions are made that (a) J_e and J_i are uniform, (b) $|B_\theta|$ and $|B_{\theta e}| \ll |B_z|$, (c) $|E_r| < |B_z|c$, and (d) Electron velocity shear can be neglected (where J_e and J_i are the electron and ion current density; $B_{\theta i}$, $B_{\theta e}$ and B_z are the ion, electron and external, magnetic fields; E_r is the radial ion electric field; c is the vacuum speed of light).

From Gauss' law the potential inside the electron beam, region 3, (see Fig. 20) is given by the expression,¹⁹

$$\phi(r) = \frac{I_i}{2\pi\epsilon_0 V_i} \ln(R/r) - \frac{I_e}{4\pi\epsilon_0 V_z} \left[\frac{r_2^2 - r^2}{r_2^2 - r_1^2} + 2 \ln R/r_2 - \frac{2r_1^2}{r_2^2 - r_1^2} \ln(r_2/r) \right] \quad (4)$$

where I_i and I_e are the ion and electron current, V_i and V_z are the ion and electron velocity, and ϵ_0 is the permittivity of the free space. The quantity, ϕ , may be eliminated from Eq. (4) by using conservation of energy,

$$\frac{-mc^2}{e} (\gamma - \gamma_0) = \phi. \quad (5)$$

The maximum electron current can then be found by setting $\frac{dI_e}{d\gamma}$ to zero, thus yielding

$$I_e \leq \frac{\left[I_0(\gamma_0 - \gamma) - (2I_i/\beta_i) \ln \left(\frac{R}{r} \right) \right] (1 - 1/\gamma^2)^{1/2}}{\left[\frac{r_2^2 - r^2}{r_2^2 - r_1^2} + 2 \ln R/r_2 - \frac{2r_1^2}{r_2^2 - r_1^2} \ln \left(\frac{r_2}{r} \right) \right]} \quad (6)$$

where

$$I_0 = \frac{4\pi\epsilon_0 mc^3}{e} \approx 17 \text{ kA}, \quad (7)$$

$$\gamma = \left[\frac{2I_i}{\beta_i I_0} \ln \left(\frac{R}{r} \right) - \gamma_0 \right]^{1/2}, \quad (8)$$

$mc^2\gamma_0$ is the initial electron energy, m and e are the electronic mass and charge, and β_i is the ion velocity normalized to the vacuum speed of light.

By inspecting the first term in Eq. (8) it is clear that the presence of the ion current raises the final electron energy. This energy increase plays only a small role in the limit current expression. The biggest ion effect arises in Eq. (4) where the potential is directly increased by an increase in the ion current.

The magnitude of the limiting electron current of Eq. (6) varies with the radial position, r . In general Eq. (6) should be integrated from r_1 to r_2 to give a current that is weighted by the changing potential across the beam. However, since the equation itself is only a simple approximation, seeking such extra "precision" would be pointless. Instead, Eq. (6) will be evaluated at different radii and the effects discussed. An upper bound to the limit current can be obtained by setting $r = r_2$ then Eq. (6) becomes

$$I_e \leq \left[\frac{I_0(\gamma - \gamma_0)}{2 \ln R/r_2} + \frac{I_i}{\beta_i} \right] (1 - 1/\gamma^2)^{1/2}, \quad r = r_2. \quad (9)$$

This gives an upper bound to the limit current since all particles are experiencing the maximum potential near the wall. A comparison is made in Table 3. If Eq. (6) is evaluated at $r = r_1$ then the result is,

$$I_e \leq \frac{\left[I_0(\gamma_0 - \gamma) + 2 \frac{I_i}{\beta_i} \ln (R/r_1) \right] (1 - 1/\gamma^2)^{1/2}}{\left[1 + 2 \ln R/r_2 - \frac{2r_1^2}{r_2^2 - r_1^2} \ln (r_2/r_1) \right]}, \quad r = r_1. \quad (10)$$

Note that when no ions are present, this will give a lower bound to the limit current since all of the particles are exposed to a potential minimum. Table 4 shows a comparison of Eq. (10) with the code results. As expected, the theoretical prediction is well below the code findings for the case with no ion beam present. For the two cases with ion injection, however, the addition of positive space charge inside $r = r_1$, elevates the potential there to such a degree that for the 5 kA case it actually exceeds that observed in Table 3 for $r = r_2$. It is clear from both Table 3 and Table 4 that the comparison between simulation and theory is quite good, considering the theoretical approximations that were made. Thus a scaling law for the electron limit current dependence on the ion current can be inferred. This effect can have a major impact on wave phase velocity control for the space charge wave accelerator. For example if the injection current is fixed a change in the ion current will shift the wave phase velocity thus removing ions from wave synchronization. However, at high γ_0 and for modest ion currents the effect is small. For example, if $I_i/I_e = 0.1$ and $\gamma_0 = 7.0$.

$$\frac{\Delta\gamma}{\gamma_0} \equiv \frac{\gamma - \gamma_0^{1/3}}{\gamma_0} \quad (11)$$

$$= \frac{1}{\gamma_0^{2/3}} \left\{ \left[1 - \frac{2I_i}{\gamma_0 \beta_i I_0} \ln \left(\frac{R}{r} \right) \right]^{1/3} - 1 \right\}$$

$$< 0.01.$$

Thus, the two major code results have been explained. Analytic expressions have been derived for predicting these results and good agreement was found between theory and code results. The mechanism for ion ballooning has been shown to be due primarily to the self electric field of the ion beam. Increases in the electron limit current are shown to be associated with an increase in the ion current. As discussed, a coupling between the ion and electron currents can negatively impact on ion-wave synchronization for the space charge wave accelerator.

VI. CONCLUSIONS

The numeric simulations presented here give the first documented evidence that a high current, high energy light ion beam can be injected down the central axis of a conventional foilless diode without either seriously disturbing the operating characteristics of the diode or causing significant disruption of the ion beam itself. For the 4-5 GW foilless diode studied and for a proton energy of 30 MeV a beam current of 1 kA can easily be tolerated. Increasing the ion beam current to 5 kA leads to a general break-down of the beam-diode system. The precise current value between 1 kA and 5 kA at which system stability ceases remains to be found. At $\gamma > 7$ a ten percent ion current will cause less than a one percent variation in beam energy. This appears acceptable for collective wave accelerators.

REFERENCES

1. J. Chen and R.V. Lovelace, Phys. Fluids **21**, 1623 (1978).
2. M.E. Jones and L.E. Thode, Los Alamos Scientific Lab Report LA-UR-79-3107 (1979).
3. S.E. Graybill and J.R. Uglum, J. Appl. Phys. **41**, 236 (1970).
4. G.W. Kuswa, L.P. Bradley, and G. Yonas, IEEE Trans. N. S. **20**, 305 (1973).
5. F. Mako, Ph.D. Thesis, Univ. of California, Irvine.
6. D.D. Ryutov and G.V. Stupakov, Fizika Plazmy **2** No. 4 and 5 (1976).
7. C. Roberson and F. Mako, Bull. Am. Phys. Soc. **24**, 1001 (1979).
8. F. Mako, JAYCOR Final Report No. 320-80-002-FR (1980).
9. That serious shortcoming has been corrected in NRL's new PREMAs code which allows for open axial boundaries with "floating" potentials. See: R.J. Barker and S.A. Goldstein, Bull. Am. Phys. Soc. **26**, 921 (1981).
10. E. Ott, T.M. Antonsen, and R.V. Lovelace, Phys. Fluids **20**, 1180 (1977).
11. A.V. Agafonov, V.S. Voronin, A.N. Lebedev, and K.N. Pazin, Zh. Tekh. Fiz. **44**, 1909 (1974), [Sov. Phys. Tech. Phys. **19**, 1188 (1975)].

12. V.S. Voronin, E.G. Krastelev, A.N. Lebedev, and B.N. Yablokov, *Fiz. Plazmy* **4**, 606 (1978), [*Sov. J. Plasma Phys.* **4**, 336 (1978)].
13. R.J. Barker, A.T. Drobot, S.A. Goldstein, and R.E. Lee: *Proc. 9th Conf. on the Numerical Simulation of Plasmas*, Evanston, Illinois (1980).
14. R.H. Jackson and R.K. Parker, *Bull. Am. Phys. Soc.* **23**, 906 (1978).
15. R.H. Jackson, et al., *Bull. Am. Phys. Soc.* **25**, 947 (1980).
16. R.J. Barker, S.A. Goldstein, and R.E. Lee, *NRL Memorandum Report 4279* (1980).
17. J.D. Lawson, *The Physics of Charged Particle Beams*, Clarendon Press, Oxford (1977).
18. I.S. Gradshteyn and I.W. Ryzhik, *Table of Integrals, Series and Products*, Academic Press, New York (1965).
19. R.B. Miller, *An Introduction to the Physics of Intense Charged Particle Beams*, Plenum Press, New York (1982).

Table 1 — Diode Currents and Charges

	Case 1	Case 2	Case 3
I_{ion} (kA)	0	1	5
$I_{electron}$ (kA)	9.6	11.6	19.7
I_{tip} (kA)	2.8	4.3	8.3
$I_{outside}$ (kA)	6.8	6.9	6.7
I_{inside} (kA)	—	0.4	0.7
Q_e (x1000 statcoul)	-18.6	-21.1	-33.2
Q_i (x1000 statcoul)	0	+4.06	-20.4

Table 2 — Comparison
of Code and Analytic Calculated Times
to Reach Final Radius

I_{ion} (kA)	1	5
r_0 (cm) initial	.725	.725
r (cm) final	.83	1.07
code time, t (ns)	.8	.8
time from Eq. (3), t (ns)	.859	.713
% Relative deviation in times	7.4	11

Table 3 — Comparison of
Code and Analytic Limit Currents.
Potential evaluated at $r = r_2$.

I_{ion} (kA)	0	1	5
$I_{electron}$ (kA) from Eq. (9)	11.03	13.49	24.13
$I_{electron}$ (kA) from Code	9.6	11.6	19.7
% Relative Deviation from Eq. (9)	12.7	14	18

Table 4 — Comparison of
Code and Analytic Limit Currents.
Potential evaluated at $r = r_1$.

I_{ion} (kA)	0	1	5
$I_{electron}$ (kA) from Eq. (10)	7.3	11.01	27.85
$I_{electron}$ (kA) from Code	9.6	11.6	19.7
% Relative Deviation from Eq. (10)	31.5	5.45	29

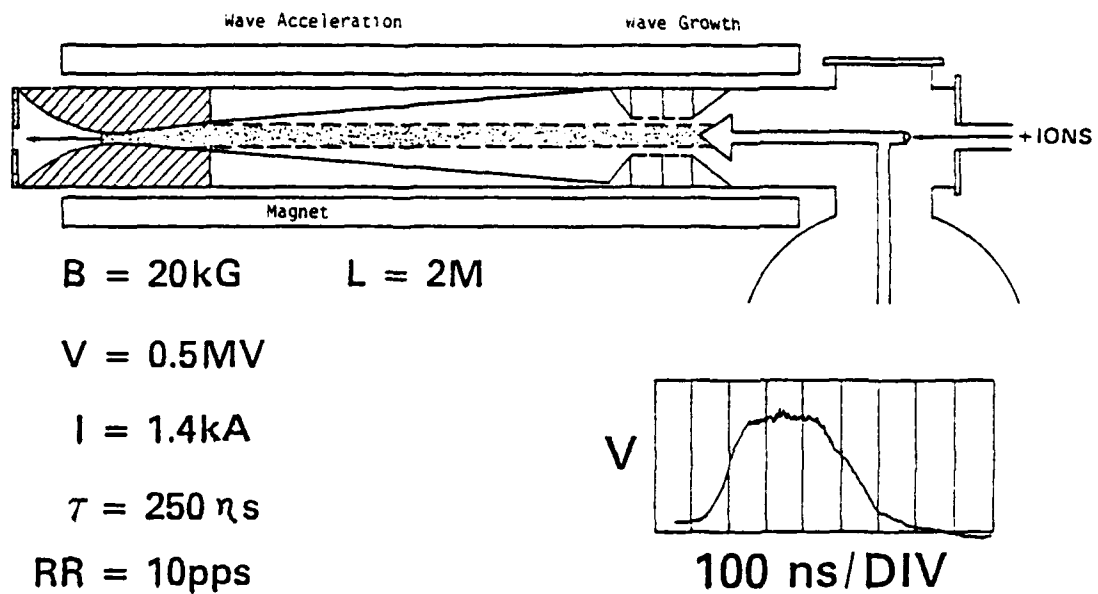


Fig. 1 — The converging guide accelerator

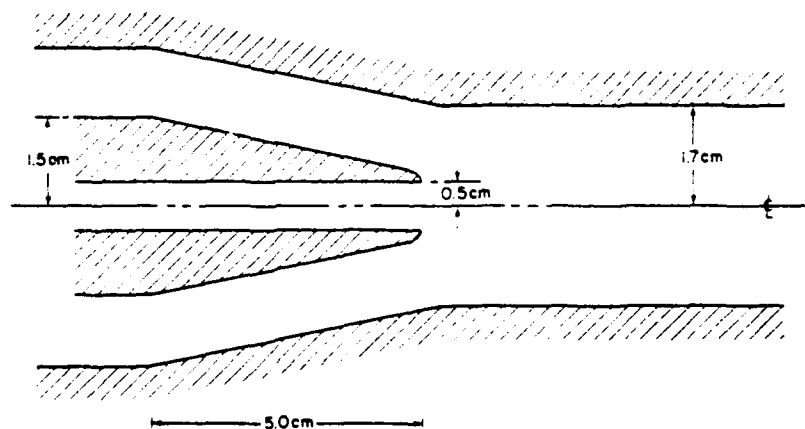


Fig. 2 — The experimental diode geometry

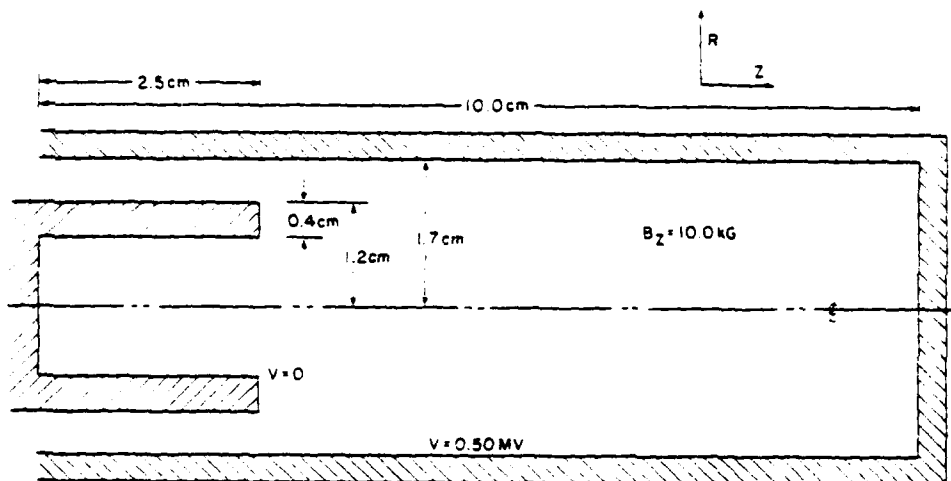


Fig. 3 - The numerical diode geometry

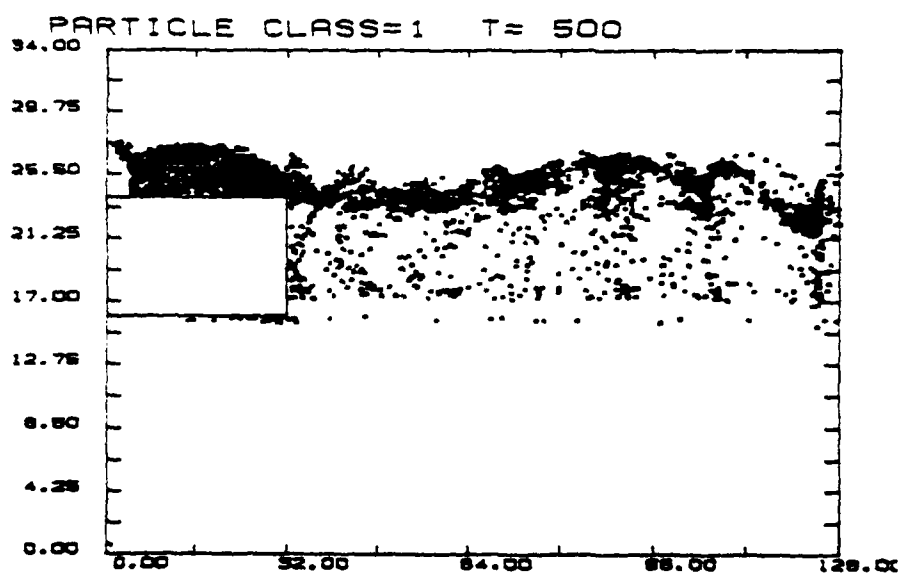


Fig. 4 - Sample electron positions in equilibrium diode with no ions present

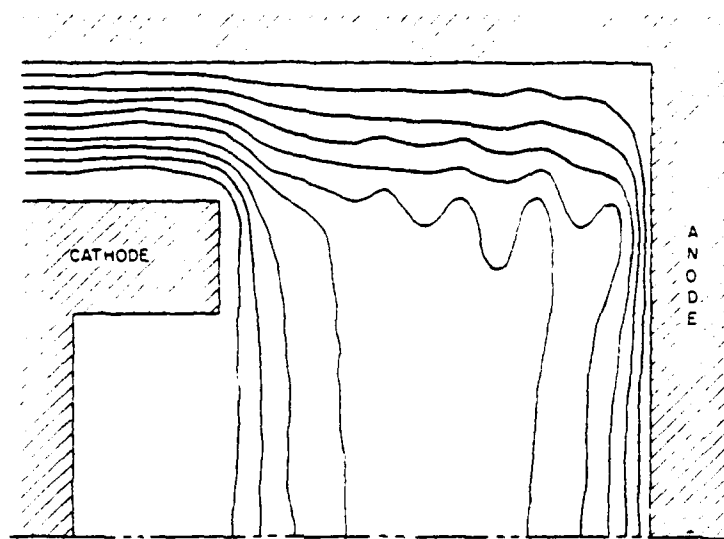


Fig. 5 — $\phi(r, z)$ for electrons—only diode

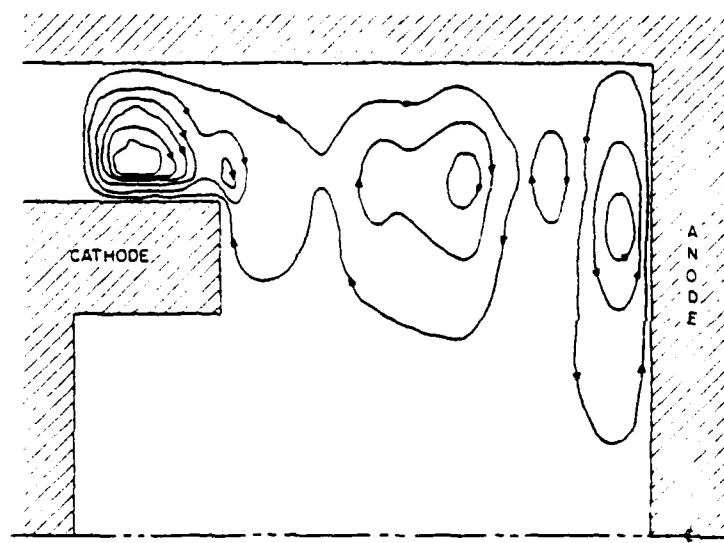


Fig. 6 — Self-magnetic field for electron—only diode

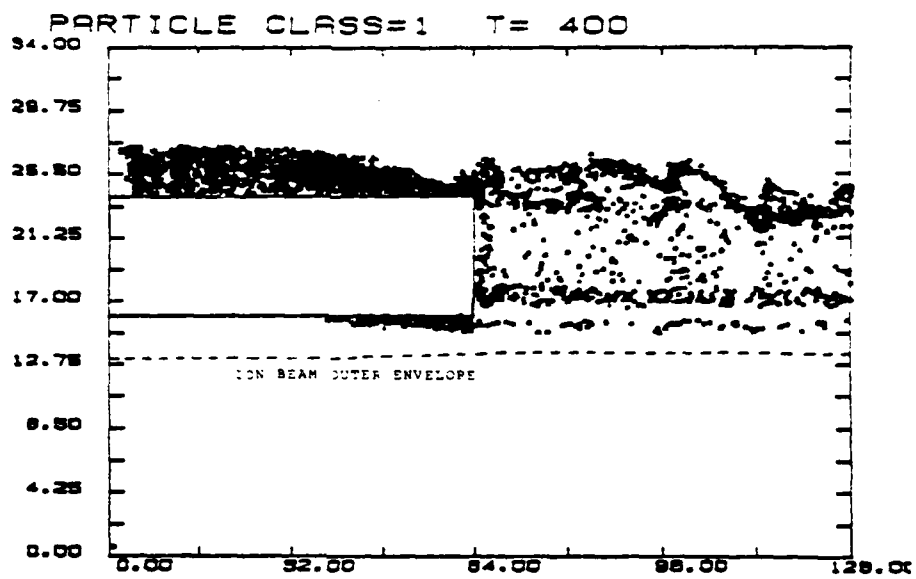


Fig. 7 — Steady-state sample electrons and ion beam envelope
for 1 kA, 30 MeV proton beam

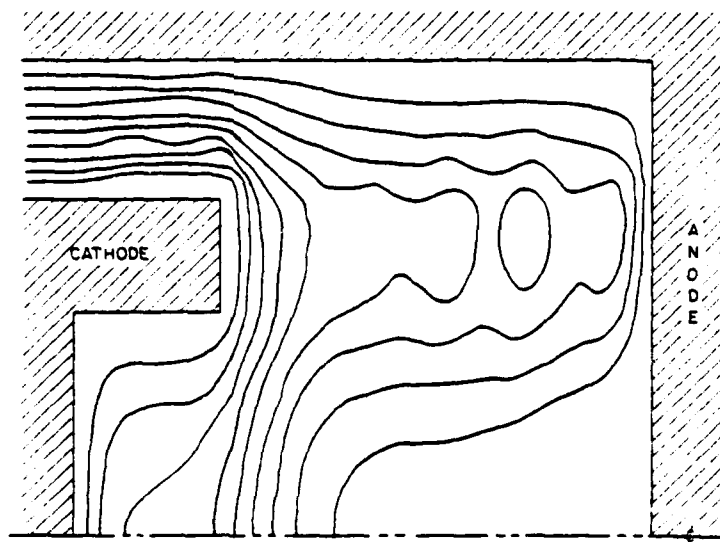


Fig. 8 — $\phi(r, z)$ for diode with 1 kA,
30 MeV proton beam

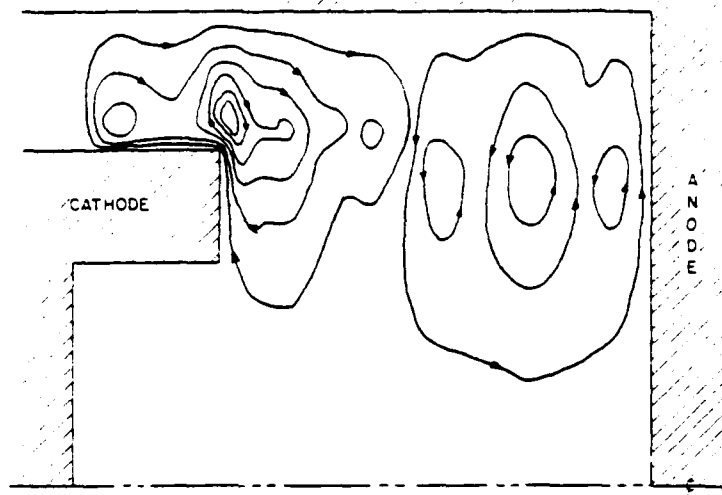


Fig. 9 — Self-magnetic field for diode with 1 kA.
30 MeV proton beam

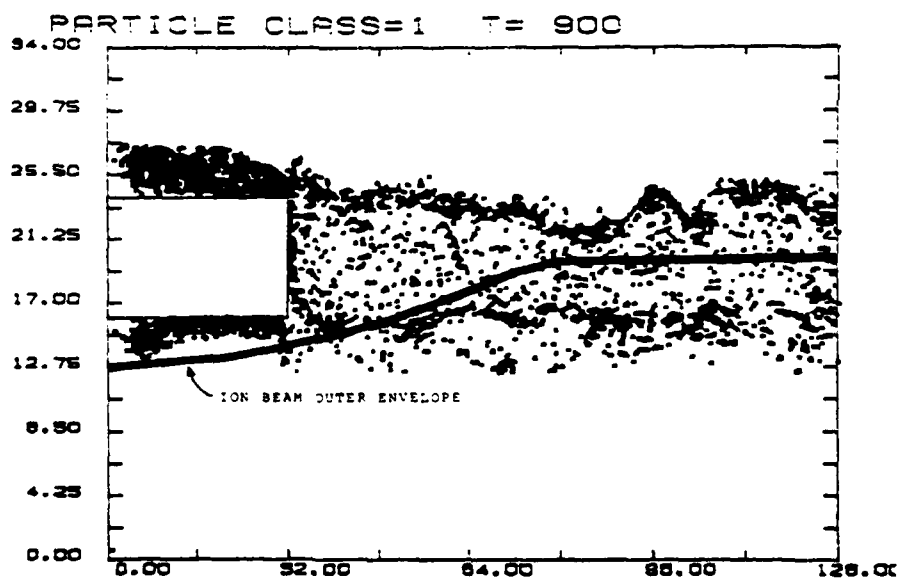


Fig. 10 — Sample electrons and ion beam envelope for 5 kA.
30 MeV proton beam

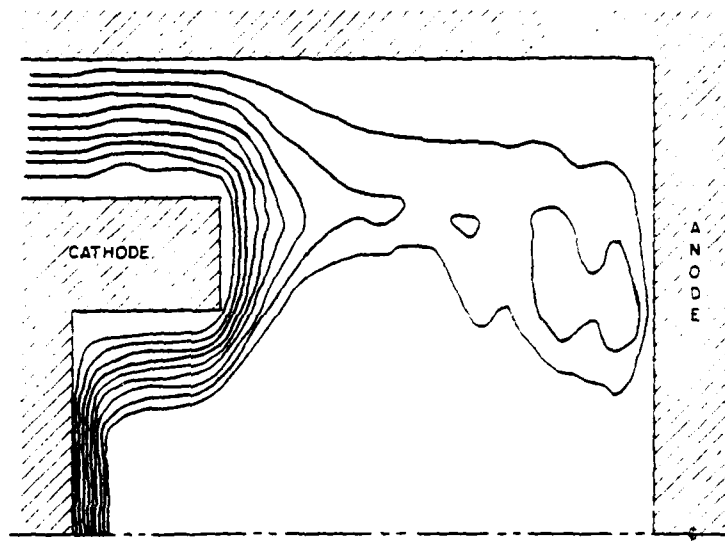


Fig. 11 — $A(r, z)$ for diode with 5 kA,
30 MeV proton beam

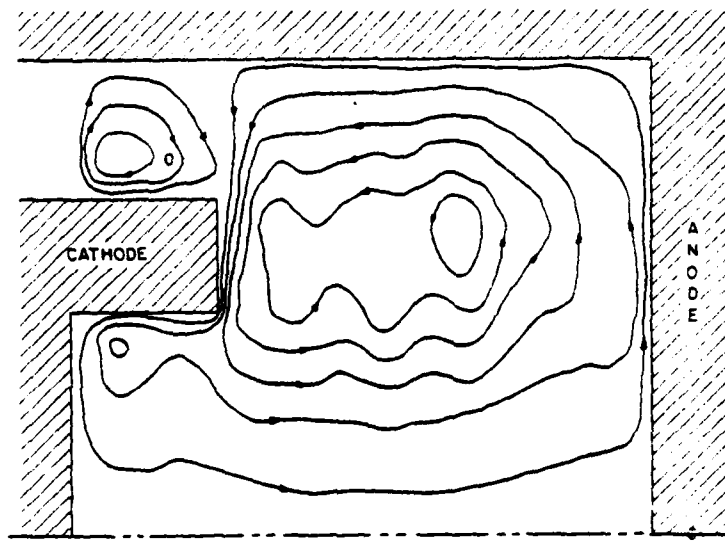


Fig. 12 — Self-magnetic field for diode with 5 kA,
30 MeV proton beam

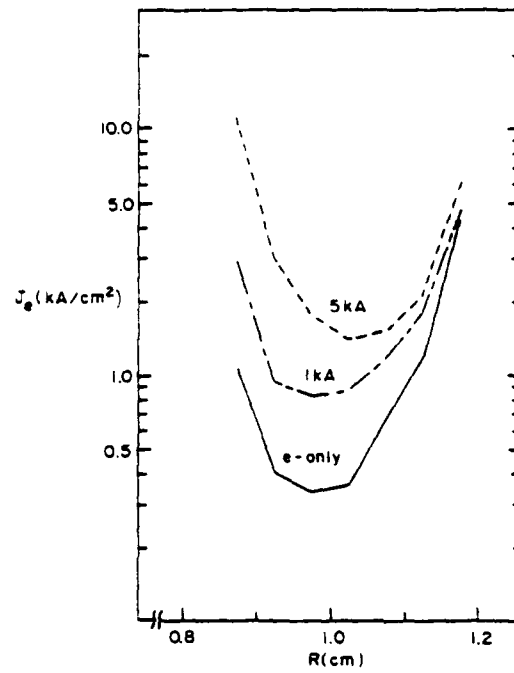


Fig. 13 - $J_e(r)$ emitted from cathode tip

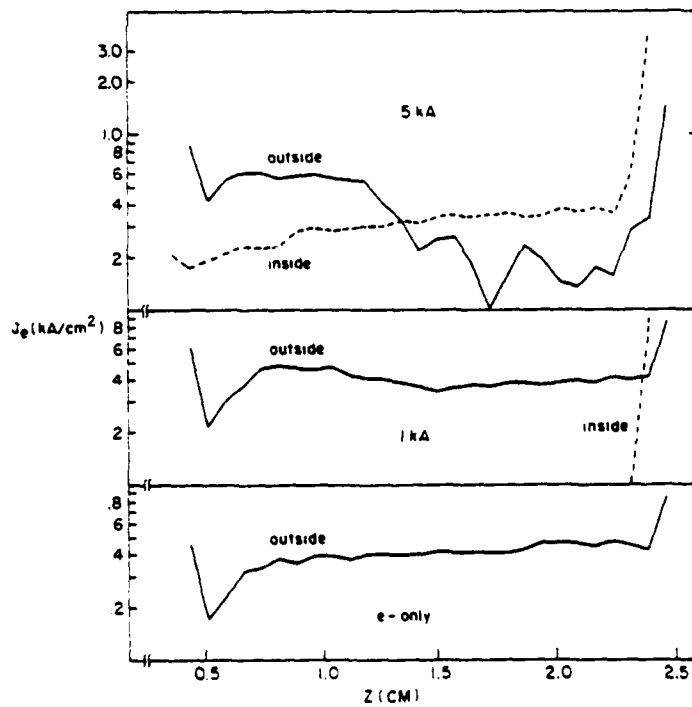


Fig. 14 - Profiles of electron shank emission

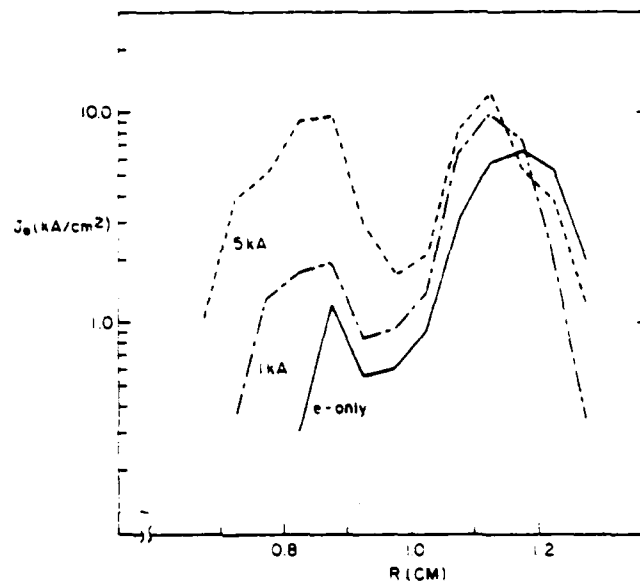


Fig. 15 — $J_e(r)$ collected at anode endplate

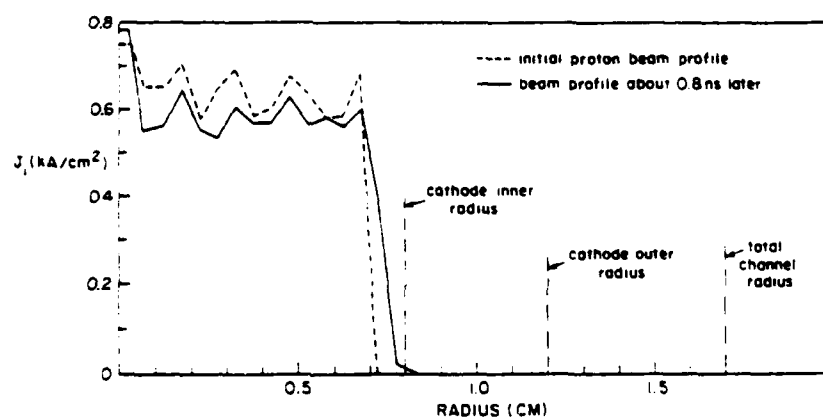


Fig. 16 — Profiles of $J_i(r)$ for 1 kA, 30 MeV proton beam case

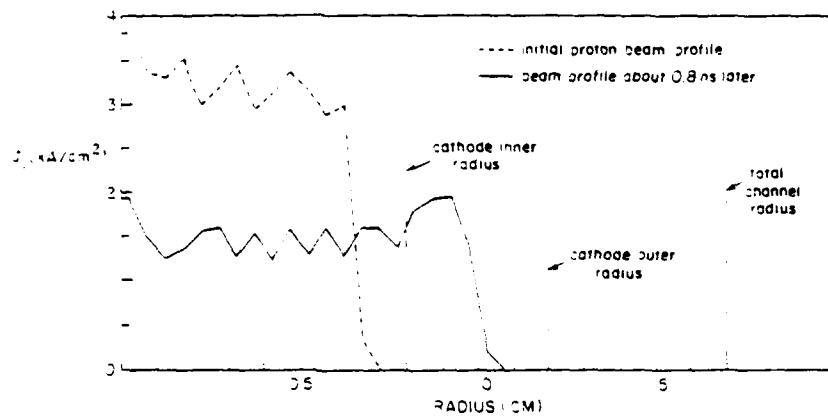


Fig. 17 — Profiles of $J_p(r)$ for 1 kA, 30 MeV proton beam case

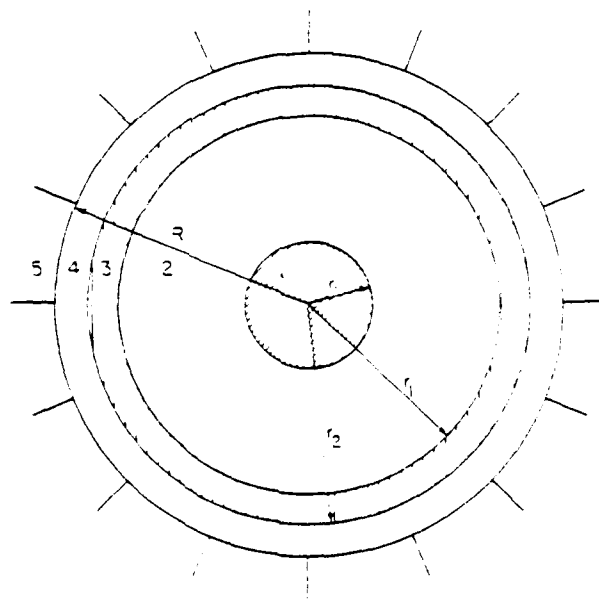


Fig. 18 — Schematic R-r cross-section of foilless diode

High Current, High Voltage Accelerators as
Free-Electron Lasers Drivers

C. W. Roberson, J. A. Pasour, C. A. Kapetanacos, P. Sprangle,
J. Golden, F. Mako and R. Lucey
Naval Research Laboratory, Washington, DC 20375

Free-Electron Generators of Coherent Radiation
June 22-25, 1981

Free-Electron Generators of Coherent Radiation

Based on Lectures of the Office of Naval Research Sponsored Workshop,
June 22-25, 1981, Sun Valley, Idaho

Edited by

Stephen F. Jacobs, *Optical Sciences Center, University of Arizona, Tucson*

Gerald T. Moore, *Institute for Modern Optics, Department of Physics and
Astronomy, University of New Mexico*

Herschel S. Pilloff, *Office of Naval Research, Arlington, Virginia*

Murray Sargent III, *Optical Sciences Center, University of Arizona, Tucson*

Marlan O. Scully, *Institute for Modern Optics, Department of Physics and
Astronomy, University of New Mexico*

Richard Spitzer, *Stanford Linear Accelerator Center, Stanford University,
Stanford, California*



1982

Addison-Wesley Publishing Company
Advanced Book Program, World Science Division
Reading, Massachusetts

London • Amsterdam • Don Mills, Ontario • Sydney • Tokyo

HIGH CURRENT, HIGH VOLTAGE ACCELERATORS AS
FREE-ELECTRON LASERS DRIVERS

C.W. Roberson, J.A. Pasour, C.A. Kapetanakis,
P. Sprangle, J. Golden, F. Mako[§] and R. Lucey[†]

Naval Research Laboratory
Washington, DC

ABSTRACT

There are several approaches to generate high voltage multi-kiloampere electron beams under investigation at the Naval Research Laboratory. Such accelerators could provide compact drivers for high power Free Electron Lasers. Three of these potential FEL drivers are discussed in this paper. They are (1) the Long Pulse Induction Linac, (2) the Race-track Induction Accelerator and (3) the Modified Betatron.

INTRODUCTION

During the past fifty years accelerators have developed primarily along two diametrically opposite directions: (1) low current, high voltage and (2) high current, low voltage devices.

[§] JAYCOR

[†] Pulse Sciences, Inc.

100-A137 447

THE MODIFIED BETATRON ACCELERATOR EXPERIMENT(U) JAYCOR
ALEXANDRIA VA F M MAKD 06 JAN 84
JAYCOR-J206-84-001/6207 N00014-81-C-2095

3/3

UNCLASSIFIED

F/G 20/7

NL



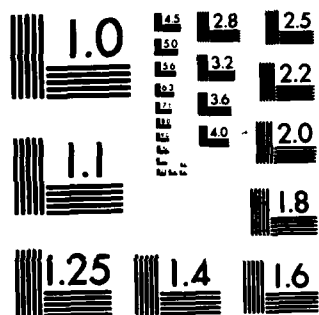
END

DATE

FILED

• 3-24

DTIC



MICROCOPY RESOLUTION TEST CHART
NATIONAL BUREAU OF STANDARDS-1963-A

Figure 1 is a plot of beam energy vs average beam current of typical accelerators developed during this period. The history of the traditional accelerator development is quite well known.^{1,2} Marx generators with a pulse forming line have been developed primarily as flash x-ray sources or inertial fusion drivers.

The free electron laser requires high voltage for short wavelength operation and high current for efficiency and high gain operation.³ Only the Induction Linac has been a serious candidate as an FEL driver in this parameter range to date.

50 YEARS OF ACCELERATOR DEVELOPMENT

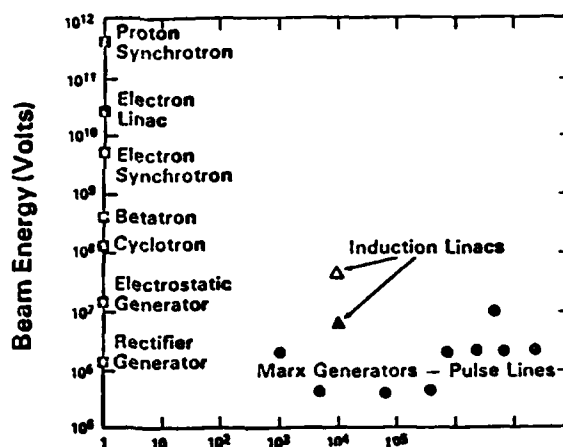


Figure 1.

This paper describes three accelerator approaches being pursued at NRL that could be used as drivers for free electron lasers; (1) the Long Pulse Induction Linac (2) the Racetrack Induction Accelerator and (3) the Modified Betatron.

THE LONG PULSE INDUCTION LINAC

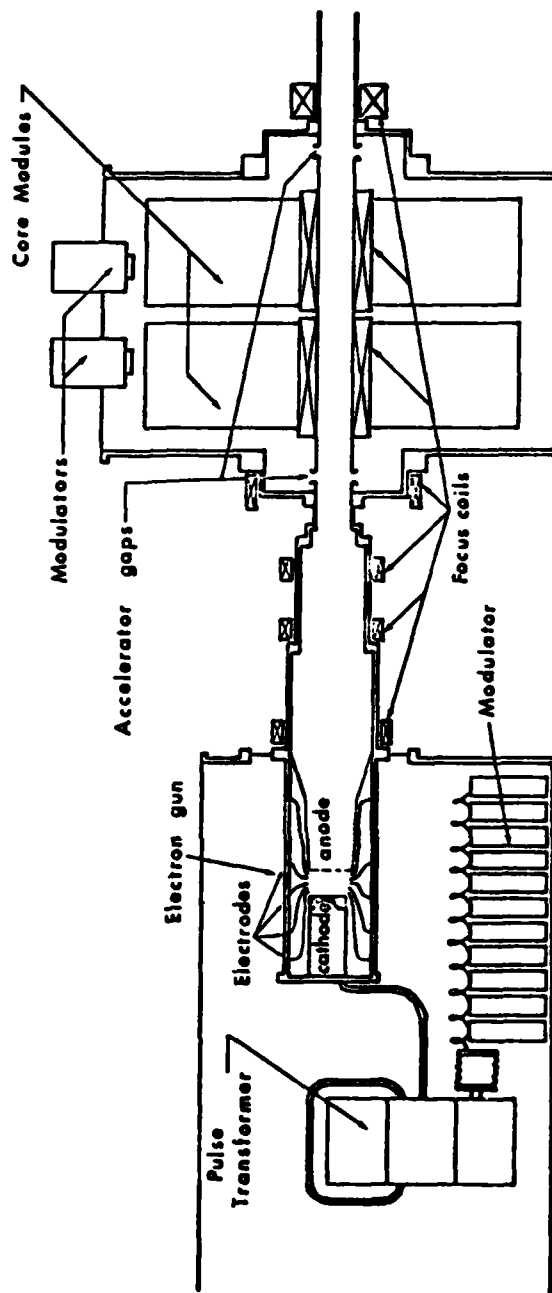
Figure 2 is a schematic of the Long Pulse Induction Linac. This device was built at the National Bureau of Standards⁴ and is currently in operation at the Naval Research Laboratory. The accelerator consists of two major components; (1) an injector and (2) an induction accelerator module.

The electron gun in the injector has a 16.5 cm diameter tungsten dispenser thermionic cathode. Electrons are accelerated in the gun through a series of 22 annular electrodes, spaced by ceramic insulator rings. The last electrode has a 95% transmission screen of tungsten and is at ground potential.

The electron gun is immersed in an oil filled tank. The gun voltage is fed from a pulse line driving a 12:1 step up transformer. The injector typically produces a 0.8 kA current beam pulse of 400 keV energy. The electron beam is transported to the induction accelerator module by a series of focusing coils.

The induction accelerator module consists of two core sets. One of the core sets gives a 4 to 1 step up voltage

INDUCTION LINAC



$V = 0.8 \text{ MV}$
 $I = 0.8 \text{ kA}$
 $\tau \sim 2.0 \mu\text{s}$
 $\frac{\Delta V}{V} \sim 3\%$
 $N \sim 10^{16} \text{ particles}$

Figure 2.

and the other a 5 to 1. The cores are wound with 0.001 inch mild steel foil, separated by 0.00025 inch mylar sheets. Each accelerating gap produces about 200 kV of acceleration.

Typically, the output energy of the electron beam generated by the linac is 0.8 MeV, the current approximately 0.8 kA and the pulse length 2 microseconds. The temporal variation in the voltage is less than 3 percent over 1.6 microseconds. This is the longest pulse induction linac in existence. Shorter pulse induction linacs of 40 nsec^{5,6} and 300 nsec⁷ have been built. The pulse length becomes an important consideration for free electron laser experiments where one wishes to study the nonlinear dynamics of the beam, or efficiency enhancement schemes. Applications that require a significant amount of energy in the radiation field also require long pulses to avoid the problems encountered with excessive electric field strengths at short pulses.

We have designed and constructed a free electron laser experiment that will use as a driver the beam from the induction linac, which will be focused to 0.5 - 0.75 cm. A pulsed, 120 cm long, 3 cm wavelength linear wiggler will provide the field modulation. The wiggler amplitude rises adiabatically in 30 cm, has a uniform straight section of 60 cm and decays adiabatically in the last 30 cm. There is a uniform axial field over the length of the wiggler that can vary from 1 to 5 kG. The output radiation is expected to be in the 3-4 mm range and the theoretical efficiency is about 10%.

THE RACETRACK INDUCTION ACCELERATOR

The Racetrack Induction Accelerator is a new high current-high voltage cyclic accelerator concept.⁸ The accelerator is designed to take advantage of long pulse induction accelerator modules to obtain a high voltage, high current electron beam in a geometry that is suitable for free electron laser operation. The geometry is an oval racetrack shaped toroid, similar to a model C stellerator.⁹ The geometry is shown in Figure 3. In one leg of the racetrack a long pulse induction accelerator module is inserted. The voltage gain of a particle as it goes around the racetrack is approximately

$$V_f = \frac{T}{\tau} V$$

where V is the voltage gain per pass through the induction module, T is the time the induction accelerator module is on, τ is the time it takes a particle to go around the racetrack, and V_f is the final voltage. In the first stage of operation we plan to construct a 5 MeV, 1 kA racetrack accelerator. The induction accelerator module from the existing linac is capable of accelerating a beam to 20 MeV in the geometry shown in Figure 3.

The high current operation of the racetrack requires a magnetic field in the direction of particle motion. This prevents the beam from blowing up due to space charge.

The toroidal magnetic field can cause the beam to drift out of the accelerator as a result of the field curvature in

RACETRACK INDUCTION ACCELERATOR — TOROIDAL MAGNETIC FIELD — APPLICATION TO FREE ELECTRON LASERS

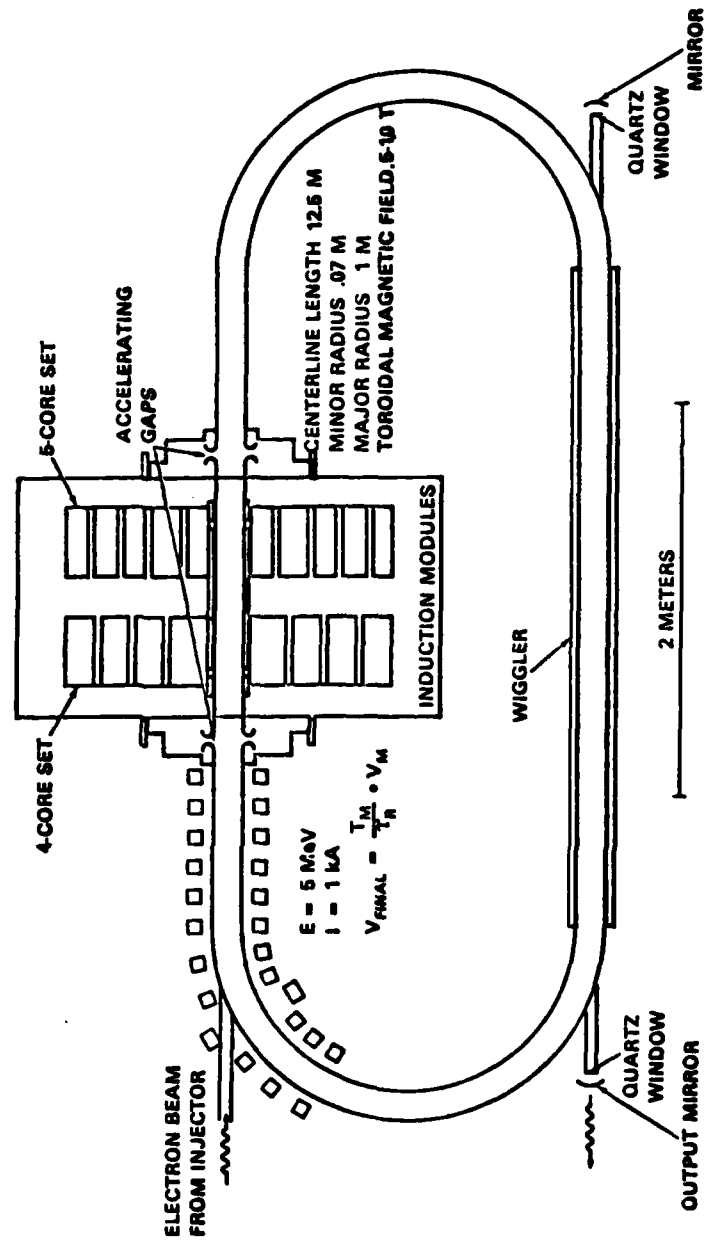


Figure 3.

the bends. This drift can be averaged out by applying an $n = 2$ helical winding in the bends. For moderate energies, the magnetic fields of such an accelerator can be steady state. An advantage of such a fixed field accelerator is that the shape of the accelerating pulse is not critical. The final energy of accelerated particles is simply the volt-secs of the induction module, divided by the transit time and is independent of pulse shape. This is true provided the final energy does not exceed a maximum determined by magnetic field and geometry. With a 1 meter radius of curvature bend, computer orbit calculations¹⁰ indicate that a stellerator magnetic field of 1 kG/MeV is required to contain single particles.

High energy operation requires a time dependent vertical field to reduce the curvature drift in the bends. The stellerator fields then serve to provide a stable energy bandwidth of 1 MeV/kG about the equilibrium orbit.

For FEL applications, a wiggler can be inserted and an optical cavity formed in one leg of the accelerator provided the gain is not too low as a result of energy spread in the beam. One can achieve variable wavelength operation over a wide range during the acceleration phase or long pulse narrow band, operation after acceleration.

As a result of inserting the long pulse induction accelerator module in a racetrack geometry with stellerator fields we have the possibility of a factor of 40 gain in the energy. This could result in a high gain free electron laser in the infrared region.

THE MODIFIED BETATRON

The betatron is a compact cyclic accelerator with a well-known technological background. Betatrons have long been used to accelerate electrons to high energies (~ 300 MeV). However, for a beam of energy $mc^2\gamma$, the current in these devices is quite low because of the space charge limit ($I_{lim} = \gamma^3$) and because of various beam instabilities (which typically scale as $I_{lim} = \gamma$). Consequently, a conventional betatron is not suitable to accelerate large current ($> \text{several kA}$) electron beams that are injected at low energy ($\gamma < 10$).

The modified betatron accelerator overcomes the current limitation inherent in the conventional betatron by the addition of a strong toroidal magnetic field component parallel to the particle orbits (Figure 4). It can be shown from space charge considerations alone that the maximum number of electrons that can be confined in a modified betatron is larger than the corresponding number for a conventional betatron by a factor $1/2 (B_\theta/B_z)^2$, where B_θ and B_z are the toroidal and vertical or betatron magnetic fields, respectively. The maximum current that can be confined in a modified betatron then is

$$I_{max} = 2.1 \left(\frac{r_b}{r_o} \right)^2 \gamma^3 \left(\frac{B_\theta}{B_z} \right)^2 [\text{kA}],$$

where r_b and r_o are the minor and major beam radii. Thus, for $r_b = 1$ cm, $r_o = 1$ m, $\gamma = 5$, $B_z = 100$ G, and $B_\theta = 5$ kG, the maximum current is about 65 kA. Although this value

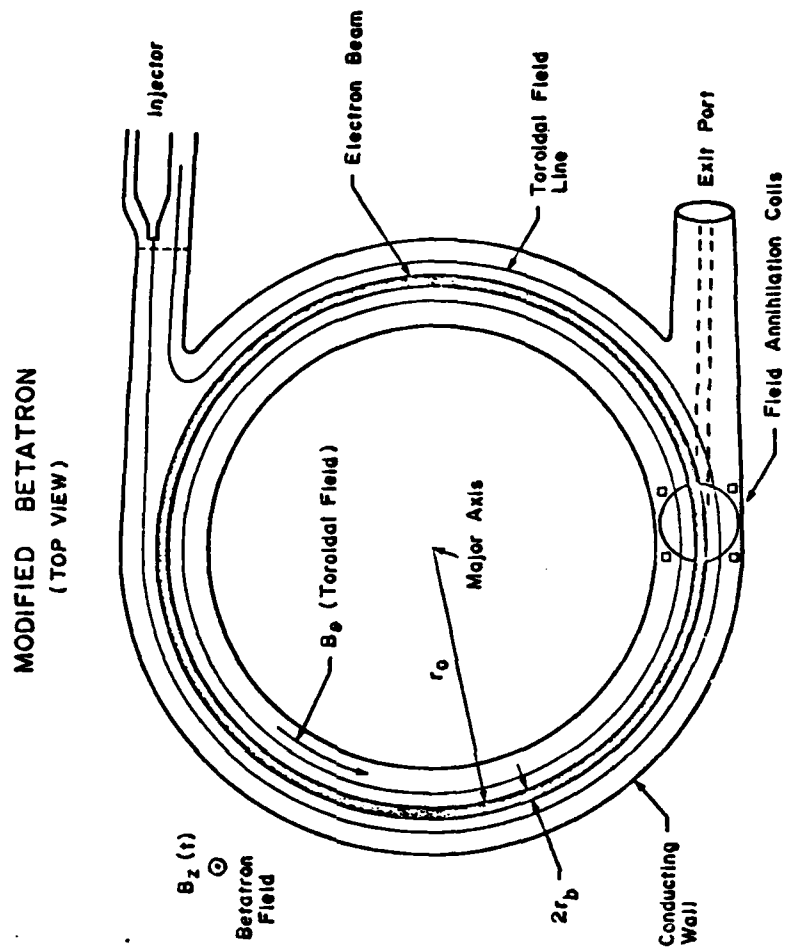


Figure 4.

represents the limit due only to space charge effects, it can be shown that the constraints imposed by stability considerations are also substantially reduced by the imposition of a toroidal field.

In Figure 4, a possible injection and ejection scheme is depicted. Electrons from an external source are injected along open field lines into the torus. Conditions can be chosen so that the forces on the beam arising from both the external and self fields cause the beam to drift inward on an open orbit.¹² When it reaches the center of the torus, an external parameter is changed so that the beam is on a closed orbit and thus is trapped. One relatively simple way to achieve this trapping is to change the external field index n , which determines the variation of B_z with r ; i.e. $B_z(r) = r^{-n}$. After trapping, the beam is accelerated just as in a conventional betatron by increasing the vertical field. After acceleration, the beam can be extracted by suddenly energizing the field annihilation coils, thereby allowing the beam to leave the torus along a tangent to the orbit.

A proof of principle experiment is now being designed at NRL in which a modified betatron will be used to accelerate a 10 kA electron beam from ~ 3 MeV to a final energy of ~ 50 MeV. Theoretical analyses and computer simulations¹² have indicated that such parameters are feasible for a 1 m radius beam. The initial and final betatron fields would then be ~ 170 G and ~ 1.7 kG, respectively, with a toroidal field of ~ 10 kG.

The applicability of the modified betatron to FEL experiments will depend to a large extent on the quality of the extracted beam. Although little work has been done on this aspect of the problem, the current and energy levels that are theoretically achievable could make possible a high-gain, infrared FEL.

SUMMARY

We have briefly discussed three approaches to high current beam accelerators presently being investigated at the Naval Research Laboratory. These accelerators are scalable to energies in excess of those obtainable with a Marx-pulse line beam generator. The induction linac at NRL is unique because of its long pulse length. Although the linac is scalable to high energies, the cost encourages one to examine the possibility of high current cyclic accelerators. Two high current cyclic accelerator concepts that are scalable to high energies have been discussed. These devices are presently in the conceptual design phase at NRL. The suitability of these accelerators as FEL drivers must await their development.

A number of FEL experiments have been planned for the long pulse induction linac. The design parameters of the first such experiment is discussed in this paper. This experiment is expected to be in operation in the near future.

REFERENCES

1. Particle Accelerators, M. Stanley Livingston and John P. Blewett; McGraw-Hill Book Company, Inc. 1962.
2. "The Next Generation of Particle Accelerators", Robert R. Wilson; Scientific American; V. 242, 42 (1980).
3. P. Sprangle, R.A. Smith and V.L. Granatstein, "Infrared and Submillimeter Waves," K.J. Button, ed. Vol. 1, p. 279, Academic Press, NY. (1979)
4. J.E. Leiss, N.J. Norris and M.A. Wilson, Particle Accelerators, V. 10, 223 (1980).
5. R. Avery, et. al., IEEE Trans. Nuc. Sci., Vol. NS-18, #3 3401, (1981).
6. T.J. Fessenden, et.al. IEEE Trans. Nuc. Sci. Vol. 28, #3 3401, (1981).
7. J.W. Beal, N.C. Christofilos and R.E. Hester IEEE Trans. Nucl. Sci. NS-16 #3 (1969).
8. C.W. Roberson, IEEE Trans. Nucl. Sci. Vol. NS-28, 3433, (1981).
9. K.M. Young, Plasma Physics, 16, 119 (1979).
10. A. Mondelli, (private communication).

11. P. Sprangle and C.A. Kapetanakos, Journal of Applied Physics 49, 1, (1978).
12. P. Sprangle, C.A. Kapetanakos, and S.J. Marsh, Proc. of 4th Int'l. Topical Conf. on Electron and Ion Beam Res. and Tech., Palaiseau, France, July 1981.

